School of Civil and Mechanical Engineering

Modelling, Simulation and Experimental Diagnostics of Failures in Rotor Systems Supported by Active Magnetic Bearings

Vahid Ehtemam Haghighi

This thesis is presented for the Degree of

Doctor of Philosophy

of

Curtin University

February 2019

Declaration

To the best of my knowledge and belief this thesis contains no material previously published by any other person except where due acknowledgment has been made.

This thesis contains no material which has been accepted for the award of any other degree or diploma in any university.

Signature: ……..

Date: ……..

Acknowledgement

I would like to express my sincere thanks to my supervisor and co-supervisor, Dr. Rodney Entwistle and Professor Ian Howard for giving me the opportunity to be their research student. I would like to thank them for their continuous support and providing me the means for the experimental work in the Active Magnetic Bearing field.

I would like to sincerely thank Mr. Andrew Lee Steer of Woodside for providing me with the SKF magnetic bearing test rig with which I could extend my knowledge and experience to the next level. I would like to thank Ms. Hannah Downie of Woodside for sharing the outcome of her undergraduate research.

I would like to acknowledge support of Mr. Alexandre Kral, Mr. Jeff Smithanik, Mr. Blair Martin of SKF for introducing their test rig and the information about the components of the test rig.

Finally, I would like to express my sincere gratefulness to my family for all their love, attention, and invaluable advice which smoothed the ups and downs of my life. I dedicate my PhD thesis to them.

Abstract

With the increasing application of Active Magnetic Bearings (AMB) in industry, the diagnostics and troubleshooting of rotor systems supported with this type of bearing is getting more attention. This thesis takes a practical 'diagnostics' approach to AMB supported rotors where little research has been done in this field. The behaviour of rotors supported by AMB is highly dependent on the controller module, which varies for different AMB designs, and is different compared to other types of bearings. Therefore, the understanding of controller components and their design, in addition to the rotordynamic behaviour of the rotor, is necessary for diagnosis and troubleshooting of failures in AMB supported rotors.

For the purposes of this research, a SKF MBRotor-II Test Stand, which is controlled by an industrial controller and its software package, is modelled and simulated to provide understanding of the test rig and its controller. First, the Finite Element Model (FEM) of the rotor was created in MATLAB. The free-free FEM of the rotor provides the mechanical rotordynamic characteristics of the rotor, which are validated against the data provided by the vendor. The eigenvectors of the rotor provide insight about the location of rotor nodes relative to the non-collocated magnetic bearing actuator and position sensors. In addition, mass, stiffness and damping matrices from the FEM are extracted to create a state-space model of the rotor. The rotor state-space model has a high number of states which makes the simulation computationally challenging. The rotor state-space model was reduced for improving the simulation speed in MATLAB.

The controller section of the test stand has multiple components (several filters, sensors, power amplifiers, and actuators). The transfer function of each component was derived based on the parameters provided by the vendor. In addition, the electrical current and displacement stiffness of the AMB was calculated based on the setting of the SKF software (MBScope). These parameters in addition to the reduced rotor state-space model were incorporated to create a Simulink model.

Based on ISO14839-3 (2006) standard, the open loop transfer function of the Simulink model for each axis of the bearings were compared against the transfer function

extracted by injecting signal in the test stand. The validity of the model and the resulting Bode plots are discussed.

Finally, different failures, including controller issues or mechanical issues such as rub, misalignment, unbalance and non-optimal controller settings were investigated using the rotorkit. The diagnostics methods applied in this research not only consider the design and controller parameters but also consider the rotordynamic measurement data of the shaft including important parameters such as measured phase, average and instantaneous gap voltage and AMB current. This type of data helps to identify faults and problems in AMB supported rotating equipment which has not been a focus in previous research. For implementing the diagnostics, high resolution data were taken from all position and current sensors in transient and steady state speed which helps in comprehensively diagnosing both controller and mechanical problems. The results of the experiments are discussed in several plots. The balancing of the rotorkit was achieved by applying conventional balancing procedures. It is important to note that in some cases that rotor vibration was close to the machine's trip limits when passing the resonance. In these cases, random location of trial weight would not allow the machine to pass the resonance as it worsens the unbalance of the rotor. In such cases, the location of the trial weight could be defined by considering the location of the heavy spot in the polar plot of the measured data.

It is also shown that the stability criteria defined in ISO14839-3 (2006) and API617 (2014) is not enough to ensure the continuous normal operation of the rotor system. More analysis such as closed loop system root locus or open loop frequency response should be considered to ensure the normal operation of the rotor system across the sampling frequency of the controller.

Table of Contents

Table of Figures

Chapter 1

Introduction

1.1 Background of Active Magnetic Bearings

Active Magnetic Bearings (AMB) is a type of bearing that supports the rotor in rotating equipment similar to fluid film bearings or roller element bearings with the difference that there is no contact between the rotor and bearing.

The magnetic bearing concept was invented over a century ago. Beams and Holms applied AMBs for suspending a centrifugal rotor in 1938 after which he filed the patent “Suspension of Rotatable Bodies” (Beams & Holmes, 1941).

Figure 1-1 shows the sketch from the patent filed by Beams and Holms. They have rotated a rotor with the speed of 1150 rps for several hours with a variation of speed of no more than 2 rps per hour. Magnetic bearings have not become popular in industry until the late twentieth century because of their dependence on highly complicated control algorithms. Being contact free and providing some other advantages, they are now becoming popular in industry to the extent that they have become the bearing of the choice for turbo-expanders and subsea compression units.

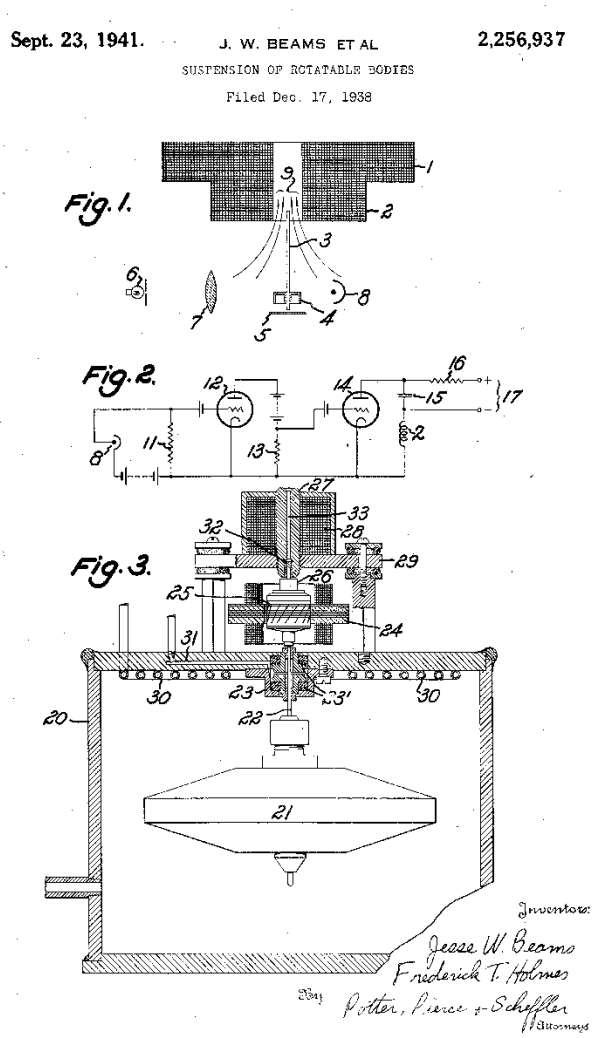

Figure 1-1: Suspension of rotatable bodies. Patent: US 2256937 A.

1.2 AMB Advantages and Disadvantages

One of the *advantages* of AMBs over fluid film bearings or rolling element bearings is their control system capability. Not only are they highly reliable and more cost efficient for operation, they also provide the capability of manipulating the rotor system behaviour. By changing the stiffness and damping of the rotor system, the response of the system to transient forces can be modified. For example, the AMB could be controlled by the control system so that it has a higher damping when the rotor passes the critical speed (ISO14839-4, 2012).

Being contact free, there wouldn't be wear between rotor and stator, providing a lower maintenance or no-maintenance advantage for the rotating equipment.

Being lubrication free, AMBs provide advantages over fluid film bearings in applications where there are issues with contamination of oil, e.g. compressors in petrochemical complexes. This removes the environmental impacts of changing lubricating oil contaminated with hazardous process gases by providing completely sealed equipment that completely isolates the inside of the equipment from the outside. Therefore, AMBs reduce environmental problems and biodegradation of used oil. They can also remove the requirement for some rotor components, such as dry gas seals, by offering completely sealed casings since the AMBs can operate in process fluids. This advantage would be very applicable to subsea compression units that require the rotor system to be completely sealed under water.

The AMBs capabilities have been improved to operate in high temperature rotating equipment such as gas turbines (Clark, Jansen, & Montague, 2004), (Schweitzer, 2009). AMBs have very low losses and provide support to very high speed shaft. As an example, turbo-molecular pumps are running above 100,000 rpm and ultra-centrifuge prototypes have reached 800,000 rpm (Alves, 1998). The AMBs can also operate in cryogenic environments.

AMBs provide the capability of changing the position of a shaft inside its bearing or casing. Its control capability can be applied to reduce, or to a high extent remove, the vibration forces transmitted to the supports. A very simple example is to control the shaft such that it rotates about its mass principal inertia axis rather than its geometrical axis by applying a notch filter to the control system (ISO14839-1, 2002). This would reduce the amount of unbalanced force exerted on the rotor and the machinery structure which leads to higher reliability and operability of machinery.

AMBs has some *disadvantages* compared to other type of bearings. AMBs require complicated control algorithms to provide the required stability for all operating conditions of the rotating equipment. Normally, AMBs require specialised engineers in the field of control, electrical and mechanical, not only in the design phase but also in commissioning, troubleshooting and diagnostics. There would be a need for highly specialised engineers that are not only highly skilled in their field but also can understand the other fields so that they can solve the problem of rotating equipment in case it occurred.

In order for AMBs to be cost competitive, they should be applied on all bearings of the machine train (string). For example, using AMB on compressor while using fluid bearing on the driver such as turbine will not be economically cost efficient. In this case both auxiliaries for lubrication and control of the AMB are required.

Machinery supported by AMBs requires an auxiliary bearing to provide safety backup in case the AMB fails or power failure happens. Therefore, additional space is required on the machine casing for having AMB with backup bearings.

1.3 Operation of AMBs

AMBs generate magnetic field forces which pull the rotor toward the poles in the AMB. The magnetic forces in the bearing are actively controlled by the controller; hence, the name of this type of bearing is Active Magnetic Bearing. AMB consists of poles opposite to each other which pull the rotor with controlling forces to keep the rotor in the centre of the bearing. The AMB suspends or levitates the rotor in the centre of the bearing and provides a contact free support. Generally, in an AMB supported rotor, the position of the rotor is measured by displacement sensors and the measured signal is sent to the controller. The controller measures the deviation of the measured signal from the desired set point, which is normally the centre of the bearing, and sends the control signals to power amplifiers to compensate for this error. Power amplifiers provide current to the actuators (AMBs) which pull the shaft by electromagnetic forces. Figure 1-2 is a simple schematic of how an AMB operates.

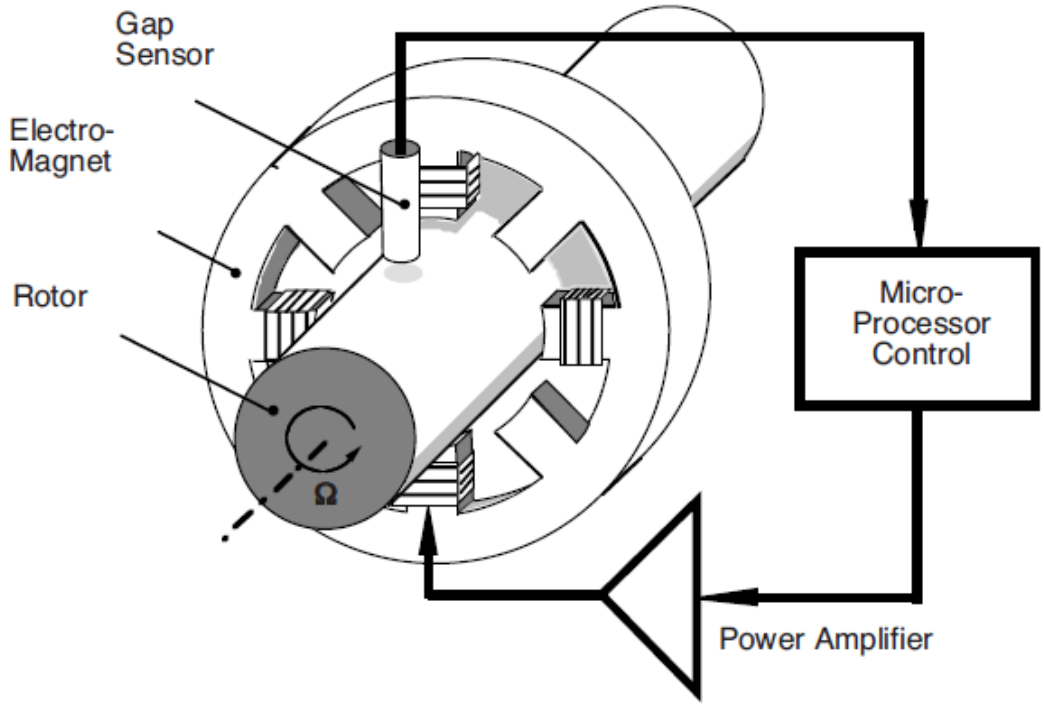

Figure 1-2: Principle of and AMB-supported rotor (Schweitzer, 2009)

1.4 Modern AMB Systems and Their Components

In modern AMB systems the components of an AMB is divided into two major sections: plant system and the controller. Each of them consists of several components. These components are explained in more detail as below.

1.4.1 Plant System

The plant system mainly includes the mechanical components that serve the principal purpose of the rotating equipment. The main components are as follows:

Rotor, impellers, Generator, etc.

These are the main components (mostly rotating parts) of the plant system where mechanical and process forces act on the rotor. For example in the case of a turbo-expander, one side of the shaft is mounted with the expander impeller which acts like a turbine. The other side of the shaft could be mounted with a compressor impeller which uses the energy of the expander side to compress a process gas. In other applications, the shaft could be a single shaft with a generator, which converts the expander power to electricity.

Figure 1-3 shows a General Electric turbo-expander equipped with AMBs. The process gas energy is converted to mechanical rotating energy on the right (expander side) and the mechanical energy of the shaft is used to compress the process gas on the left side (compressor). This equipment is one of the main current applications of AMB systems.

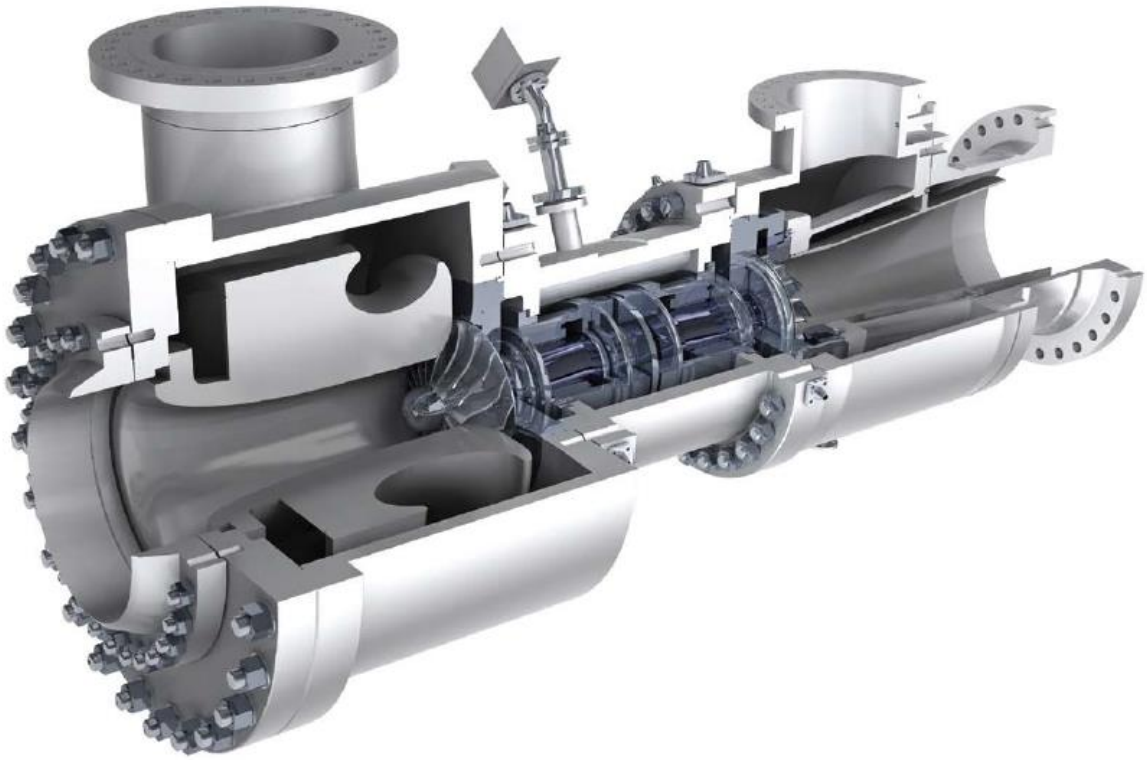

Figure 1-3: General-Electric (2017) TurboExpander with the expander on the right side and the compressor on the left side.

Active Magnetic Bearings (Actuators)

The AMBs levitate the rotor by attractive electromagnetic forces and keep the shaft in the centre of the AMBs. The rotor is consists of laminated plates at the bearing locations. The laminations reduce eddy currents induced by the electromagnetic fields. The AMB stator consists of laminated plates and coils. There are different arrangement of coils and poles in AMBs such as Heteropolar and Homopolar (ISO14839-1, 2002). The Homopolar AMBs have the same magnetic polarity for all poles while the Heteropolar AMBs have different magnetic polarity as shown in Figure 1-4.

Each AMB could be considered to consist of four quadrants, each 90 degrees apart. The axis of the quadrants are 45 degrees (left and right) from the vertical (gravity) direction. Figure 1-5 shows the axis for each quadrant showing the SKF naming convention (V1, V3,

W1, W3) while Figure 1-4 defines the axes based on ISO standards (ISO14839-1, 2002). Each quadrant might consist of several electromagnets that are interconnected with each other.

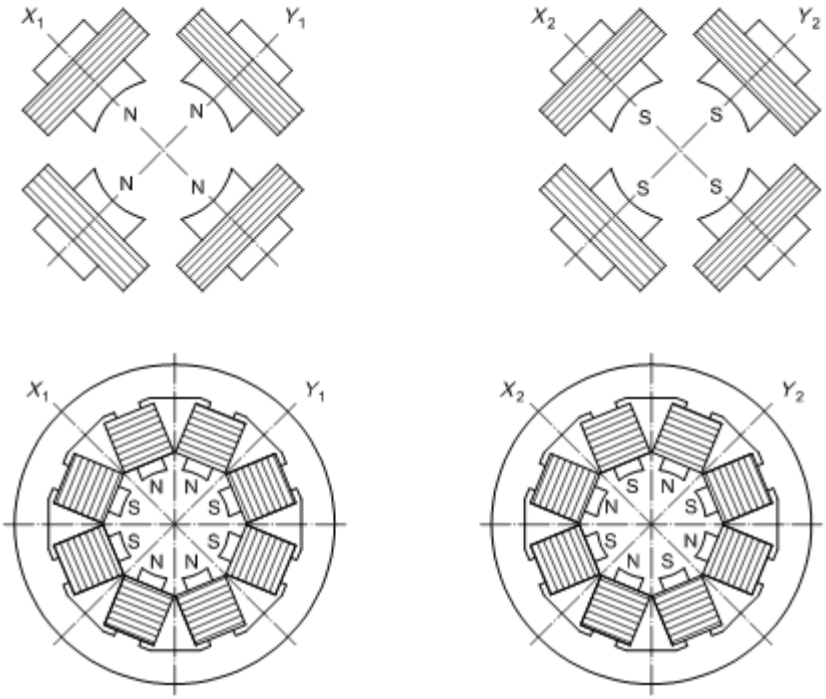

Figure 1-4: Homopolar (Upper) and Heteropolar (Lower) AMB Configurations.(ISO14839-1, 2002)

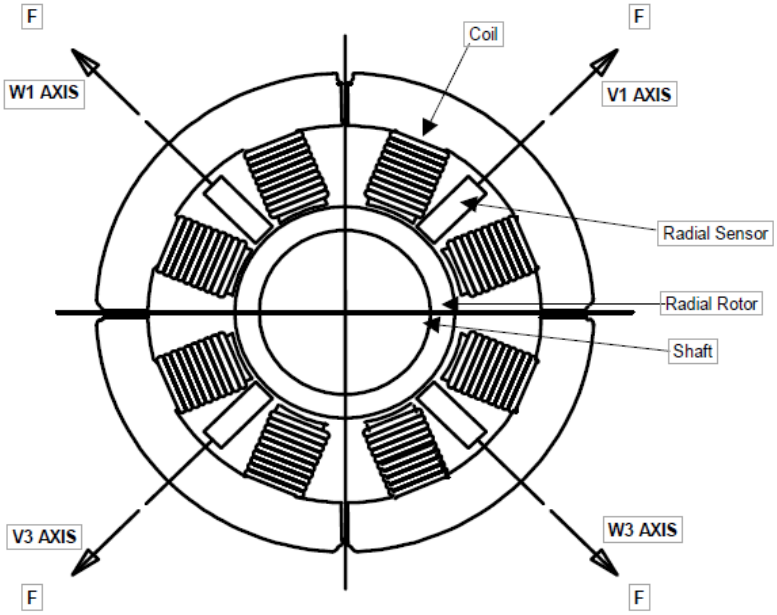

Figure 1-5: AMB sensor and electromagnet arrangement in SKF test stand (viewed from driver to driven) (SKF, 2014b)

The pulling forces that keep the rotor in the centre of the bearing are generated by electromagnets. In operation of magnetic bearings are contactless which reduce the maintenance intervals and increase the reliability of the rotating equipment. Normally in industrial machines each single shaft is supported by two radial and one axial AMB.

Position and speed sensors

Position sensors provide feedback to the controller about the position of the shaft relative to the bearing non-rotating parts. Each axis (or each quadrant) is equipped with one displacement sensor. The output of the sensors on opposite quadrants (180 ° apart) could be subtracted so that when they are calibrated and shaft is in the centre position null voltage is sent to the controller (SKF, 2014b).

A speed sensor provides an output proportional to the speed of rotation of the rotor. This sensor provides feedback to the controller for adjusting the speed to the desired value. The proximity-type speed sensor detects teeth on a toothed wheel or a notch on the shaft. The toothed wheel provides several pulses per one rotation of shaft while a single notch provides single pulse per rotation of the shaft. If the speed sensor provides one pulse per revolution of the rotor, it can be called Keyphasor. The Keyphasor pulse also provides phase information which is very important in diagnostics and fault finding of the equipment.

Auxiliary (backup or touch down) bearings:

When the equipment is not in operation, the shaft will be supported by these bearings. These bearings are not used during the normal operation of the equipment. In case of an emergency or process upset which causes high levels of vibration, the shaft will come into contact with the backup bearing. In case of emergency (hard landing), the shaft is supported by these bearings until the shaft stops rotation. The clearance between the shaft and the bearing is dependent on the clearance of other components such as the clearance between the rotor and seals, casing or stators. The maximum clearance of the auxiliary bearings should be designed so that the rotor does not touch the static component during normal operation or shutdown status. It should be noted that there would be a trade-off between increasing the clearances in static components such as seals as it might affect the efficiency of the equipment.

1.4.2 Controller

As magnetic attraction provided by poles of the AMB is inherently unstable, the controller must provide a feedback automatic control system to make levitation of the rotor feasible. The controller has the main function of smoothly levitating the shaft and keeping the shaft in the centre of the bearings during operation. The controller reads the position sensor outputs and compares the values with the set point defined in the controller. Based on the deviation from the set point (normally centre of the bearing), the controller sends a signal to the power amplifiers in order to provide current to the AMBs to keep the rotor at the set point location.

Figure 1-6 is a general schematic of the controller input and outputs for an AMB supported rotor. Notice the laminated plates at the bearing locations.

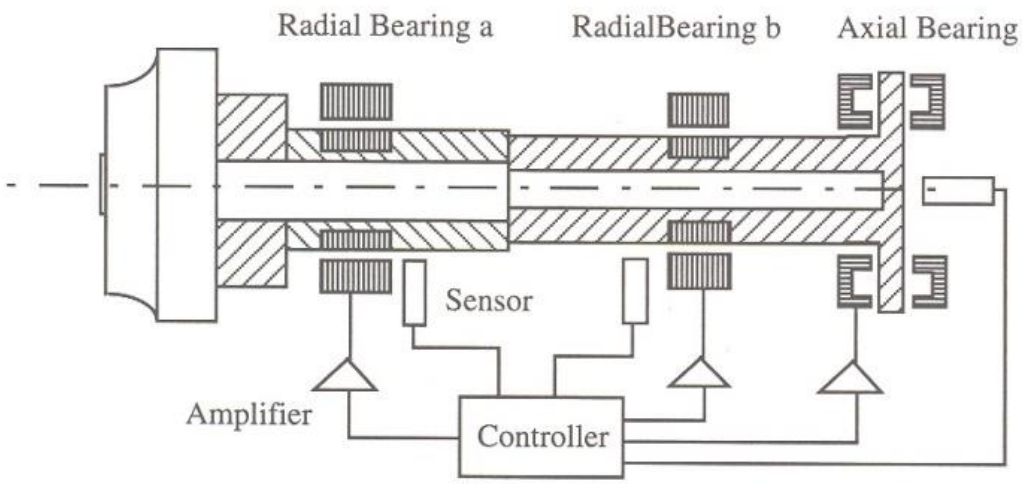

Figure 1-6: Schematic showing controller input and output in AMB supported rotors (Schweitzer, 2009).

In addition, the controller is responsible for integrity and safety of critical equipment such as tripping the rotating equipment in case of high level of vibration, over speed or other integrity-critical issues. The industrial control cabinets normally contain three modules.

- Power supply module which include power boards, batteries, protection PCBs and safety accessories.
- AMB control module which consist of controller boards and amplifiers.
- System interface module which includes communication interface and monitoring the cabinet.

An SKF E300V2 cabinet is illustrated in Figure 1-7.

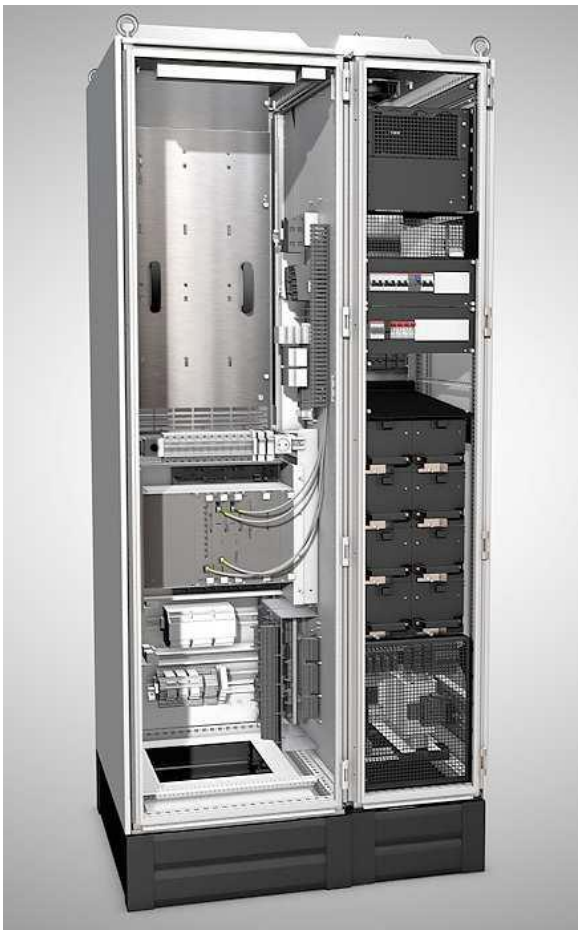

Figure 1-7: SKF E300V2 control cabinet.

The AMB digital controllers consist of different parts such as microprocessor, filters or compensators, A/D and D/A convertors, Pulse Width Modulation (PWM), etc. A simple schematic of how the controller and plant system are communicating with each other is shown in Figure 1-8.

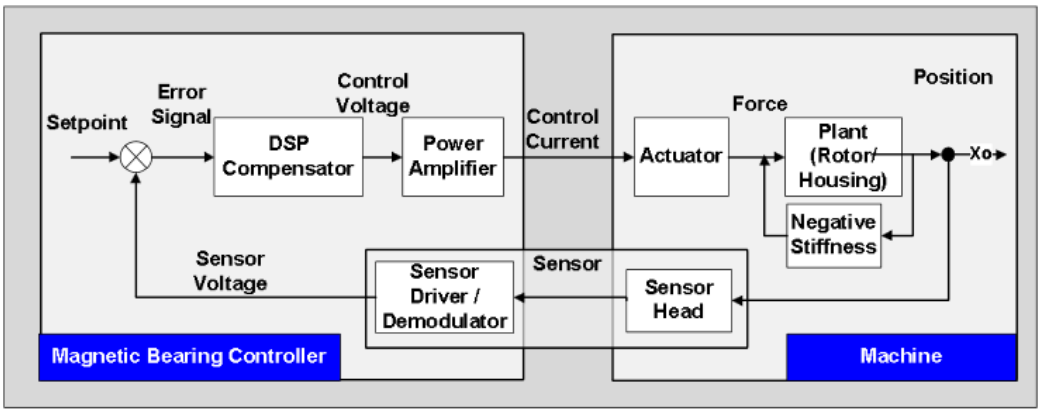

Figure 1-8: Controller and Plant System Communication (Swanson, Masala, & Hawkins, 2014)

The controller could be centralised or de-centralised. In the case of a centralised controller, inputs and outputs can have connection for different control axes. Such a controller might also be considered as Multi-Input Multi-Output (MIMO) controller. In de-centralised controllers, inputs and outputs of each control axis do not have internal connection with other control axes. This type of controller might be considered as Single-Input Single-Output (SISO). SISO is often used for control of radial AMB and is always used for control of axial AMBs (Swanson *et al*., 2014).

The controller sends command signals to the power amplifiers, which in turn power amplifier provides current to the actuators for shaft levitation. The current sensors measure the current provided to the actuators.

1.5 Research Significance and Objective

The level of knowledge and experience in industry on diagnosis of AMB supported rotor system faults is less than the knowledge and experience for diagnosis of rotors supported by fluid film bearings or roller element bearings. Currently, most rotating equipment operators are dependent on vendors to diagnose the defects in AMB rotor systems as the diagnosis knowledge is limited within their organisations. While vendors are dependent on operators' experience of plant processes and the process effect on the machinery. In addition, rotordynamic engineers are strong in analysing the rotor behaviour while control engineers are strong in solving the controller issues. AMB supported rotors show different rotordynamic behaviours compared to rotors supported by fluid film or roller element bearings. This behavioural change is completely dependent on the design and characteristic of AMB and its controller and is different case by case. As a result, diagnosis of AMB rotor system is different from other type of bearing and needs an integrated approach for solving a problem. AMB supported rotors are very reliable; however, in case of a failure in the AMB system (mechanical or controls) downtime and delays due to delays in mobilizing people to site for measurement and implementing field work can cause loss of production.

The significance of this research is to discover the essential knowledge and understanding of AMBs in relation to both controllers and the rotordynamics of rotors supported by AMBs which is necessary for diagnostics and fault finding through data acquisition and pattern recognition where limited machine-specific research has been implemented. The majority of the research done in the field of AMB supported rotors has focused on the design of the

AMB supported rotors whereas the current research takes a practical comprehensive approach on how to diagnose and troubleshoot AMB supported rotors by measuring the signals provided by the controller system. The significance and main objective of this research is to:

- to create theoretical model including mechanical and controller for extracting machine normal characteristics and integrate with practical data acquisition in particular for rotors which having elastic eigenmodes within operating speeds of the equipment .
- to apply advanced pattern recognition for diagnostics of the faults in flexible rotors running above their first bending mode.
- to provide a comprehensive approach considering all measured parameters (e.g. vibration, electrical current, speed, etc.) with which to diagnose mechanical and controller faults.

The main contribution of this research to new knowledge is as follows:

- Cover the gap between the previous research and what is required in practice in the operating companies in the field of rotordynamic diagnostics of AMB supported rotors. This will be discussed in more detail in Chapter 2 literature review.
- Provide a comprehensive practical approach in diagnostics of AMB supported machinery considering not only vibration (traditional approach) but also electrical currents and different tools that are required to diagnose the problem.
- Provide the reader the foundation knowledge for understanding the model and sensor data and how to integrate them to fault find and troubleshoot different mechanical and controller problems in AMB supported rotors.
- Demonstrate pattern recognition methods for identifying defects based on acquired sensor data on AMB supported rotor.
- Increase the AMB knowledge in Australia which can be applied in industries such as oil and gas. The state-of-the-art subsea compression units that could be used in LNG projects in Australia use AMB rotor systems.

The methodology to achieve the above mentioned goals is to:

- Create mechanical (rotordynamic) model (FEA), extract key characteristic of the rotorkit and validate the result with manufacturer datasheets and industrial standards
- Create controller model based on the component characteristics and different software values for the filter
- Integrate the controller model and rotordynamic FEA model. Compare the open loop, sensitivity of the theoretical model with measured data extracted through system identification method and compare against acceptable limits of industrial standards
- Introduce different faults such as rubbing, unbalance, misalignment and controller failure in the SKF MBRotor-II rotorkit. Study the effect of failures, identify the patterns of the faults in the acquired data and provide the method of troubleshooting and diagnostics.

1.6 Thesis Layout

This dissertation is presented in 7 chapters with the aim of providing necessary knowledge for diagnostics of AMB supported rotors. The summary of each chapter is provided as below:

Chapter 1 provided background on AMB systems and its history. Advantages and disadvantages of AMB supported rotors were described. The operation of AMB supported rotors and their modern applications, including the main components of AMB supported system, the plant system and the controller were studied. Finally, this chapter showed the research significance and objective of this study and provides the outline of the chapters.

Chapter 2 discusses the previous research and studies that were done in rotordynamic design including FEA, control of AMB supported rotors and rotordynamic diagnostics including the work done on AMB supported rotors. Rotordynamics diagnostics of AMB supported rotors has not been studied comprehensively in academia or industry which thereby provided the motivation for this research.

In Chapter 3 an introduction is provided to the SKF test rig which is used for the experimental work of this thesis. An introduction is given to the hardware and software components of the rotorkit.

Chapter 4 presents the classical rotordynamic equations of motion for a simple rotor. It is shown that even for a simple rotor the classical rotordynamic equations of motion can get very complicated. Therefore, the rotor is modelled through FEA methods considering industrial standard guidelines. The model is transformed to a state space model. The eigenvalues are extracted and verified with vendor provided values. The model is reduced to a lower number of degrees of freedom for integration with controller.

Chapter 5 derives all the hardware and software module transfer functions. This includes AMBs, sensors, power amplifier, PID compensators and filters. A Simulink model is developed to integrate the mechanical component (rotor FEA model) with the controller components. The Simulink model output is compared with experimental results extracted by injecting sweep sinusoid waveform based on ISO14839-3 (2006) recommendations.

Chapter 6 presents a comprehensive approach to diagnostics of AMB supported rotors which includes consideration of theoretical model outputs and the experimentally measured results. For this purpose an external data acquisition system is connected to the test rig to capture high resolution data. Various defects that could be simulated by the rotorkit are simulated. This includes mechanical failure modes such as rubbing to stationary part, misalignment, unbalance or controller failure modes such as non-optimal failure setting. It is demonstrated that all the sensors' data, including vibration and AMB currents, should be complemented with modelling data such as Campbell diagrams for troubleshooting the fault in the rotor system. Finally, it is shown that the stability criteria defined in ISO14839-3 (2006) and API617 (2014) is not enough to ensure continuous normal operation of the rotor system and other inputs such as open loop frequency response or root locus of poles and vibration response of the rotor should be considered in the assessment.

Chapter 7 provides a discussion, summary and conclusion of the research done in this thesis. It also discusses the possible extension of future works that could be done on SKF MBRotor-II.

Chapter 2

Literature Review

2.1 Introduction

AMB supported rotors integrate different fields of expertise such as rotordynamics and control. For modelling and diagnostics of rotors supported by AMBs, it is necessary to have knowledge in the fields of rotordynamics, control and diagnostics of equipment by sensors' data analytics. This chapter reviews the studies and work that has been done in the above-mentioned fields.

2.2 Rotordynamics

Rotordynamics is a field in mechanical engineering which analyses the vibration characteristics or motion of rotating structures. The rotating structures are different from static structures as additional forces and factors need to be considered. As an example, the cross coupling in bearings and gyroscopic forces in rotating machines makes the analysis of these structures more complicated since additional parameters must be considered. Rotordynamic history goes back to the last quarter of the 19th century when Gustaf de Laval studied the behaviour of a high speed turbine (Dimarogonas, 1992). In the 1920s, rotordynamics was heavily used in the design of turbomachinery. Currently, rotordynamic analysis of turbomachinery is mandated by different standards such as API617 (2014) for compressors, API610 (2010) for pumps, API611 (2014) for steam turbines and API616 (2011) for gas turbines in the design phase of the equipment. In these standards, specific guidelines are provided on rotordynamic analysis and acceptable vibration levels for the equipment. There have been many research papers and books in the rotordynamics field. One can refer to Childs and Childs (1993) who have studied the dynamics of rotating machines for designing turbines, pumps, compressors, etc.. In his book, the effect of gas seals and wet (liquid) seals, which are commonly used in industrial applications, are studied. Agnieszka Muszynska (2005) not only discusses the rotordynamic models, but also discusses different rotor defects such as fluid instability, rotor rub, unbalance and misalignment in rotors supported by conventional bearings.

Although classical rotordynamics had a considerable evolution in design of rotating equipment, the analyses were based on simplifications and assumptions that made the rotordynamic calculations possible. As the computational processing power became higher, the machines geometry became more complex along with a tendency towards optimisation of the assets with tighter tolerances and higher efficiency, more complicated

rotordynamic analysis was desired. Most of these analyses are based on Finite Element Methods (FEM) which can also integrate other factors such as process fluids, seals or AMB forces. Note that the basic concept and knowledge of classical rotordynamic is still required even during the FEA analysis. Subramanian, Sekhar, and Prasad (2017) have integrated centrifugal and thermal growth of labyrinth seals into rotordynamic models of gas turbines. Their modelling study shows considerable difference in the sealing coefficient. In a study by Voigt *et al*. (2017) which is a collaboration between university and industry, the rotordynamic analysis of a subsea multiphase pump/compressor is integrated with computational fluid dynamics (CFD) analysis. The designed module consists of a full scale AMB equipped with Hall sensors for precise force estimation. Štimac *et al*. (2013) modelled a flexible rotor supported by AMB system with non-collocated sensor and AMB. They extracted the frequency response of the system. They verified their model simulation result against the output of the experimental tests on a rotorkit. They corrected and optimised their model based on the experimental results. Weiler (2017) compared ANSYS workbench 18.0 and NASTRAN version 2016 capabilities in analysing rotordynamic via FEA. He concluded that these commercial software packages cannot properly handle the frequency dependent structural damping. This leads to incorrect calculation of backward whirling mode frequencies. He has also indicated that ANSYS does not provide a clear method for applying internal and external damping which might lead to misleading conclusions regarding instability.

In this dissertation, an introduction on classical rotordynamics is provided and it is shown how the equations of motion can become very complicated even for a simple one disk rotorkit. A FEA method is used for modelling the rotorkit flexible rotor that is running above its first critical speed. The rotor is simulated based on the equation of motion provided by Friswell (2010).

2.3 Control of AMBs

AMBs are a type of actuator that works with a magnetic field to keep the rotor in the centre of the bearing. The feedback controller is required to continuously read the position of the rotor, calculate the error from the desired position and send a control signal to correct the position of the rotor. The majority of AMB-supported rotors in industry use simple PID controllers in Single Input Single Output (SISO) form for each axis or in more complicated

cases Multiple Input Multiple Output (MIMO) which considers the output of all the axes together to send control signals to all the axes (Swanson *et al*., 2014). However, there are many papers in the field of AMB controllers with different complexity and stability algorithms. The μ-synthesis controller is one of the algorithm methods that has been the subject of research recently. Y. Huang (2007) has applied Model Predictive Control (MPC) in velocity form in state space equations. He has used system identification techniques (injecting signal and measurement of output) to identify the characteristics of the system. Jiancheng *et al*. (2013) have implemented a μ-synthesis control algorithm on a Double-Gimbal Control Moment Gyro. They compared the performance of the controller with a PID controller. The result of their experimental works shows the μ-synthesis controller had better performance on suppression of structural resonances. Zheng *et al*. (2015) have use Synchronous Rotating Frame (SRF) transformation for auto-balancing of the rotor. This method has better closed loop stability compared to notch filters as it only compensates for the unbalance angle. Roy *et al*. (2016) have simulated and experimentally tested Proportional Derivative high frequency band limited PD_{hfl}. They compared the performance of PD_{hfl} with a PD controller. They demonstrated that PD_{hfl} shows better levitation accuracy and unbalance response minimization. Zheng *et al*. (2017) have used a damping optimisation procedure based on the modal separation for suppression of synchronous vibration. Although this method has shown a good result for the first bending mode of the rotor, as it passed the first critical speed, the vibration increased as the speed moved toward the second bending mode of the rotor. Huang *et al*. (2015) have applied AMBs not only to control the spindle in the machining processes, but also to suppress chatter in milling processes. They applied an adaptive algorithm which is based on Fourier series analysis to suppress the chatter phenomena.

Tan and Zhang (2012) applied parameters scheduling to change the PID settings based on feedback from the rotor. The simulation results showed improvement of the performance indicators. Ji *et al*. (2008) have done a literature review on nonlinear dynamics of active magnetic bearings including non-linear self-sensing and non-linear control of magnetic bearings. They have noted the dynamic behaviour of AMB supported rotor could be significantly different from the simple linearized model.

Although there have been many advances in the field of controllers for AMB supported rotors, the majority of the industrial controllers remain PID. One reason is that in case of failure it would be easier to troubleshoot the problem. Complicated controller along with integration with the processing plant makes troubleshooting challenging. Somad (2007) has compared conventional PID controllers with advanced fuzzy controller algorithms on a MBC500 test rig. She has noted that simple PID algorithms on the MBC500 have the advantage of simplicity but it cannot damp the resonances so a notch filter was used for damping the resonance. If a non-optimal notch filter is designed, the filter will cause system instability. In addition, if the controller has a large positive phase, it has negative effect on the system.

The rotorkit in this research has a simple SISO PID for each axis equipped with various filters to damp the resonances of the rotor within or outside of the operating speed range. Different transfer functions and capabilities of the rotorkit filters will be described in future chapters.

2.4 Rotordynamics Diagnostics

Rotordynamic diagnostics is a field of study that diagnoses the problem with rotors, especially flexible rotors, by capturing vibration sensor data on the running rotating equipment. Keyphasor data, which sends one pulse per rotation of the rotor, is always required. The Keyphasor pulse, along with measured displacement vibration, provides additional information such as synchronous vibration value, associated phase, etc. This field is slightly different from rotordynamic design as it identifies the rotor behaviour by analysis of sensor data.

One of the pioneers in the field of rotordynamic diagnostics is Donald Bently. He established Bently Rotordynamics Research Corporation (BRDRC or "Birdrock") in 1981. The focus of BRDRC was mainly on machinery rotordynamic diagnostics. They studied fluid-induced instability (D. Bently & Muszynska, 1989), rotor rub against stator (Agnes Muszynska *et al*., 1989), misalignment (Campbell, 1993), shaft crack detection (D. Bently, Muszynska, & Bosmans, 1989) and developed malfunction diagnostic techniques mainly on rotors supported by fluid film bearings. Agnieszka Muszynska (2005) not only mathematically modelled different malfunctions such as fluid induced instability, whirl and whip, rotor rub against stationary components, unbalance and misalignment, she also

provided experimental case studies for rotordynamic diagnostics of these defects. D. E. Bently and Hatch (2003) provided an introduction to different types of plot applied in diagnostics in addition to methodologies to diagnose different rotordynamic problems in industry. They have provided experimental case studies that provide practical diagnostics of rotordynamic problems. However, the majority of these research papers and books were based on rotors supported by fluid film bearings.

As the quantity of rotating equipment with AMB in industry has increased, there has been more research on these types of equipment. Siva *et al*. (2018) have provided a review of the research implemented in the field of AMB rotors. They have provided an introduction on different components of AMB supported rotors, traditional vibration suppression in flexible and rigid shaft, condition monitoring of rotor-bearing system and control algorithms and their performance. They have also discussed how to identify cracked rotors with AMBs. They have introduced diagnostics methods by installing AMB on a rotor supported by journal bearings or roller element bearings. By applying AMB forces or signals and exciting the rotor, the faults in journal bearings or roller element bearings could be identified. However, in their literature review no method was identified for troubleshooting of the rotors supported by AMB system through sensor data analytics. Aenis *et al*. (2002) proposed the system identification method and its integration with model-based diagnosis techniques. The focus in their work was to put the test rig into operation. They demonstrated the simulation results for a centrifugal pump with 0%, 33% and 100% worn balance piston. However, they did not demonstrate the result of any practical experiment. The above two papers used system identification methods based on injecting signals on a levitated rotor and measurement of the displacement signal at the sensors. This provides the capability of identifying the poles (resonances) and zeros of the system. Different defects, such as cracks in the rotor, modify the resonance of the system. There are a few limitations with this method: first it identifies the system characteristics have changed. However, it does not provide the reason. Second, most often a signal can not be injected while the rotor is running. Injection of a signal might cause a high level of vibration that might trip the rotor. Finally, it cannot identify the problems that are intermittent or transient in nature. For example, aerodynamic instability might be present under a certain process condition while it might not exist in other conditions. Foreign

objects might come into contact with the rotor intermittently, depending on process conditions, thus affecting the rotor.

Downie *et al*. (2015) have studied the reliability and failure modes of AMB-supported rotor specifically the SKF MBRotor-II. The main failure modes observed in their research were related to vibration amplitudes and controller tuning of the test stand. They also applied the OREDA (Offshore [and Onshore] Reliability Data) database to compare the reliability of AMB supported compression trains with a conventional compressor configuration. P. S. Keogh (2012) has studied the contact between rotor and backup bearings. He also demonstrated that in the case of contact of the rotor with its backup bearing, if the controller remains in operation, the contact dynamic response is different compared with cases where the rotor drops onto the backup bearing. He also studied the effect of thermal bend through analytical tools and transfer functions and provided the stability envelope.

Based on ISO14839-4 (2012) rotors can show three types of behaviour when they contact Touch Down Bearings (TDB) or backup bearing - Full rub, pendulum vibration and combination of rub and pendulum motion. Liu, Lyu, Wang, and Yan (2018) have modelled and simulated the orbit response of rotors to identify these three types of rotor contact behaviour. Lyu *et al*. (2018) have simulated the orbit response of the rotor during the touchdown. They have extracted the mean and local variance of Instantaneous Frequency based on the Hilbert Transform. Based on mean and variance values they identified the type of contact of the rotor with TDB. However, their studies need to be validated with experimental results. Sun *et al.* (2017) applied machine learning methods to estimate the dynamic behaviour of a rotor touch down based on experimental studies. Most of the above mentioned research considers just the contact between a rotor and the auxiliary bearings but lack full analysis of the experimental data such as spectrum plots or data sources such as AMB current data.

Bouaziz *et al.* (2011) have theoretically modelled the behaviour of misaligned rotors. In their studies, they demonstrated that rotor shows 2X and 4X superharmonic peaks predominant in spectrum plots for AMBs with four, six and eight magnets. The number of magnets has a linear relationship with the magnitude of peaks and that a decrease of air gap affects the second harmonic. Spangler *et al.* (2017) have used bias current perturbation methods for defining the magnetic centre of the AMB. The proposed solution is based on

the behaviour of a small number of selected points for defining the effective air gap that compensates the difference between the theoretical model output and the measurement results. Halminen *et al.* (2015) have studied the effect of misaligned cage less auxiliary bearings. They have shown if the misalignment between the auxiliary bearings is more than 75% of the air gap, the touchdown would lead to complete functional failure of the equipment. There has been limited research on misalignment of two casings in a machine string using consideration of the sensor data, including displacement and current data.

Gouws (2013) has applied Cepstrum analysis, Wigner-Ville Distributions (WVD) and enveloped Equi-Sampled Discrete Fourier Transforms (ESDFT) for condition monitoring of different components of AMB systems. Based on this research, Cepstrum analysis provided good results in finding vibration issues at all frequencies. WVD provided good results for high amplitude and high frequency defects. ESDFT provided good results for small amplitude low frequency defects.

2.5 Summary

This chapter provided an overview of the research that has been done in the field of rotordynamics, AMB controllers and rotordynamic diagnostics. The previous research focus was mainly on design and implementation of controllers. Many types of AMB controller algorithm have been designed and implemented. However, less attention has been paid to diagnostics of rotors supported by AMBs. Most of the attention of the research was on design of the rotors and controllers or improvement of control algorithms. System identification methods have some limitations which were stated earlier. There has been less focus on rotordynamic fault diagnostics through sensor data analytics.

This research takes a comprehensive approach to diagnostics and troubleshooting of AMB supported rotors. It incorporates all diagnostic sensor data such as displacement (position), current signal and average and instantaneous gap voltage and AMB current values. In addition, frequency spectrum plots, waterfall plots and orbit plots are considered which can provide insight to excitation frequencies. The measured data is integrated with modelling and simulation data for the purpose of diagnostics. Industrial standards are used as a benchmark and guideline for assessment of the condition of the complete AMB-supported system.

There has been limited research on sensor data analytics of contact between the rotor and stator in locations other than auxiliary bearings, such as seals and stator. There are situations where external objects come in contact with bearing through the process fluid. In this research, contact between the rotor and the static component located between the two AMBs is considered while controller still in operation.

There has been no research on non-optimal controller settings, its effect on the rotordynamic behaviour of the rotor and how to identify and troubleshoot this type of problem. This study provides a case study and a method of identifying and troubleshooting the controller issues.

Chapter 3

SKF Rotorkit MBRotor-II and the Controller MB340g4-ERX

3.1 Introduction

During the course of this thesis, a SKF test stand is modelled, simulated and the experimentally diagnosed by creating known defects on the test rig. For these reasons it is important to have an understanding of the hardware and software modules and operation of the rotorkit necessary for modelling, simulation and diagnostics. In this chapter general information about the SKF MBRotor-II supported by the MB340g4-ERX controller is provided. Note that the SKF controller and its software which was used in this research is a replica of the controller used for industrial applications such as turbo-molecular pumps.

3.2 SKF Test Stand Hardware

The SKF MBRotor-II is controlled by an MB340g4-ERX controller. The SKF test stand (MBRotor-II) rotating components consist of a rotor and a disk between inboard and outboard AMBs. The rotor includes the main part and two stub shafts which are within the bearings. There is provision for balancing the rotor at the disk (Figure 3-1). The rotor is flexible and the nominal speed range is between approximately 350 rpm to 12000 rpm. The vendor maximum recommended operating speed is 9000 rpm. The rotor passes its first critical speed (first bending mode) at a speed of approximately 6360 rpm (106 Hz) as it is accelerates to the operating speed of 9000 rpm.

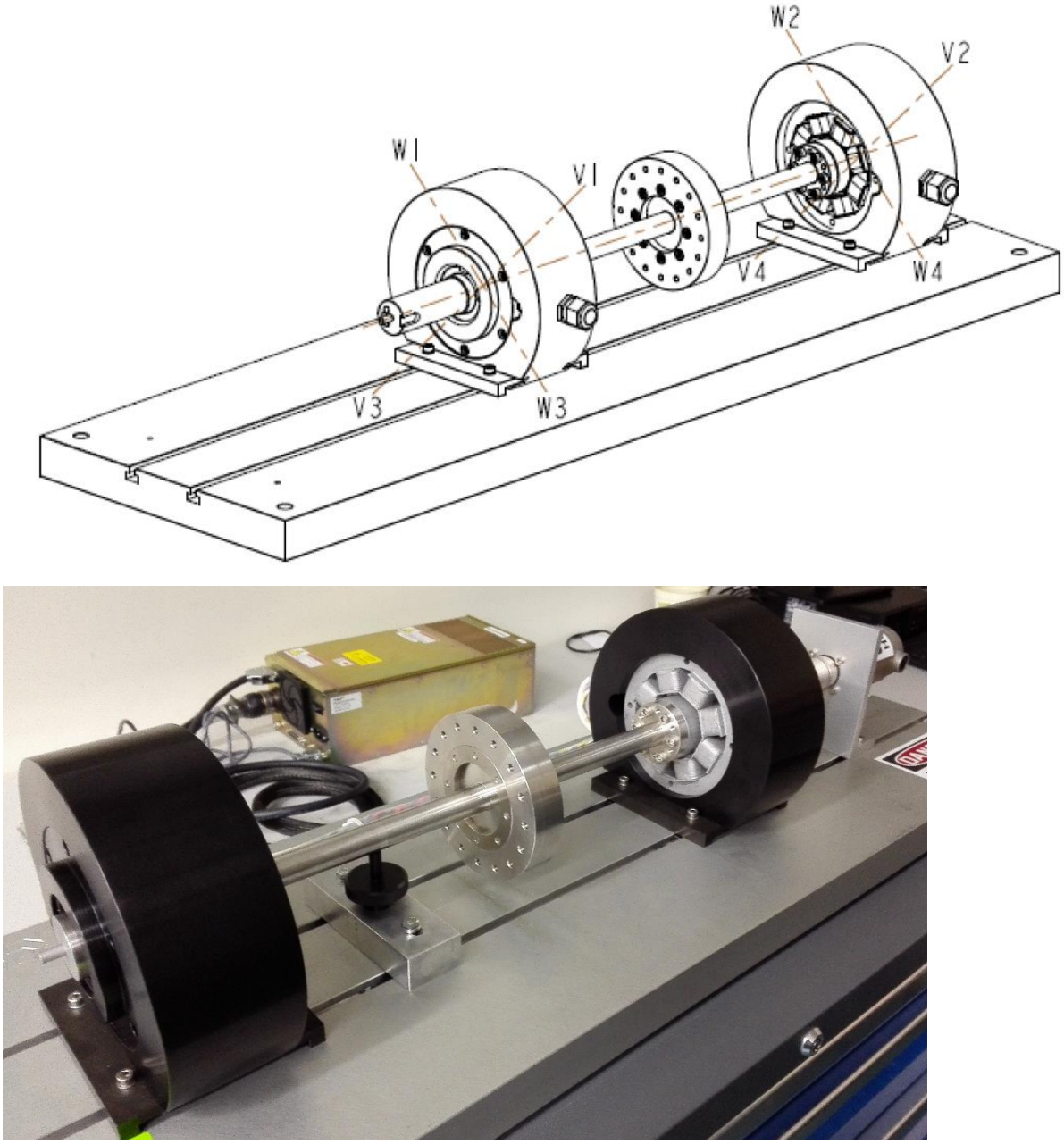

Figure 3-1: SKF test stand MBRotor-II schematic (SKF, 2014b) and MBRotor-II picture

The SKF test stand supports the rotor by two radial AMBs. The AMBs are responsible for levitating and controlling the rotor centre at running speed or while the rotor is not turning. The coils in each quadrant are wound in series which provides four electromagnets (quadrants) on each bearing. Each quadrant is considered to have one axis and the electromagnets are arranged at a 45 degree angle from the vertical direction (SKF, 2014b) (Figure 3-1 and Figure 3-2). One of the reasons for this arrangement is that the weight of the shaft is distributed across the quadrants. The magnetic poles are running in low flux density which by applying the bias control current, the electromagnetic forces would be

linear with control current. In case of high current, there would be cross coupling between the poles that will cause non-linearity of the pulling forces (Ren, Bian, & Liu, 2008). In practice, the cross couplings are negligible and these are addressed in commissioning and calibration of the equipment before start-up. The details of controller current stiffness and negative displacement stiffness for the test stand AMBs will be provided in Chapter 5.

Each quadrant has one position sensor which provides feedback to the controller for levitating and keeping the rotor in the centre of AMB. Each AMB quadrant has one axis which is in line with the opposite quadrant axis. In other words, pairs of magnets are diametrically opposed. For control purposes the axes of opposite quadrants are considered as one since they are in the same direction. For example, both V1 and V3 axes, which are inline, are defined as V13. The inboard AMB axes (driver end AMB) are V13 and W13, right and left of the vertical axis respectively (driver to driven end point of view) and the outboard bearing axes (non-driver end AMB) are V24 and W24, right and left of vertical axis respectively (driver to driven end point of view) as demonstrated in Figure 3-1.

For detailed information, cross sections, components and drawings of the SKF test stand refer to Appendix 1.

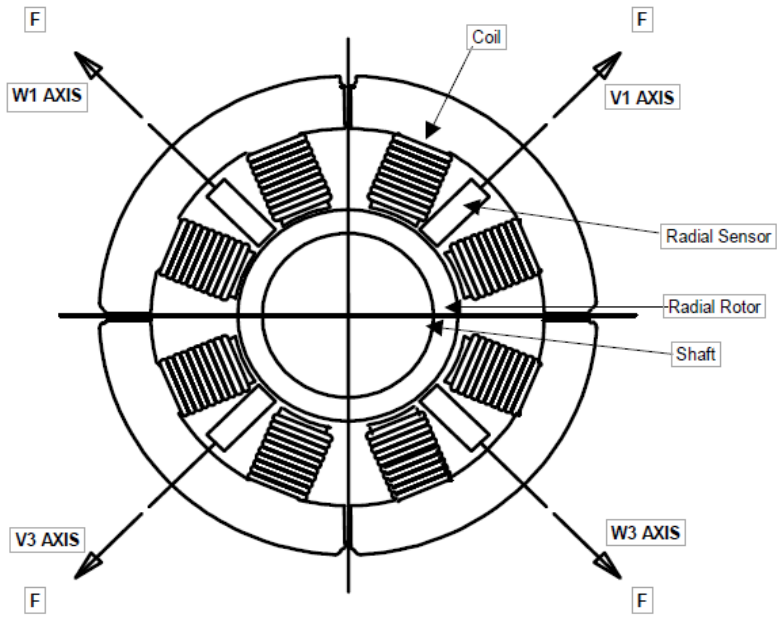

Figure 3-2: AMB sensor and electromagnet arrangement in SKF test stand (viewed from driver to driven) (SKF, 2014b)

Figure 3-3 shows the SKF controller, MB340g4-ERX. The MB340g4-ERX controller acquires position and speed sensor signals and provides outputs to the motor and AMB actuators. The controller is capable of controlling five axes; however, the test stand axial movement is controlled by the motor through the coupling. The four radial axes have a de-centralised control algorithm. In other words, each axis has a Single Input Single Output (SISO) controller with its own parameters. For controlling the position of the rotor within its bearings, the controller has different hardware and software components. The command signal adds and subtracts control current from a steady bias current for the opposing electromagnets (each opposing quadrant on each axis) so that the magnetic force is increased on one pole while it is reduced on the opposing pole as a result of control current added to or subtracted from the bias current of opposite electromagnets. This type of current control is defined as differential mode control.

In order to provide smooth levitation and support of the rotor by AMBs, different control and filter parameters need to be configured. Different parameters on each individual axis provides the capability of having different stiffness and damping on each axis of the AMB. Normally though, the parameters for two axes of a single AMB are the same while the parameters may differ for the two AMBs supporting the shaft. This is a consequence of different external forces, with different magnitudes, which are exerted on the rotor. Examples of such external forces are uneven distribution of gravity forces or uneven process forces interacting with the rotor.

The controller parameters of the MB340g4-ERX are configured in the MBScope software suite. The major software modules of the MB340g4-ERX are explained in the software section 3.3.

Figure 3-3: SKF MB340g4-ERX Controller.

3.3 SKF Test Stand Software

The SKF MBRotor-II is controlled by MB340g4-ERX controller. The tuning parameters of the MB340g4-ERX are configured and tested through the MBScope software suite. The software suite has different modules for configuration, monitoring and calibration of the controller settings which are described in this section.

3.3.1 MBScope - Configuration Module

In the Configuration Module, the controller PID and filter parameters can be configured. These parameters are configured under the Configuration Panel - SISO tuning tab (Figure 3-4). Each axis has its own parameters that are configured individually. The PID - proportional component is similar to the spring stiffness of a fluid film bearing, the PID - integrator component is for removing the steady state error, and the PID - derivative component is similar to the damping component of a fluid film bearing. The purpose of the lead-lag or lag-lead filters is to respectively increase or decrease the phase and gain between the zero and pole of the transfer function. The lead lag filter may be used as an alternative to the derivative component for damping the resonances in the running speed range of the shaft. The low pass filter attenuates the gain and phase of the transfer function above the low pass frequency. The low pass filter can make the system quieter as it removes the high frequency signals; however, it can have a negative effect as it reduces

the phase lead that might reduce the damping of the system. Generic 2nd order or notch filters are used to attenuate the effect of resonances outside the operating speed of the rotor. It should be noted that this filter must not be used for damping the resonance of the rotor within the operating range of the rotor. Each axis can have up to four generic 2nd order or notch filters. Figure 3-5 depicts the generic 2nd order and notch filter setting for V13 axis which is defined in Figure 3-1. The PID settings and filter transfer functions will be discussed in Chapter 5.

The controller also is responsible for controlling the rotation speed. The controller determines the speed from the Keyphasor notch and adjusts the speed by a PID controller. The Keyphasor is a tachometer that sends one pulse per rotation of the shaft. In this case not only is the speed measured but also the phase of the vibration which is an important parameter in diagnosing rotordynamic faults. The setting for the motor are defined in the Motor Control tab; these include the PID parameters and speed control parameters such as run, idle, minimum and maximum speed in addition to acceleration.

The alarm (trip) and alarm delay settings are adjusted in the Alarm Settings tab.

Confidential vendor-supplied data removed from this publically accessible electronic copy.

A reader seeking that data should contact SKF directly.

Figure 3-4: MBScope - Configuration Panel.

Confidential vendor-supplied data removed from this publically accessible electronic copy.

A reader seeking that data should contact SKF directly.

Figure 3-5: Generic 2nd order and notch filter setting for V13 axis.

3.3.2 MBScope – Analyzer Module

The Analyzer software module provides different transfer function plots of the controller for each axis. These transfer function plots are used for assessment of controller performance. The software injects a sweep signal internally and provides transfer functions such as open loop, closed loop, and sensitivity transfer functions. These are important criteria that show the mechanical and control characteristics of the combined system. These transfer functions could also be assessed based on the criteria defined by ISO14839, although, it is a very low power machine.

The maximum speed of the SKF Test Stand is 12000 rpm (200 Hz) and the MB340g4-ERX has a sampling frequency of 8 kHz. Therefore the assessment frequency range based on ISO14839-3 (2006) is in the range of 0-2 kHz. The stability of the controller and rotor system, along with the controller transfer function and settings, will be discussed further in Chapter 5.

Figure 3-6 shows the Analyzer software module for extracting different axis transfer functions.

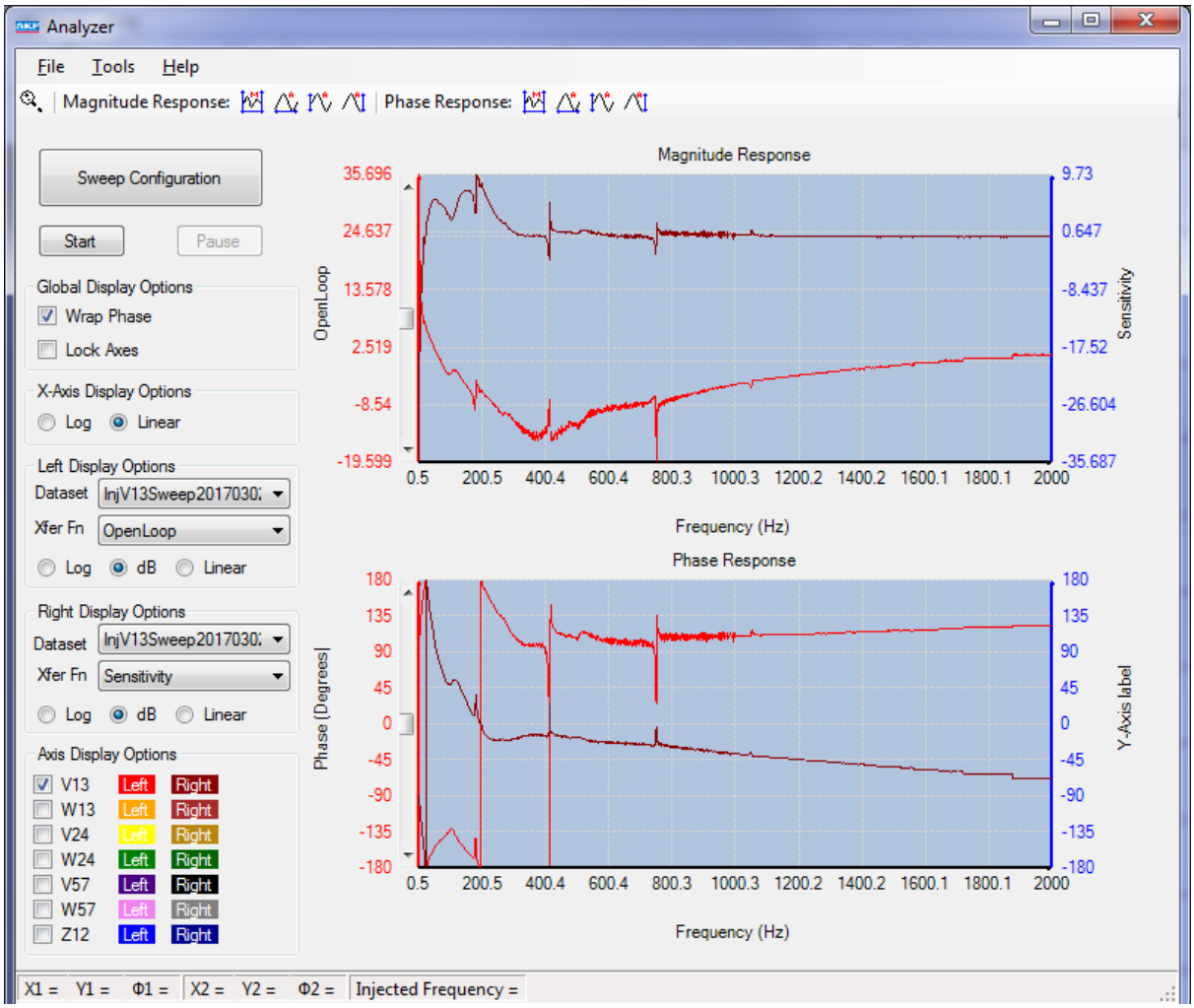

Figure 3-6: Analyzer software module for extracting system transfer functions.

3.3.3 MBScope – Calibration

The MBScope Calibration module has the capability of measuring and calibrating the scale factors of the position sensors. The sensors may be calibrated automatically or manually by moving the rotor to touch the auxiliary bearings and adjust the scale factors accordingly. The scale factor of the position sensors, their setpoints and other parameters is accessed through the calibration software. These scale factors are also required for simulation purposes (will be discussed in Chapter 5) and for configuration of the DAQ (will be discussed in Chapter 6). A screenshot of calibration module is shown in Figure 3-7.

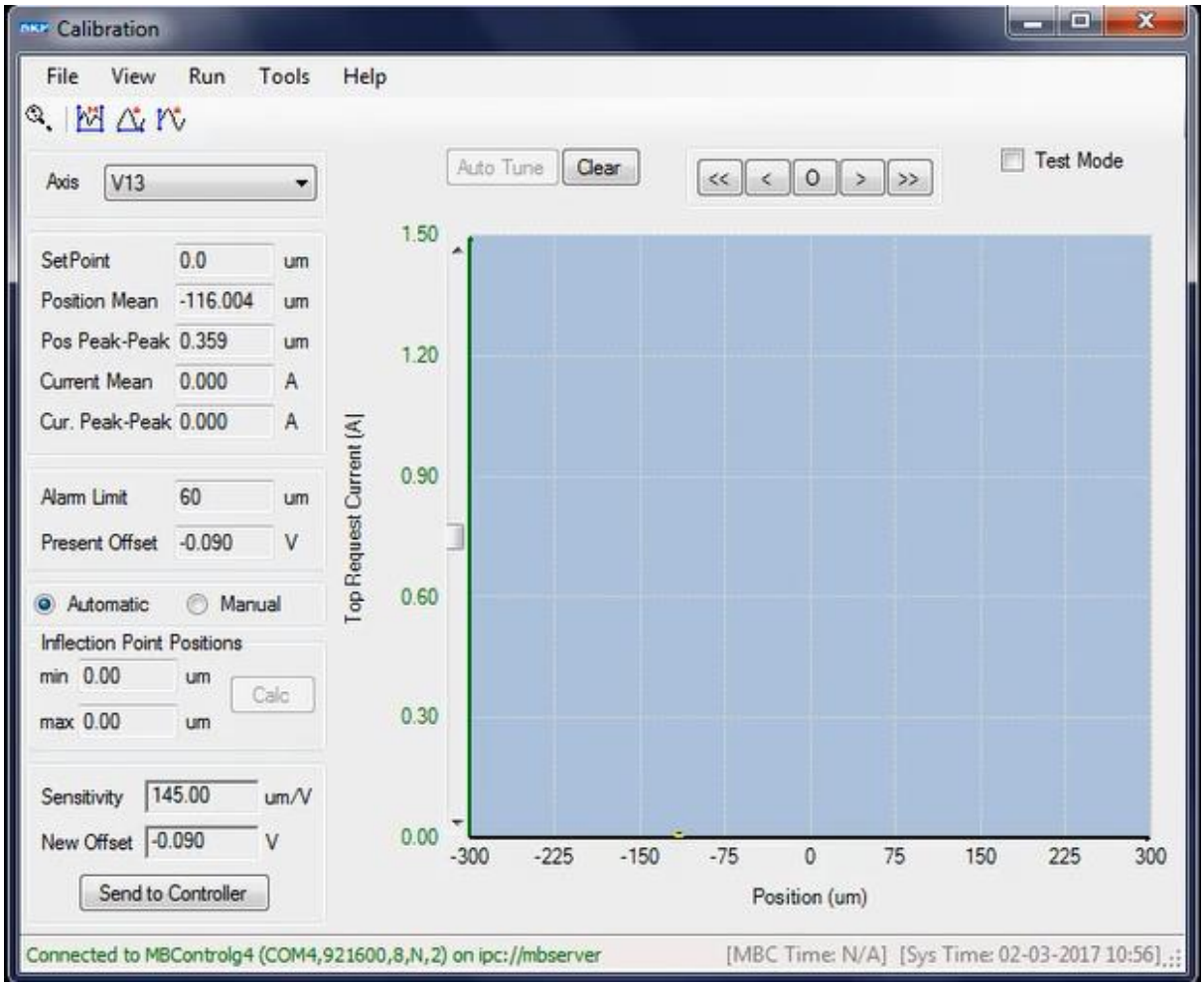

Figure 3-7: Calibration software for the position sensors.

3.3.4 MBScope – Trending

MBScope Trending provides trending information for different measured parameters such as vibration, current, and speed. This module's capacity for providing trend information is inadequate for diagnostics purposes as it does not have the capability of providing trend data for all channels simultaneously. Therefore, it is necessary to capture high resolution data using an external DAQ device for diagnostics.

3.4 MBResearch Output

Figure 3-8 shows the MBResearch module which provides the BNC connectors for measurement of different parameters such as position (vibration) and AMB current values. As mentioned in section 3.3.4, an external data acquisition (DAQ) device is connected to these BNC connectors to acquire high resolution sensor data. These outputs are providing valuable data for analysis and diagnosis of the rotor system which is discussed in Chapter 6.

Figure 3-8: MBResearch BNC outputs for position and current measurement.

3.5 Scope of Work on MBRotor-II in This Research

MBRotor-II has a rotor that can rotate at a speed above its first bending mode frequency. Therefore, modelling of the rotor should be undertaken so that it includes this mode. To

levitate the rotor by the AMBs, there is a need for a controller with closed feedback loop. The MB340g4-ERX controller continuously measures the position of the rotor in each bearing, compares the feedback with the set point and send compensation signals to the actuators, which are the two AMBs, for reducing the error or deviation from set point. The controller has different components such as PID compensator, different filters such as lead-lag, low band pass, generic 2^{nd} order, power amplifier which sends the signals to AMBs to levitate the rotor at stand still or at operating speed.

In this research, the MBRotor-II rotor is studied in detail and modelled in Chapter 4. In Chapter 5 the MB340g4-ERX controller compensators and other components are modelled in detail and integrated with the mechanical components. Finally, different mechanical and controller faults are created experimentally on the rotorkit and the pattern of the failures are studied in Chapter 6.

3.6 Summary

In this chapter an overview of SKF rotorkit which was used for the experimental studies of this thesis was provided. In summary, the rotor with the mass disk can operate above its first bending mode frequency. The rotor is supported radially by two AMBs which are responsible for levitating the rotor and keeping the rotor in the centre of the bearing while running. For keeping the rotor in the AMBs' centre, the controller reads the rotor position and provides feedback control signals to keep levitating the rotor. The controller settings can be adjusted through different software modules dedicated to configuration, calibration and monitoring.

Chapter 4

Rotordynamic Modelling and FEA

4.1 Introduction

Rotordynamic modelling and Finite Element Analysis (FEA) of rotors is one of the primary and most important parts of designing rotating equipment. The rotordynamic analysis of rotors dates back to 1919 where H.H. Jeffcott studied the lateral vibration of a simple shaft in the neighbourhood of a whirling speed (Jeffcott, 1919). This “modal model” is still used in industry as a simple explanation of rotordynamic response of flexible rotors to unbalance and for diagnostics purposes (D. E. Bently & Hatch, 2003; Agnieszka Muszynska, 2005). One of the most important steps in designing critical industrial rotating equipment is the rotordynamic analysis. This step is becoming more essential as the demand for higher power and efficiency of rotating equipment is increasing which leads to tighter tolerances between the rotor and static parts. Normally, the rotordynamic study and design of rotors are done numerically through FEA methods.

Understanding the fundamentals of rotordynamics is important in designing and diagnostics of AMB supported rotors. In this chapter, an introduction is provided to FEA of the SKF MBRotor-II rotor. However, extracting complete equations of motion and coupled equations of motion is beyond the scope of this thesis and the reader might need to refer to Agnieszka Muszynska (2005) and Friswell (2010) for more detail on rotordynamic and FEA matrices extraction.

The FEA model of the AMB-supported rotor is an input to the design, selection and optimisation of AMB controller parameters and filters. In this chapter, the classic simplified rotordynamic equations of motion for a simple rotor are demonstrated. The mass, stiffness, damping and force matrices for the SKF rotor are then extracted through the FEA method. These matrices are integrated into the rotordynamic equations of motion which provides the free-free behaviour of the rotor. The eigenvalues of the model are compared against vendor provided values. Finally, a model reduction technique is used to reduce the model degrees of freedom (DOF) which can then be used for integrating with the controller transfer function.

4.2 Rotordynamic Equation of Motion

In this section the rotordynamic equation of motion for a simple rotor with a disk is extracted. The lateral and angular equations of motion are derived to extract critical frequencies of the shaft and stability criteria. It is shown that considering gyroscopic forces

couples angular displacement equations. If the gyroscopic forces are also considered in lateral displacement vibration (which is beyond the scope of this thesis), all lateral and angular vibration responses will be coupled together. This makes these equations very complicated to solve even for a simple rotor. However, it is important that the reader understand the type and number of critical frequencies of a simple rotor. The reader is encouraged to refer to Muszynska (1995) and Friswell (2010) for more details on extraction of equations of motion.

Figure 4-1 depicts a simple two lateral mode isotropic (the same characteristics in both x and y direction) rotor without gyroscopic forces with negligible shaft mass. The general lateral rotordynamic equation of motion in the horizontal (x) and vertical (y) directions may be extracted as in equations (4-1) and (4-2) by summing forces in those direction (Agnieszka Muszynska, 2005):

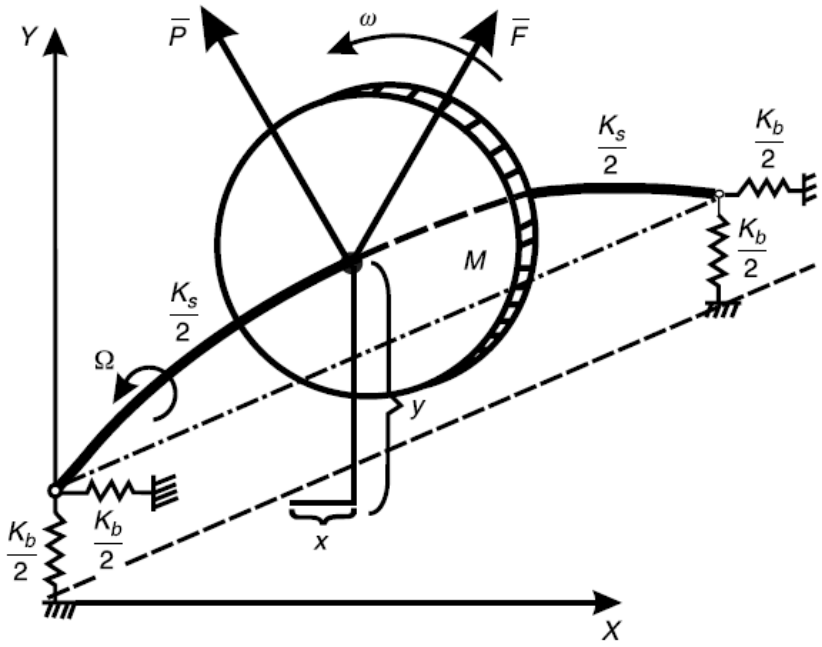

Figure 4-1: Simple two lateral isotropic rotor (Agnieszka Muszynska, 2005)

$$M\ddot{x} + D_s\dot{x} + Kx = Fcos(\omega\, t + \delta\,) + P cos\gamma \tag{4-1}$$

$$M\ddot{y} + D_s\dot{y} + Ky = Fsin(\omega\, t + \delta\,) + P sin\gamma \tag{4-2}$$

where:

M : modal mass

K : lateral isotropic stiffness (include contributions of K_s isotropic elastic rotor and K_b isotropic elastic support)

D_s : external lateral damping (without gyroscopic damping)

F : magnitude of rotating external excitation force

ω : frequency of the external rotating force which might be different from shaft rotation frequency (Ω)

δ : the initial phase of rotating external excitation force

P : magnitude of constant magnitude and direction radial load force

γ : angular orientation (measured from the x axis) of the external radial constant load force P

An insightful method of solution is to substitute x and y with two conjugate variables (equations (4-3), (4-4)) which generates equations (4-5) and (4-6):

$$r_1 = x + jy \tag{4-3}$$

$$r_2 = x - jy \tag{4-4}$$

$$M\ddot{r_1} + D_s\dot{r_1} + Kr_1 = Fe^{j(\omega\, t+\delta)} + Pe^{j\gamma} \tag{4-5}$$

$$M\ddot{r_2} + D_s\dot{r_2} + Kr_2 = Fe^{-j(\omega\, t+\delta)} + Pe^{-j\gamma} \tag{4-6}$$

The above equations are decoupled from each other. In addition, the dynamic external exciting forces are in opposite directions. The force that is rotating in the same direction as the rotation of the shaft is called the forward mode and the force that is rotating in the opposite direction of the rotation of the shaft is called the backward mode. Since it is assumed the rotor is isotropic, by substituting equation (4-7) in (4-5) and (4-6) and extracting the characteristic equation without excitation forces (F=0, P=0) provides the

rotor free response or the eigenvalues which can be used for assessing the stability condition of the rotor:

$$r_1 = r_2 = Re^{st} \tag{4-7}$$

$$Ms^2 + D_s s + K = 0 \tag{4-8}$$

The eigenvalues are:

$$s_{1,2} = -\frac{D_s}{2M} \pm \mathrm{j}\sqrt{\frac{K}{M} - \frac{{D_s}^2}{4M^2}} = \sigma \pm \mathrm{j}\omega_d \tag{4-9}$$

A similar procedure using complex conjugate provides another pair of eigenvalues equal to the above equation thanks to the assumption that the rotor is isotropic. If the damping and stiffness in the x and y directions are different (non-isotropic rotor) then these two pairs of eigenvalues will be different.

The direct (real) part of the eigenvalues is the growth/decay rate with a unit of 1/s and the quadrature (imaginary) part of eigenvalue is the damped natural frequency with a unit of rad/s (D. E. Bently & Hatch, 2003). The direct part of the equation is responsible for stability of the rotor free transverse vibration. If the direct part is positive the rotor is unstable and if the direct part is negative the rotor is stable. If the direct part is equal to zero, the system is at the threshold of instability. In practice, the rotor instability could be checked by an impulse force. If the rotor vibration decays, the rotor is stable.

If the damping ratio ($\zeta = \frac{D_s}{2\sqrt{KM}}$) is greater than 1, the rotor is overdamped and will not have vibration oscillatory motion.

The free response vibration of the rotor based on r_1, r_2 is equal to:

$$r_1 = R\, e^{\gamma t} e^{j\omega_d t} \tag{4-10}$$

$$r_2 = R\, e^{\gamma t} e^{-j\omega_d t} \tag{4-11}$$

where R is a constant displacement vector that depend on the initial condition of free vibration.

In order to extract the forced response to forward circular nonsynchronous excitation considering the static force is equal to zero, the solution is extracted as follows. The response to a nonsynchronous excitation is a general response, which in the special case of unbalance, the frequency of the excitation force would be the same as unbalance response frequency.

$$r_1 = Re^{j(\omega t+\alpha)} \tag{4-12}$$

$$r_2 = Re^{-j(\omega t+\alpha)} \tag{4-13}$$

where R and α is the magnitude and phase of forced response.

Substituting into the extracted equations of motion (4-5) and (4-6):

$$Re^{j\alpha} = \frac{Fe^{j\delta}}{K - M\omega^2 + jD_s\omega} \tag{4-14}$$

$$Re^{-j\alpha} = \frac{Fe^{-j\delta}}{K - M\omega^2 - jD_s\omega} \tag{4-15}$$

The amplitude and phase of vibration are extracted as follows:

$$R = \frac{F}{\sqrt{(K - M\omega^2)^2 + D_s^2\omega^2}} \tag{4-16}$$

$$\alpha = \delta - \arctan\frac{D_s\omega}{K - M\omega^2} \tag{4-17}$$

The complex dynamic stiffness (CDS) could be extracted as follows:

$$CDS = K - M\omega^2 \pm jD_s\omega = \frac{F}{R}e^{\pm j(\delta-\alpha)} \tag{4-18}$$

Note that at the undamped natural excitation frequency, the mass and stiffness cancel each other and the response phase lags the excitation force by 90 degrees. API684 (2005) mentions that damped natural frequency is different from undamped natural frequency; however, in practical turbomachinery these two frequencies are considered approximately equal if the mode shape indicates that the journal motion in its bearing is less than 5% of the shaft mid-span displacement.

The above equations considered just the isotropic rotor lateral displacement response in the plane perpendicular to the rotor axis at the disk location. Rotors also show angular displacement as they bend during their lateral vibration. The angular vibration displacement for an isotropic rotor with a heavy disk and massless shaft supported by anisotropic supports may be extracted as below (Agnieszka Muszynska, 2005) based on the coordinate system convention shown in Figure 4-2:

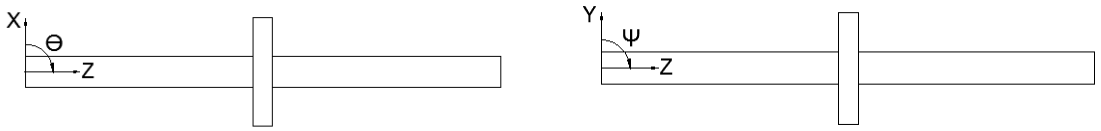

Figure 4-2: Coordinate System convention for equation of motion

$$I_T\ddot{\theta} + \Omega I_P\dot{\psi} + D_{s\theta}\dot{\theta} + K_\theta\theta = -\Omega^2(I_P - I_T)\chi\cos\left(\Omega t + \delta_\chi\right) \quad (4\text{-}19)$$

$$I_T\ddot{\psi} - \Omega I_P\dot{\theta} + D_{s\psi}\dot{\psi} + K_\psi\theta = -\Omega^2(I_P - I_T)\chi\sin\left(\Omega t + \delta_\chi\right) \quad (4\text{-}20)$$

I_T: Transverse Moment of inertia

I_P: Polar moment of inertia

Ω: The rotor angular velocity

ψ: Angular displacement in (y,z) plane

θ: Angular displacement in (x,z) plane

$D_{s\theta}, D_{s\phi}$: External angular damping

K_θ, K_ϕ: Anisotropic angular stiffness in two directions combining rotor and the support

δ_χ: The initial angle between the rotor axis and the skewed disk axis

χ: Rotor disk skewed position projected on (x,y) plane

The gyroscopic moments $\Omega I_P\dot{\psi}$, $-\Omega I_P\dot{\theta}$ couple the equations (4-19), (4-20) and are dependent on the rotor rotation speed. A skewed disk creates an unbalanced moment that is similar to an unbalanced mass in linear lateral vibration. For the rotor with a skewed disk, the vibration amplitude and phase response may be extracted by substituting equations (4-21) and (4-22) in equations (4-19) and (4-20) - similar to the solution for lateral

displacement vibration – resulting in equations (4-23), (4-24) and (4-25), (4-26) (Agnieszka Muszynska, 2005):

$$\psi = R_{\psi}\cos(\Omega t + \alpha_{\psi}) \tag{4-21}$$

$$\phi = R_{\phi}\sin(\Omega t + \alpha_{\phi}) \tag{4-22}$$

$$R_{\psi} = \frac{\chi\Omega^2|I_T - I_P|\sqrt{\left(\left(K_{\phi} - \Omega^2(I_T + I_P)\right)^2 + D_{s\phi}^2\Omega^2\right)}}{\sqrt{\left[(K_{\phi} - \Omega^2 I_T)(K_{\psi} - \Omega^2 I_T) - \Omega^4 I_P^2 - D_{s\phi}D_{s\psi}\Omega^2\right]^2 + \Omega^2\left[D_{s\phi}(K_{\psi} - \Omega^2 I_T) + D_{s\psi}(K_{\phi} - \Omega^2 I_T)\right]^2}} \tag{4-23}$$

$$R_{\phi} = \frac{\chi\Omega^2|I_T - I_P|\sqrt{\left(\left(K_{\psi} - \Omega^2(I_T + I_P)\right)^2 + D_{s\psi}^2\Omega^2\right)}}{\sqrt{\left[(K_{\phi} - \Omega^2 I_T)(K_{\psi} - \Omega^2 I_T) - \Omega^4 I_P^2 - D_{s\phi}D_{s\psi}\Omega^2\right]^2 + \Omega^2\left[D_{s\phi}(K_{\psi} - \Omega^2 I_T) + D_{s\psi}(K_{\phi} - \Omega^2 I_T)\right]^2}} \tag{4-24}$$

$$\alpha_{\psi} = \delta + \frac{\arctan\left(D_{s\phi}\Omega\right)}{K_{\phi} - \Omega^2(I_T + I_P)} - \frac{\arctan\Omega\left[D_{s\phi}\left(K_{\psi} - \Omega^2 I_T\right) + D_{s\psi}\left(K_{\phi} - \Omega^2 I_T\right)\right]}{\left(K_{\phi} - \Omega^2 I_T\right)\left(K_{\psi} - \Omega^2 I_T\right) - \Omega^4 I_P^2 - D_{s\phi}D_{s\psi}\Omega^2} \tag{4-25}$$

$$\alpha_{\phi} = \delta + \frac{\arctan\left(D_{s\psi}\Omega\right)}{K_{\psi} - \Omega^2(I_T + I_P)} - \frac{\arctan\Omega\left[D_{s\psi}\left(K_{\phi} - \Omega^2 I_T\right) + D_{s\phi}\left(K_{\psi} - \Omega^2 I_T\right)\right]}{\left(K_{\phi} - \Omega^2 I_T\right)\left(K_{\psi} - \Omega^2 I_T\right) - \Omega^4 I_P^2 - D_{s\phi}D_{s\psi}\Omega^2} \tag{4-26}$$

It may be shown that the rotor orbit in response to a skewed disk that is like an unbalance that has backward and forward components. The rotor skewed disk unbalance-like resonances, where damping is neglected, may be extracted as below:

$$\Omega_1 = \sqrt{\frac{K_{\theta}}{I_T + I_P}} \tag{4-27}$$

$$\Omega_2 = \sqrt{\frac{K_{\psi}}{I_T + I_P}} \tag{4-28}$$

The simple rotor has two lateral and two angular eigenvalues which can be considered separately due to the simplifying assumptions. In the above examples the lateral and angular vibration and their equations of motion were studied separately and the coupling between the lateral and angular equations of motion were neglected by making

assumptions that simplified the equations. In the real case, the rotor equations of motion for both lateral and angular vibration displacement are coupled because the rotor mass, skewed disk and unbalance all act at the same time. Extracting and solving the coupled rotordynamic equations parametrically and finding the solution for these rotors is complicated (Friswell, 2010). Numerical methods such as FEA are applied as an alternative approach for solving the complicated parametric equations of motion which will be explained in the next section.

4.3 FEA Model of the Rotor

In the FEA model, the rotor model is divided to smaller elements where each element has the properties of the rotor explained in the previous section. These elements are assembled together to create the mass, stiffness and damping matrices and integrating them to the equation of motion. Much academic and industrial research has been done in the field of FEA. The FEA modelling method that was applied in this research was developed by Friswell *et al.* of which more details may be found in Friswell (2010). The general equation of motion containing element matrices are applied in the FEA model is shown in equation (4-29).

$$[\boldsymbol{M}]\ddot{\boldsymbol{q}} + [\boldsymbol{C}]\dot{\boldsymbol{q}} + [\boldsymbol{K}]\boldsymbol{q} = \boldsymbol{f} \tag{4-29}$$

where:

$\boldsymbol{q}$ is displacement vector consisting of lateral and angular displacements at each node based on the coordinate system convention defined in Figure 4-3 for each element.

$$q = [u\ v\ \theta\ \psi]^T \tag{4-30}$$

Figure 4-3: Coordinate system convention for FEA nodes

$[\boldsymbol{M}]$, $[\boldsymbol{C}]$, $[\boldsymbol{K}]$ are the mass, damping and stiffness matrices respectively.

$\boldsymbol{f}$ is the external force vector which includes unbalance, lateral forces such as process forces, in addition to the AMB magnetic bearing forces.

$[\boldsymbol{C}]$ includes both damping and gyroscopic matrices. The skew symmetric gyroscopic matrix, which depends on the rotational velocity, captures the gyroscopic effect which couples the rotational degrees of freedom perpendicular to the spin axis. In other words, a change in the vertical dynamics of the rotor influences the horizontal dynamics of the rotor system. Gyroscopic moments cause the natural frequency of the rotor to increase since they depend on rotational speed.

$[\boldsymbol{K}]$ includes both rotor stiffness and the skew symmetric circulatory matrix which also depends on rotational velocity and modifies apparent stiffness of the structure and can produce unstable motion. Skew-symmetric stiffness element also depend on internal damping. Refer to Friswell (2010) and Genta (2007) for detailed information.

u, v are lateral displacement of the shaft from the equilibrium position in the x and y directions respectively.

θ, ψ are positive rotation around the x and y axes respectively.

For the FEA analysis of the SKF MBRotor-II rotor different possible software platforms were investigated. The aim was to extract mass, stiffness, damping and gyroscopic matrices required for analysis of the rotor system by the integration of the mechanical components (rotor) with the AMB controller system. Among these software packages considered were ANSYS and different toolboxes such as Dynamic Properties of Rotating Structures by von Groll (1995) and the rotordynamic toolbox, developed as a part of the book by Friswell (2010). It was necessary to have the desired accuracy in the calculated results and be able to have the mass, stiffness, damping and gyroscopic matrices extracted separately. The Friswell rotordynamic toolbox was chosen for the above criteria and its accompanying book clarifies the equations of motion that are required for manipulating the equations for AMB supported rotors.

Based on the model created with this toolbox, each shaft element has two nodes at each end and has four degrees of freedom as per equation (4-30). The axial vibration, including axial displacement and torsional vibration, have not been considered in this research. The axial movement of the rotor is constrained by the motor through the coupling and no measurement is available on the rotorkit for both torsional and axial vibration. Based on

Friswell (2010) the mass, stiffness and damping matrices for shaft elements considering shear and rotary inertia are define as below:

$$M_e = \frac{\rho A l}{840(1+\phi_e)^2}\begin{bmatrix} m_1 & 0 & 0 & m_2 & m_3 & 0 & 0 & m_4 \\ 0 & m_1 & -m_2 & 0 & 0 & m_3 & -m_4 & 0 \\ 0 & -m_2 & m_5 & 0 & 0 & m_4 & m_6 & 0 \\ m_2 & 0 & 0 & m_5 & -m_4 & 0 & 0 & m_6 \\ m_3 & 0 & 0 & -m_4 & m_1 & 0 & 0 & -m_2 \\ 0 & m_3 & m_4 & 0 & 0 & m_1 & m_2 & 0 \\ 0 & -m_4 & m_6 & 0 & 0 & m_2 & m_5 & 0 \\ m_4 & 0 & 0 & m_6 & -m_2 & 0 & 0 & m_5 \end{bmatrix} + \frac{\rho l_e}{30\, l_e(1+\phi_e)^2}\begin{bmatrix} m_7 & 0 & 0 & m_8 & -m_7 & 0 & 0 & m_8 \\ 0 & m_7 & -m_8 & 0 & 0 & -m_7 & -m_8 & 0 \\ 0 & -m_8 & m_9 & 0 & 0 & m_8 & m_{10} & 0 \\ m_8 & 0 & 0 & m_9 & -m_8 & 0 & 0 & m_{10} \\ -m_7 & 0 & 0 & -m_8 & m_7 & 0 & 0 & -m_8 \\ 0 & -m_7 & m_8 & 0 & 0 & m_7 & m_8 & 0 \\ 0 & -m_8 & m_{10} & 0 & 0 & m_8 & m_9 & 0 \\ m_8 & 0 & 0 & m_{10} & -m_8 & 0 & 0 & m_9 \end{bmatrix} \quad (4\text{-}31)$$

Where:

$$\mathrm{m}_1 = 312 + 588\,\phi_\mathrm{e} + 280\,\phi_\mathrm{e}^2$$

$$m_2 = (44 + 77\,\phi_e + 35\,\phi_e^2)l_e$$

$$m_3 = 108 + 252\,\phi_e + 140\,\phi_e^2$$

$$m_4 = -(26 + 63\,\phi_e + 35\,\phi_e^2)l_e$$

$$m_5 = (8 + 14\,\phi_e + 7\,\phi_e\phi_e)l_e^2$$

$$m_6 = -(6 + 14\,\phi_e + 7\,\phi_e^2)l_e^2$$

$$m_7 = 36$$

$$m_8 = (3 - 15\,\phi_e)l_e$$

$$m_9 = (4 + 5\,\phi_e + 10\,\phi_e^2)l_e^2$$

$$m_{10} = (-1 - 5\,\phi_e + 5\,\phi_e^2)l_e^2$$

$$K_{0e} = \frac{E_e I_e}{(1+\phi_e) l_e^3} \begin{bmatrix} 12 & 0 & 0 & 6l_e & -12 & 0 & 0 & 6l_e \\ 0 & 12 & -6l_e & 0 & 0 & -12 & -6l_e & 0 \\ 0 & -6l_e & (4+\phi_e)l_e^2 & 0 & 0 & 6l_e & (2-\phi_e)l_e^2 & 0 \\ 6l_e & 0 & 0 & (4+\phi_e)l_e^2 & -6l_e & 0 & 0 & (2-\phi_e)l_e^2 \\ -12 & 0 & 0 & -6l_e & 12 & 0 & 0 & -6l_e \\ 0 & -12 & 6l_e & 0 & 0 & 12 & 6l_e & 0 \\ 0 & -6l_e & (2-\phi_e)l_e^2 & 0 & 0 & 6l_e & (4+\phi_e)l_e^2 & 0 \\ 6l_e & 0 & 0 & (2-\phi_e)l_e^2 & -6l_e & 0 & 0 & (4+\phi_e)l_e^2 \end{bmatrix} \quad (4\text{-}32)$$

$$K_{1e} = \frac{E\, I_e \beta}{(1+\phi_e) l_e^3} \begin{bmatrix} 0 & 12 & -6\,l_e & 0 & 0 & -12 & -6\,l_e & 0 \\ -12 & 0 & 0 & -6\,l_e & 12 & 0 & 0 & -6\,l_e \\ 6\,l_e & 0 & 0 & (4+\phi_e)l_e l_e & -6\,l_e & 0 & 0 & (2-\phi_e)l_e l_e \\ 0 & 6\,l_e & -(4+\phi_e)l_e l_e & 0 & 0 & -6\,l_e & -(2-\phi_e)l_e l_e & 0 \\ 0 & -12 & 6\,l_e & 0 & 0 & 12 & 6\,l_e & 0 \\ 12 & 0 & 0 & 6\,l_e & -12 & 0 & 0 & 6\,l_e \\ 6\,l_e & 0 & 0 & (2-\phi_e)l_e l_e & -6\,l_e & 0 & 0 & (4+\phi_e)l_e l_e \\ 0 & 6\,l_e & -(2-\phi_e)l_e l_e & 0 & 0 & -6\,l_e & -(4+\phi_e)l_e l_e & 0 \end{bmatrix} \quad (4\text{-}33)$$

$$C_{0e} = \beta\, K_{0e} \quad (4\text{-}34)$$

$$C_{1e} = -\frac{\rho\, I_e}{15\, l_e\, (1+\phi_e)^2} \begin{bmatrix} 0 & -g_1 & g_2 & 0 & 0 & g_1 & g_2 & 0 \\ g_1 & 0 & 0 & g_2 & -g_1 & 0 & 0 & g_2 \\ -g_2 & 0 & 0 & -g_3 & g_2 & 0 & 0 & -g_4 \\ 0 & -g_2 & g_3 & 0 & 0 & g_2 & g_4 & 0 \\ 0 & g_1 & -g_2 & 0 & 0 & -g_1 & -g_2 & 0 \\ -g_1 & 0 & 0 & -g_2 & g_1 & 0 & 0 & -g_2 \\ -g_2 & 0 & 0 & -g_4 & g_2 & 0 & 0 & -g_3 \\ 0 & -g_2 & g_4 & 0 & 0 & g_2 & g_3 & 0 \end{bmatrix} \quad (4\text{-}35)$$

Where:

$$g_1 = 36$$

$$g_2 = (3 - 15\,\phi_e) l_e$$

$$g_3 = (4 + 5\,\phi_e + 10\,\phi_e^2) l_e^2$$

$$g_4 = (-1 - 5\,\phi_e + 5\,\phi_e^2) l_e^2$$

In the above equations:

M_e is the element mass matrix

K_{0e} is the element stiffness matrix

K_{1e} is the skew-symmetric speed dependent element stiffness matrix from the internal damping

C_{0e} is the element damping matrix

C_{1e} is the element gyroscopic matrix

l_e is the length of the element

E is the Young's modulus

ρ is the mass density

ϕ_e is the shear coefficient

I is the moment of inertia

β is the rotor damping factor

If the disk is not an integral part of the shaft, or it is not shrink-fitted to the rotor, it has negligible effect on the stiffness of the rotor; however, it affects the mass matrix and gyroscopic matrix. Below are the equations that show the mass and gyroscopic matrices for a disk that does not affect the stiffness of the rotor:

$$M_d = \begin{bmatrix} m_d & 0 & 0 & 0 \\ 0 & m_d & 0 & 0 \\ 0 & 0 & I_d & 0 \\ 0 & 0 & 0 & I_d \end{bmatrix} \tag{4-36}$$

$$G_d = \begin{bmatrix} 0 & 0 & 0 & 0 \\ 0 & 0 & 0 & 0 \\ 0 & 0 & 0 & I_p \\ 0 & 0 & I_p & 0 \end{bmatrix} \tag{4-37}$$

where:

M_d is the disk mass matrix

G_d is the disk gyroscopic matrix

4.4 FEA guidelines and standards

This section reviews the FEA modelling recommendations and guidelines that are made within various industrial standards. Although these recommendations are for industrial

equipment, especially the API which is mainly followed in oil and gas industries, it has been considered for modelling of the MBRotor-II which is a laboratory-sized equipment.

API 684 Second edition (API684, 2005) provides recommendations on how to model rotor – bearing systems. For simple rotordynamic analysis, two types of elements should be considered in creating the complete rotor model: shaft elements that have influence on stiffness, mass and inertia, and the disk elements that contribute to mass and inertia. It is evident that the optimum number of elements should be used in analysis. If the number of elements chosen is less than required, it will cause inaccurate results while a high number of elements can cause numerical issues in addition to increasing the time of computation. Based on the recommendation provided by this standard, the number of stations (nodes) should be at least four times the number of desired modes if the program is applying the transfer matrix method. In addition, the length to diameter ratio should not exceed 1.0 (0.5 is preferred) and should not be less than 0.1. If the effect of an element is negligible in the analysis result (e.g. grooves), this feature may be ignored during modelling. In the rotor modelling, the centre of gravity of the seal, coupling, etc. should be considered as the appropriate location of mass. If the location of the coupling is beyond the shaft, elements of low mass with high stiffness could be considered. In flexible and gear type couplings, the hub is considered as a part of the shaft, while flexible joints are considered as a spring in a flexible coupling. If the sleeves, collars, impellers, etc. are shrink-fitted on the shaft, and the length of the component is large, then the contributing stiffness of the part should be considered in the modelling.

Based on the requirement by API 617-part I (2014), undamped lateral vibration analysis is required to determine undamped critical speeds and mode shapes. This analysis should define the first four undamped critical speeds and should include analysis of support stiffness ranging from 0.1X to 10X of the expected support stiffness. In addition a damped unbalanced response analysis should be implemented for the speeds of 0 to 150% of the maximum continuous speed. However, for AMB-supported rotors based on ISO14839-3 (2006) the peak sensitivity (defined in section 5.9) in the range of frequency of 2 kHz or three times the rated speed, whichever is greater, should be studied. In addition, if the actuator and sensors are not collocated in the modelling of flexible rotors, this standard recommends considering the location of the sensor and the actuator (AMB) separately. In

API 617-part I - section 4.8.2.7 the locations and the values that the unbalance should be placed for different shaft configurations is defined. For symmetric modes, the unbalance is based on the sum of the journal static loads, and for the asymmetric modes the unbalance is 180 degrees out of phase and the magnitude is based on the static load on the adjacent bearing. For overhung shafts it is based on the overhang mass.

4.5 Recommendations applied to SKF MBRotor-II Test Rig

SKF MBRotor-II rotor dimensions and component materials are provided in the SKF manual and datasheets. In order to reduce the effect of eddy currents induced by the AMBs, the rotor is mounted by insulated laminations at the bearing locations. The laminated plates add mass to the rotor system but their effect on the stiffness of the rotor is negligible. Therefore, the laminated plates are considered just as mass at the nodes (yellow colour) as shown in Figure 4-4. The disk consists of two sections. One part is integral with the shaft as a single piece and the other part is a hub, which is bolted to the smaller diameter disk as shown in Figure 3-1. The integral part of the disk with the shaft contributes to the mass and stiffness of the rotor while the latter contributes only to the mass and inertia of the rotor. There is a part of the hub that is not located at a node (similar to an overhang mass) and just the outer diameter and inner diameter is considered in the analysis. In this case the mass and inertia of this element is considered in the analysis while the stiffness is negligible. The distribution of the mass is based on the thickness of the disk and length of the elements. The final FEA model of the SKF MBRotor-II rotor model has 76 elements as shown in Figure 4-4. The disk and element matrices are integrated and the complete rotor assembly is created to provide the mass, stiffness and damping matrices. The FEA model has 77 nodes where each node has 4 degrees of freedom (DOF) as per equation (4-30). Therefore; the total number of DOFs for the complete rotor assembly is 308. The maximum length to diameter ratio is 0.5 while the recommended minimum is 0.1.

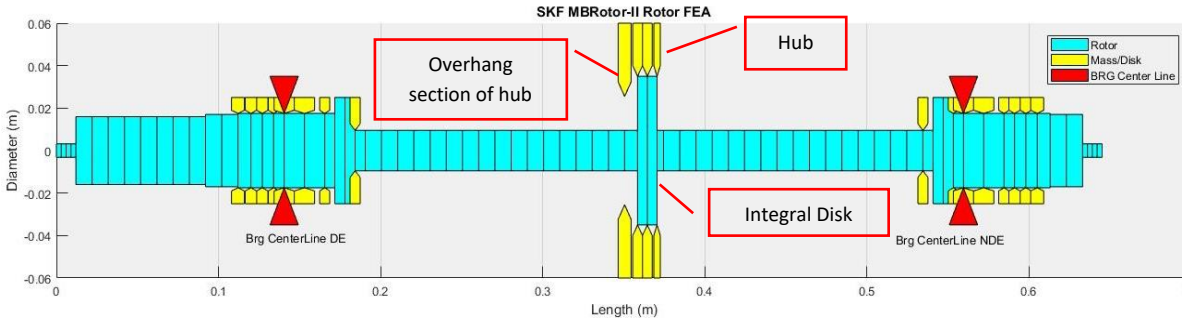

Figure 4-4: FEA model of the SKF MBRotor-II showing the rotor, disk and bearing locations. Coupling (drive) end is on the left.

4.6 State Space Analysis

For extracting the eigenvalues and also integrating the rotor FEA model with the controller, it is necessary to convert equation (4-29) to state space format. Equation (4-29) may be stated as follows (Swanson *et al.*, 2014):

$$[\boldsymbol{M}]\{\ddot{\boldsymbol{q}}\} + [\boldsymbol{C}]\{\dot{\boldsymbol{q}}\} + [\boldsymbol{K}]\{\boldsymbol{q}\} = \boldsymbol{f_{amb}} + \boldsymbol{f_{ext}} \tag{4-38}$$

where the following parameters are extracted from equation (4-31) to (4-37) and incorporated as follows:

$[\boldsymbol{K}] = K_0 + \Omega\, K_1$

$[\boldsymbol{C}] = C_0 + \Omega\, C_1$

Ω is the rotation speed of the rotor

f_{amb} AMB forces exerted on the rotor

f_{ext} Process forces, external forces or unbalance

The 308 DOF second order differential equations can be converted to 2x308 first order differential equations – the state space format (Hatch, 2000):

$$\begin{bmatrix}\dot{q}\\ \ddot{q}\end{bmatrix} = \begin{bmatrix}0 & I\\ -M^{-1}K & -M^{-1}C\end{bmatrix}\begin{bmatrix}q\\ \dot{q}\end{bmatrix} + \begin{bmatrix}0\\ M^{-1}B_s\end{bmatrix}u_{AMB} + \begin{bmatrix}0\\ M^{-1}f_{ext}\end{bmatrix}u_{ext}$$
$$Y_{sens} = C_s\begin{bmatrix}q\\ \dot{q}\end{bmatrix} + D_s \tag{4-39}$$

The following parameters are defined based on the above equation.

$$A_s = \begin{bmatrix} 0 & I \\ -M^{-1}K & -M^{-1}C \end{bmatrix} \tag{4-40}$$

$$B_{s,act} = \begin{bmatrix} 0 \\ M^{-1}B_s^* \end{bmatrix} \tag{4-41}$$

$$B_s^* = \begin{bmatrix} 0 & 0 & 0 & 0 \\ \vdots & \vdots & \vdots & \vdots \\ 1 & 0 & 0 & 0 \\ 0 & 1 & 0 & 0 \\ \vdots & \vdots & \vdots & \vdots \\ 0 & 0 & 1 & 0 \\ 0 & 0 & 0 & 1 \\ \vdots & \vdots & \vdots & \vdots \\ 0 & 0 & 0 & 0 \end{bmatrix} \begin{matrix} \\ \\ dof\ of\ actuator\ x\ direction \\ dof\ of\ actuator\ y\ direction \\ \\ dof\ of\ actuator\ x\ direction \\ dof\ of\ actuator\ y\ direction \\ \\ \end{matrix} \tag{4-42}$$

$$B_{s,ext} = \begin{bmatrix} 0 \\ M^{-1}f_{ext} \end{bmatrix} \tag{4-43}$$

Since the AMB forces are independent of each other and process forces acting on the rotor are independent from each other as well, the B_s could be assembled as follows (Hatch, 2000):

$$B_s = [B_{s,act}(:,1,2) \quad B_{s,ext} \quad B_{s,act}(:,3,4)] \tag{4-44}$$

$$C_s = [C_{sensor}\ 0]$$

$$C_{sensor} = \begin{bmatrix} 0 & \dots & 1 & 0 & \cdots & 0 & 0 & 0 \\ 0 & \dots & 0 & 1 & \dots & 0 & 0 & 0 \\ 0 & \dots & 0 & 0 & \dots & 1 & 0 & 0 \\ 0 & \dots & 0 & 0 & \dots & 0 & 1 & 0 \end{bmatrix} \tag{4-45}$$

where columns containing 1 are the DOF columns of sensor axis in C_{sensor} or the location that the measurement of state is desirable.

$$D_s = [0] \tag{4-46}$$

The MBRotor-II is running above its first bending mode and as such the location of the AMB input is different from the location of the sensor. The MBRotor-II position sensor and AMB actuation point are not collocated. Therefore, different nodes are considered as AMB input and as position sensors outputs.

4.7 Extracting Eigenvalues and Eigenvectors for Free-Free Rotor

The free-free analysis of the rotor system provides essential information related to the natural frequencies and mode shapes of the rotor system. In a free-free analysis, the eigenvalues and eigenvectors of the rotor are extracted with the condition of no support (no bearing) and the rotor is at stand still (0 rpm). This is achieved by calculating the eigenvalues and eigenvectors of matrix A_s in equation (4-40).

The analysis of the rotor at stand still is one of the main differences between analysis of rotors supported by conventional bearings (roller element bearing or fluid film bearing) and AMBs. The AMB control system can excite a resonance of the rotor even when the rotor is not rotating by inducing electromagnetic forces with a frequency equal to one of the resonances of the rotor. In addition it is important to observe the mode shapes to verify whether a mode shape node is situated between a position sensor and an actuator of the bearing. This parameter is important in assessment of controllability of the rotor. If a node is situated between the actuator location and the sensor location in the operating speed range of the rotor, the sensor will read the position of the shaft at the actuator location 180 degrees out of phase as indicated in Figure 4-5.

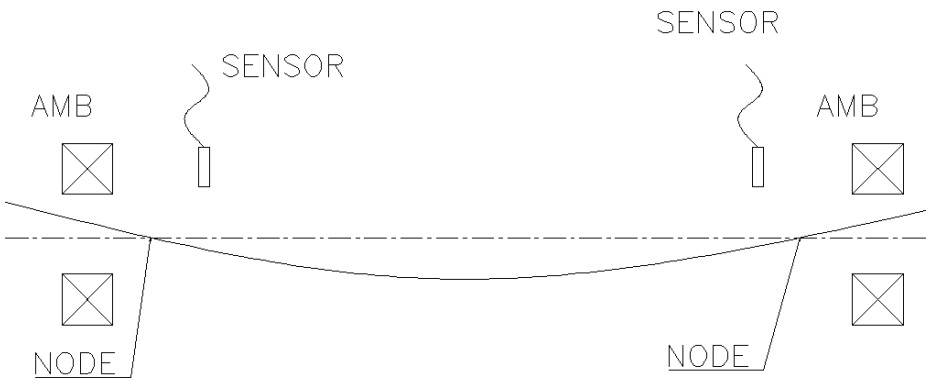

Figure 4-5: Nodes on right and left side of the rotor are located between sensor and bearing causing vibration reading to be of out of phase (Not applicable to MBRotor-II).

The eigenvalues of free-free rotor are extracted from the FEA model by calculating the eigenvalues of matrix A_s. These values are compared against vendor-provided values in Table 4-1. The calculated values have less than 2% difference from the SKF-provided rotordynamic analysis report (SKF, 2014a). Therefore, this FEA model is considered suitable for integration with the control system dynamic model. The small differences might be

related to how boundary conditions are considered on the disk and the equations of motion applied for extracting the FEA matrices.

Table 4-1: Eigenvalues of free-free rotor FEA model compared to SKF-provided values

Mode/Type	SKF Rotordynamic Natural Frequency (Hz)	Free-Free FEA Natural Frequency (Hz)	% Difference
1st mode /Rigid	0	0.0012	-
2nd mode /Rigid	0	0.0094	-
3rd mode /Flexible	108	107.8	0.2
4th mode /Flexible	403	410.8	1.9
5th mode /Flexible	746	754.4	1.1
6th mode /Flexible	1133	1149	1.4

The rotor mode shapes are shown in Figure 4-6 for the frequencies below 2 kHz. There are no nodes located between the sensor reading position and the actuator locations. This could also be determined from the Bode plot by considering the location of zeros and poles and their order (Bleuler et al., 2009). If the Bode plot shows two poles without a zero between them or two zeros without any pole between them, it indicates that there is a node between the sensor and the actuator (Bleuler et al., 2009) in that frequency range. The Bode plot of the free-free rotor for V13 Actuator force as the input (N) and V13 sensor as the output (m) is demonstrated in Figure 4-7. No nodes between the sensor and actuator in operating range of the rotorkit are observed.

The natural frequencies of the system are dependent on the distribution of mass, stiffness and damping matrices and not on the location the input forces are applied or where the output is measured. Therefore, the natural frequencies of the system are constant for all the extracted transfer functions of the rotor system. The zeros, where the locations that vibration amplitude of the rotor is minimal, are dependent on the numerator of the transfer function which is dependent on where the output is measured. The gain and phase of the transfer functions can be extracted by vector product of distances from all zeroes to the intended frequency multiplied by dc gain (Hatch, 2000).

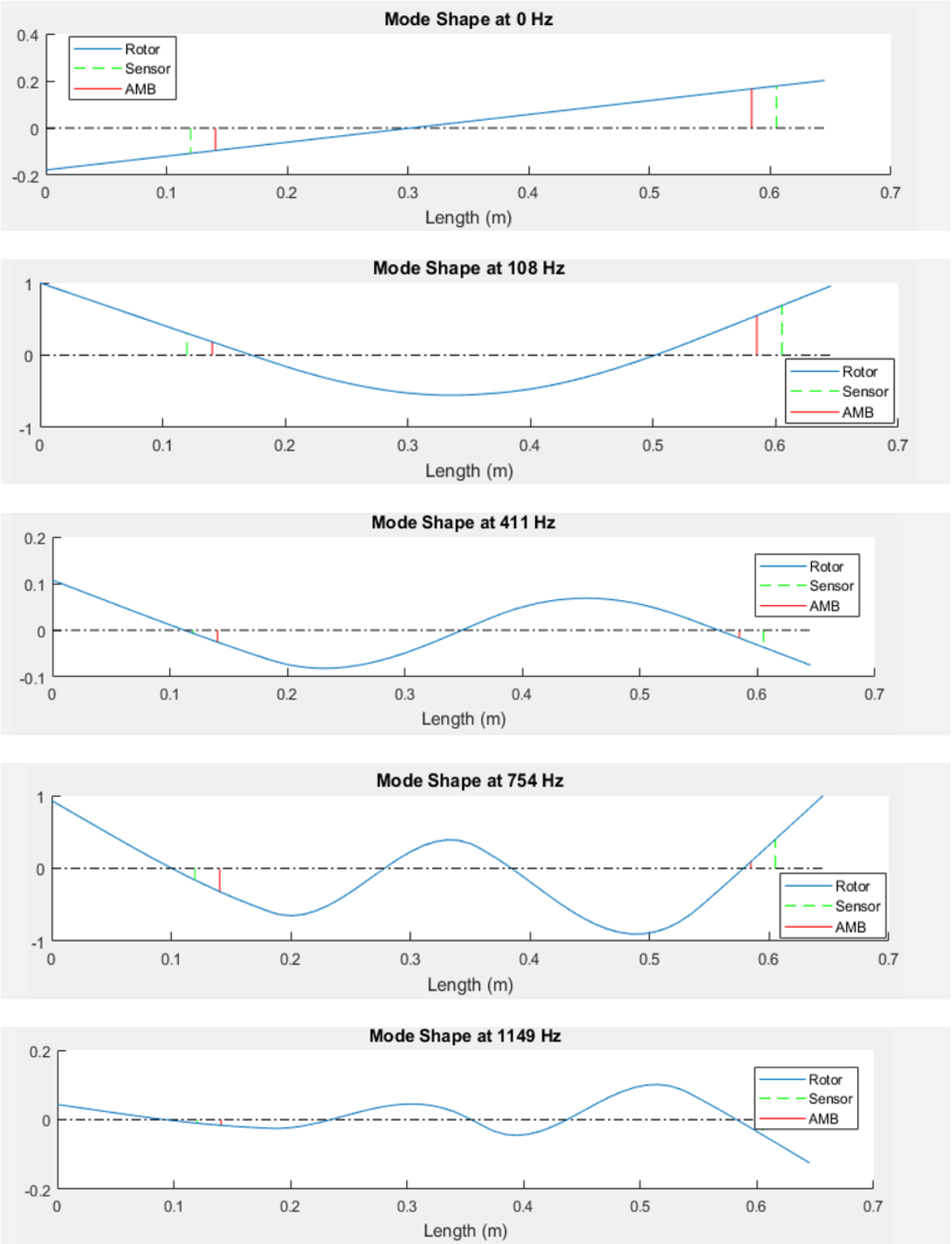

Figure 4-6: MBBRotor-II mode shapes below 2000 Hz

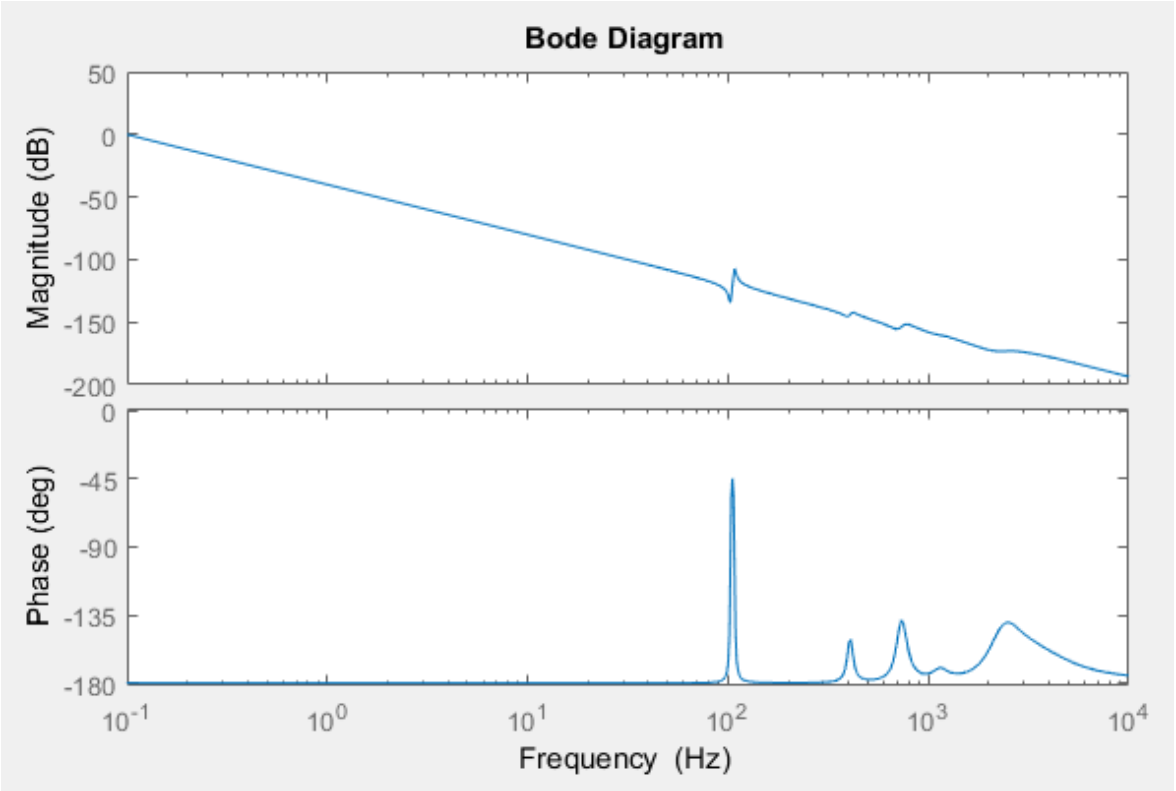

Figure 4-7: Bode plot of free-free rotor system (Input force V13 Actuator (N), Output measurement at V13 Sensor (m)) (0 dB=1 m/N)

4.8 Defining Desirable Bearing Stiffness

Figure 4-8 shows the variation of rotor natural frequencies with changes in AMB stiffness at stand still condition. This plot can be used for defining the target stiffness for AMBs. Based on this plot a value of approximately 0.5-1 MN/m would be appropriate. At this stiffness the first three modes show slope which indicates there is a balance of strain energy between the bearing stiffness and the rotor stiffness (Bleuler et al., 2009). Bleuler has not provided more details on the balance of strain energy between rotor and bearing stiffness.

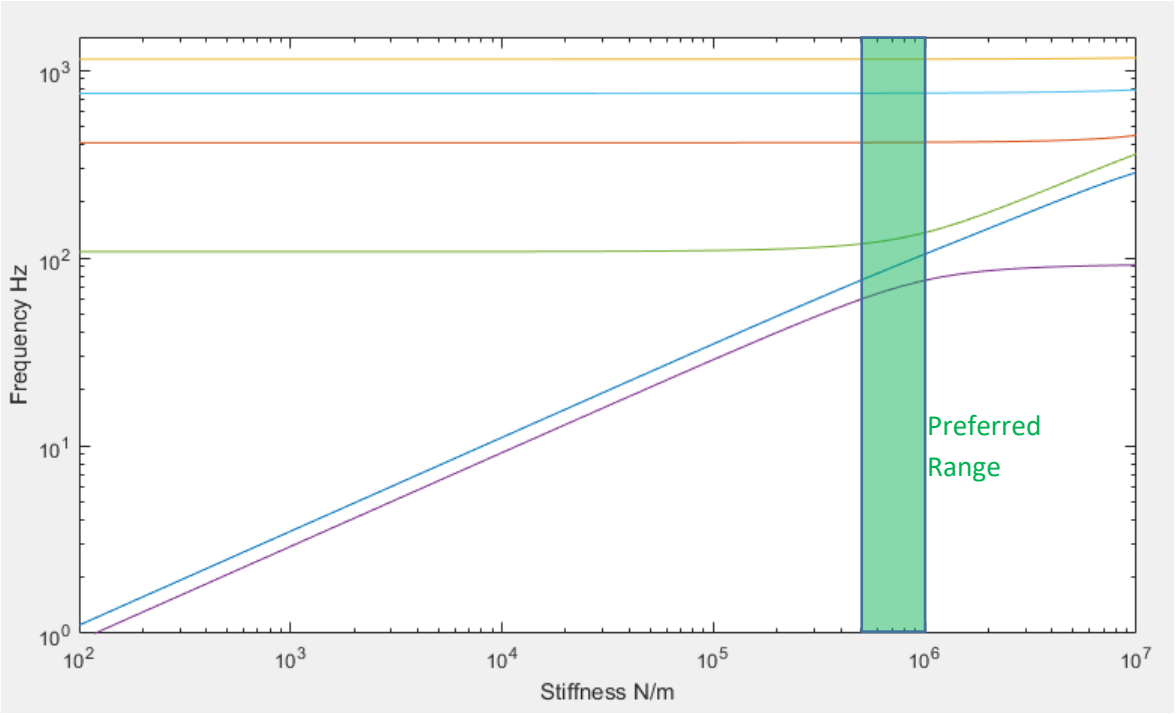

Figure 4-8: Variation of rotor natural frequencies with variation of AMB stiffness.

4.9 Reducing Model DOFs

The state space models presented in equation (4-39) for FEA of the rotor has six inputs and four outputs. The inputs to the state space models are AMB forces and unbalance forces each of which has two components in each plane (V13, W13, V24, and W24 for AMB actuators) and horizontal and vertical components of unbalanced force at the disk node. The unbalanced force components are optional for creating the operational model. It could be used for simulation of unbalanced forces at the disk nodes. The input forces are in Newtons (N). The outputs of the state space model are the four displacement outputs at position sensor locations for V13, W13, V24 and W24 axes. The output unit of the model is displacement in metres (m). Each state space model has 616 states. Integrating a 4x6x616-state model with a controller block makes the integrated model very slow and computationally expensive. The high frequency poles and zeros which are far left side of half complex plane (from the vertical axis) have negligible contribution to the stability and response of the system; hence, these are removed. Furthermore, the actuator dynamics, power amplifier frequency range, signal processing sampling rate of the sensors and the controller bandwidth remove the effect of high frequency poles and zeros. Therefore, the model was reduced for the modes with frequencies lower than 5 kHz. The model was reduced using the MATLAB *freqsep* command which is available in Control System Toolbox

with the low pass cut off frequency of 5 kHz. All the poles and zeros above the low pass cut off frequency were removed from the original state space model. The original state space model was reduced to 4x6x36 after model reduction. The Bode plot for the transfer function of V13 axis with the actuator force as input and V13 sensor axis as the output for the original model and the reduced model are compared in Figure 4-9. Note the good coincidence between the model before and after the reduction up to 5 kHz.

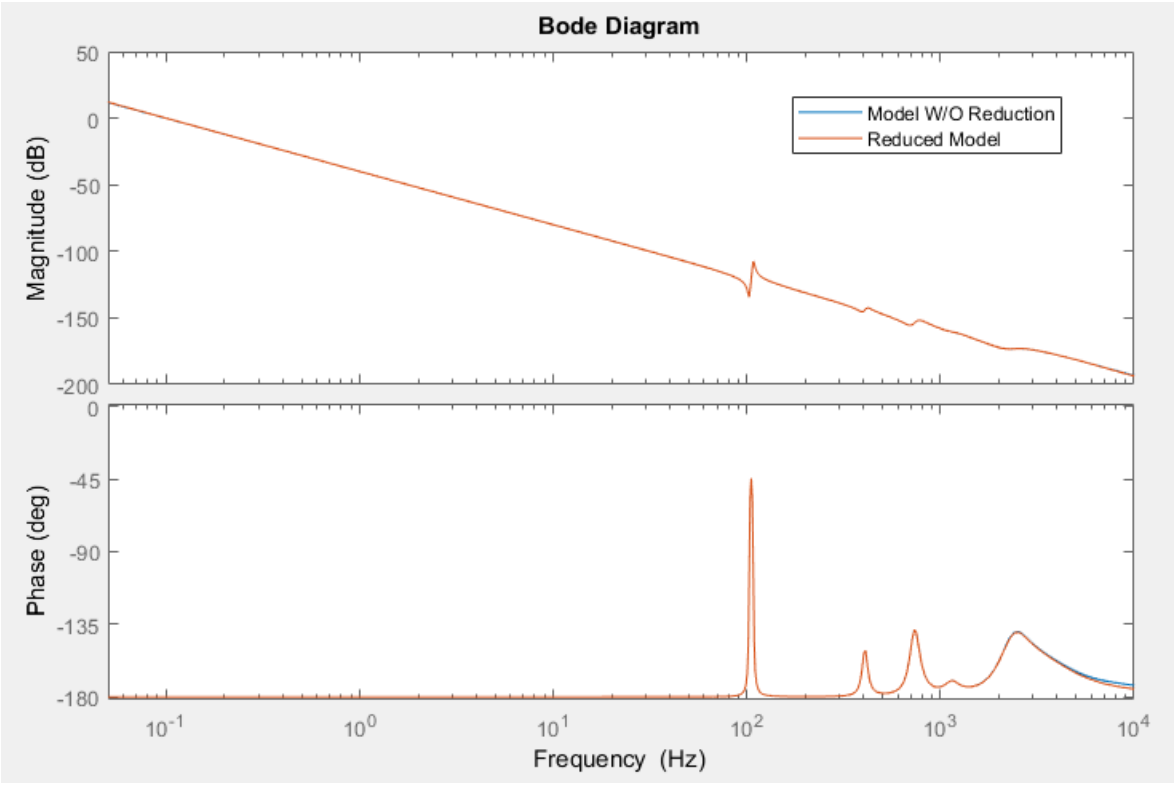

Figure 4-9: Bode plot showing the V13 axis transfer function (actuator (N) to sensor reading (m)) for model without reduction and the reduced model. (0 dB=1 m/N)

Figure 4-10 shows the poles of the free-free rotor system after model reduction. The poles at zero are related to the rigid body mode and other poles are related to the rotor bending modes.

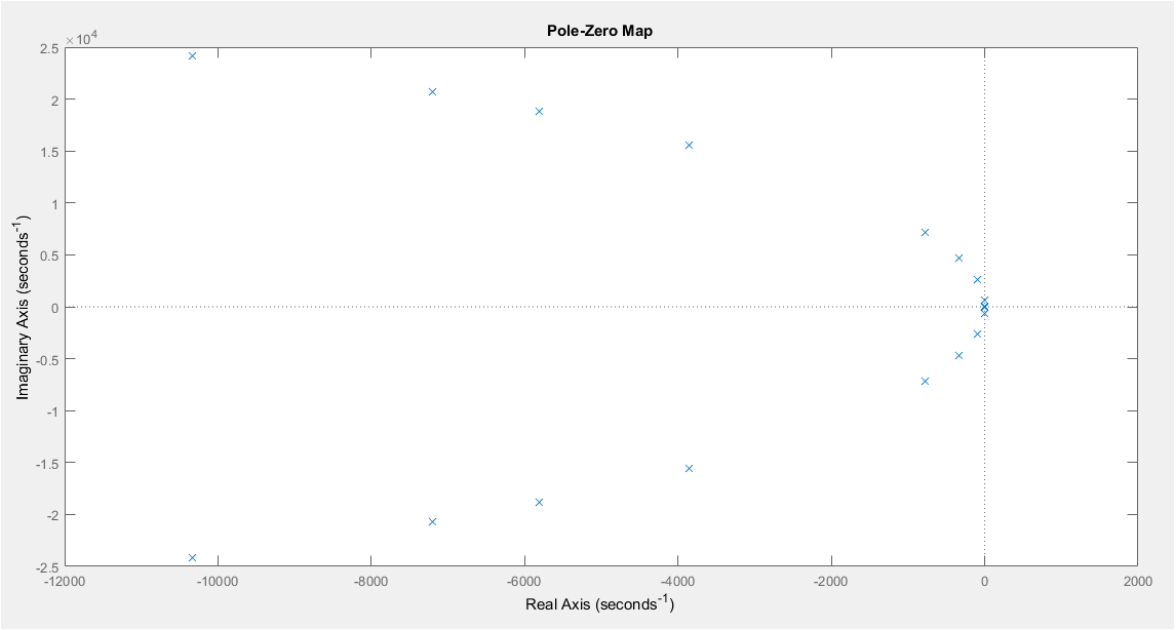

Figure 4-10: Poles of reduced models (both V and W planes)

4.10 Critique

In this chapter, a few assumptions were made during the modelling of MBRotor-II. The FEA model uses two dimension elements (2D FEA); although, the model follows normal industrial standards and guideline. This might lead to some inaccuracies in large elements. For example, the rotor disk which is a part of the rotor has been considered as single elements with large diameter. The elements in this area might not consider the full deflection of the disk. In addition, the FEA model does not include the coupling and the electric motor in modelling. Having an extremely flexible coupling, the rotor can move axially approximately 1 cm. Therefore, the location of the sensors and actuators considered in theory might be deviating from the experiments.

4.11 Summary

In this chapter, the rotordynamic equations of motion for a simple rotor were explained. The FEA model of the SKF MBRotor-II was created based on industry guidelines and rotor data provided by the vendor. Different components such as the laminated plates and disk and their effects on the rotor FEA were considered in the model. Mass, stiffness, gyroscopic and damping matrices were extracted from the FEA model and applied to the rotordynamic

equations of motion. The eigenvalues of the FEA model for the free-free rotor were compared to manufacturer-provided datasheets. The results showed good correlation and the model was deemed to be suitable for the next modelling steps.

The second order differential rotordynamic equations of motion were converted to a set of first order state space equations which had 616 states. The state space model considered sensors reading shaft positions in two locations (both V and W directions) which creates four outputs for the model. The state space model has six inputs which include AMB forces exerted in two shaft location (both V and W directions) and unbalance mass exerted at one location (both V and W directions) at the disk node.

The desirable stiffness of the AMB bearings were extracted based on the natural frequency map against different AMB bearing stiffness values. This desired value will be used in defining the AMB and controller parameters in the next chapter.

The original state space model was reduced to 36 states in the range of 0-5 kHz considering the operating frequency of the rotor and controller system components and sampling rates which will be discussed in more detail in the next chapter. The original model and the reduced model were compared for the coincidence of the transfer functions and suitability.

Chapter 5

Controller Development and Integration with the Rotordynamic Model

5.1 Introduction

In the previous chapter, the free-free FEA rotordynamic model of the rotorkit was extracted and converted to the state space model. This rotor model now requires integration with the AMB and closed loop controller to be supported and levitated radially in the bearings. In this chapter, the characteristics of the AMB and the controller, including PIDs, different filters and other hardware components such as sensors and their transfer functions, are explained. The AMB, controller and other hardware component transfer functions are integrated with the state space model of the rotor. The open loop and sensitivity transfer functions are studied and compared against the standards. Finally, the electrical and total stiffness of the AMB are extracted. Note that the axial movement of the rotor is constrained through the physical coupling to the motor and therefore does not need to be included in this model.

The transfer functions of different hardware components and software settings are extracted in the following sections.

5.2 Magnetic Bearing Transfer Function

In a simple form, the force exerted by a single pole assuming no loss in the iron is provided in equation (5-1) (Schweitzer, 2009):

$$f = \frac{1}{4} k \frac{i^2}{g^2} \tag{5-1}$$

$$k = 4\,\pi\,10^{-7} N_c^2 A_\alpha cos(\alpha_p) \tag{5-2}$$

f : exerted force on the rotor by the single pole (N)

k : magnetic bearing coefficient (Vsm/A)

i : current passing through the coil (A)

g: nominal gap between rotor and the pole (m)

N_c: number of turns of coil per pole (138 turns for MBRotor-II)

A_α : projected area of the pole face on the rotor (m^2)

α_p: angle between poles

Based on equation (5-1) the force acting on the pole is not linear with current which makes the 'plant' non-linear. In order to linearize the equation and thereby simplify the control of the magnetic force, a bias current i_b is introduced at a nominal air gap g_0 which is normally the centre of bearing.

In differential operation mode, control current is added to the bias current in one quadrant and subtracted in the opposite quadrant. The SKF MBRotor-II is comprised of two AMBs that operate in differential mode. The force acting on the rotor in each axis can be modelled as follows (Traxler & Maslen, 2009):

$$f(x, i_c) = \frac{1}{4} k \left(\frac{(i_b + i_c)^2}{(g_0 - x)^2} - \frac{(i_b - i_c)^2}{(g_0 + x)^2} \right) \tag{5-3}$$

$f(x, i_c)$: exerted force on the rotor in each axis on a differential operation mode AMB (N)

i_b: bias current (A)

i_c : control current (A)

g_0: nominal gap between rotor and bearing when the rotor is in the centre of the bearing (m) (364µm in MBRotor-II)

x : the movement of the rotor from centre toward the first electromagnet (m) refer to Figure 5-1.

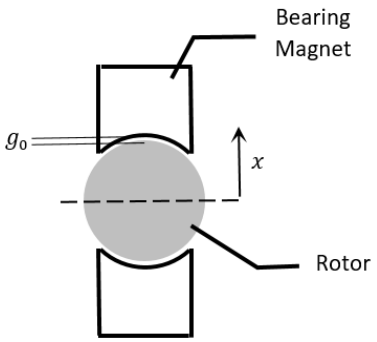

Figure 5-1: Movement of rotor from the centre toward the pole.

The force current factor k_i and force displacement factor k_s (also known as negative stiffness) can be defined as follows, considering $x \ll g_0$ and simplifying the equations (Traxler & Maslen, 2009):

$$k_i = k\frac{i_b}{g_0^2} \tag{5-4}$$

$$k_s = k\frac{i_b^2}{g_0^3} \tag{5-5}$$

k_i with the unit of (A/m) and k_s with the unit of (N/m) play an important role in the control of magnetic bearings. The only parameter that can be modified to change the behaviour of magnetic bearing in the MBRotor-II is i_b. To achieve maximum dynamic range, this value is normally half of the magnetic saturation current. The rest of the parameters are particular to the vendor design and manufacture. However, in the front end engineering design of magnetic bearings different parameters such as rotor weight, maximum process loads on the rotor, rotor tolerances between magnetic bearing and casing are considered in order to define other parameters of the magnetic bearing which mainly defines the load capacity of the bearing.

5.3 Power Amplifier

The power amplifier transfer function is a first order low pass and provided by SKF as follow:

Confidential vendor-supplied data removed from this publically accessible electronic copy.

A reader seeking that data should contact SKF directly. (5-6)

PA_{tf} *: the power amplifier transfer function which its input is control signal voltage and its output magnet current (A/V)*

f *: the low pass band passband frequency which is 1500 Hz*

s *: the complex variable in state space*

The power amplifier acts like a first order low pass frequency with a passband frequency of 1500 Hz. Figure 5-2 shows the frequency response of the magnetic bearing.

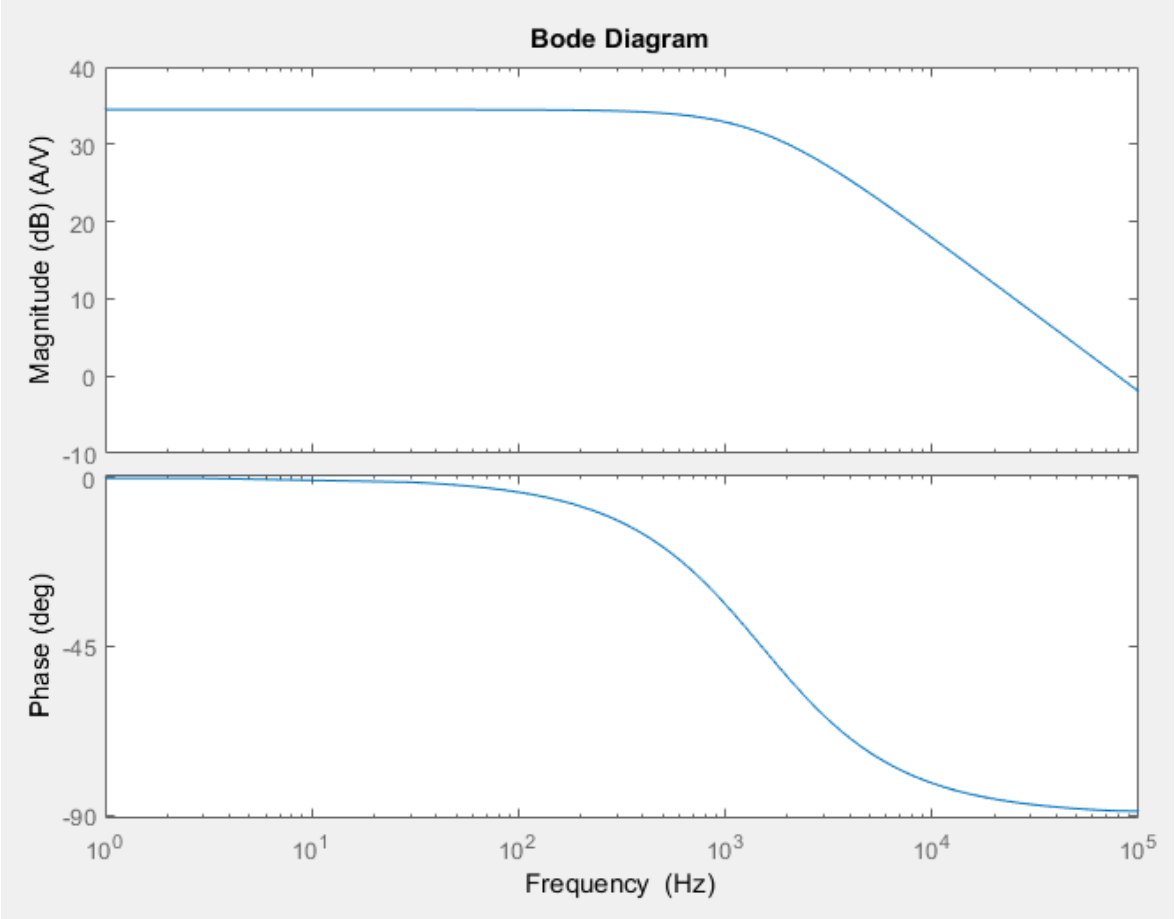

Figure 5-2: Bode plot of power amplifier.

5.4 Displacement Sensor Transfer Function

The displacement sensor is comprised of three transfer functions; sensor, anti-aliasing filter and a low pass filter. These transfer functions are characteristics of hardware components and is provided by vendor. The sensor transfer function measures the input displacement in metres (m) from the FEA state-space model and the output of the transfer function is the measured in volts (V). The transfer function of each of these components is provided below:

Confidential vendor-supplied data removed from this publically accessible electronic copy.

A reader seeking that data should contact SKF directly.

(5-7)

k_{sens}*: the scale factor of the sensor. The scale factor is the inverse of sensitivity of the sensor provided by the calibration tool which has been described in section 3.3.3.*

f *: the sensor which acts like a low pass filter with a passband frequency of 3000 Hz.*

ζ_s : damping ratio of the sensor low pass filter.

The scale factor for each displacement sensor on each axis can be extracted from the sensitivity provided in the calibration tool. The calibration tool defines the scale factor of the sensor based on the predefined movement of the rotor within the auxiliary bearing (*refer to section 3.3.3).* The scale factor of the sensor is the inverse of sensitivity of the sensor. A screen shot of calibration tool is shown in Figure 5-3. The scale factor of the sensors for each axis is provided in Table 5-1.

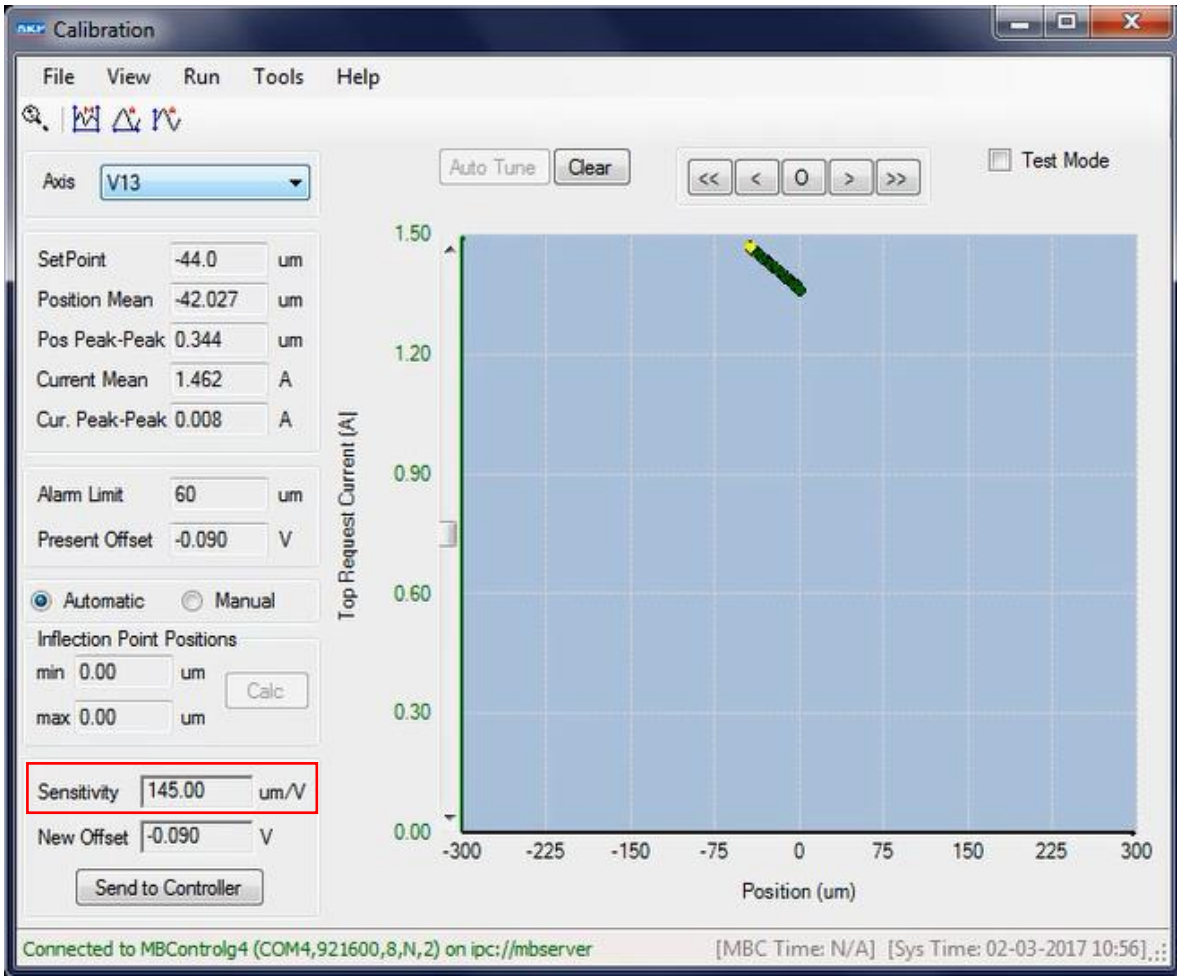

Figure 5-3: Calibration tool providing the sensitivity of the displacement sensor for V13 axis.

Table 5-1: Scale factor of displacement sensors for each axis

Axis	Displacement Sensor Scale Factor (V/m)
V13	6896
W13	8929
V24	7246
W24	8333

The sensor has an anti-aliasing filter which is of first order with a corner frequency of 15.9 kHz. This filter remove the noise or undesired signal measurement which has a higher frequency than the specified value. The transfer function of anti-aliasing filter is as follows:

Confidential vendor-supplied data removed from this publically accessible electronic copy.
A reader seeking that data should contact SKF directly. (5-8)

f *: the anti-aliasing filter frequency (15.9 kHz)*

The anti-aliasing filter prevents the aliasing components from being sampled. This is implemented by attenuating the higher frequency components of a raw signal. Note that there are some other components, such as power amplifier, which also reduce the effect of higher frequency components (>1500 Hz).

The sensor also has a 2nd order low pass filter with a passband frequency of 10 kHz. The transfer function for the filter is provided as below:

Confidential vendor-supplied data removed from this publically accessible electronic copy.
A reader seeking that data should contact SKF directly. (5-9)

f *: sensor Low pass passband frequency (10 kHz)*

ζ_{LP} *: damping ratio*

The Bode plot of V13 axis sensor, anti-aliasing and low pass filter in series transfer function is plotted in Figure 5-4.

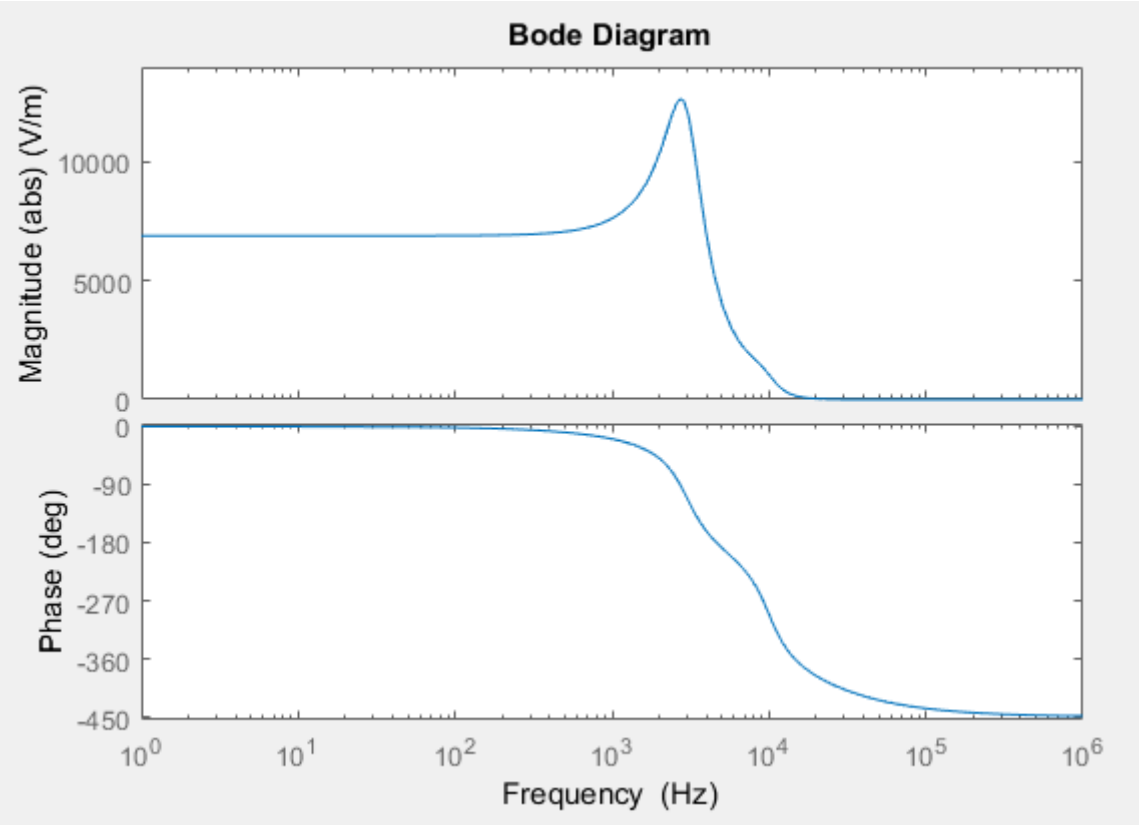

Figure 5-4: Bode plot of V13 displacement sensor transfer function for parameters listed in Appendix 2.

5.5 Controller Time Delay Transfer Function

The controller has a delay in processing the input signal and providing output to the actuator. SKF has provided a time delay of 50µs whose transfer function may be presented as follows (based on author's communication with SKF):

Confidential vendor-supplied data removed from this publically accessible electronic copy.

A reader seeking that data should contact SKF directly.

(5-10)

T_c *: the controller time delay of 50 µs*

5.6 Zero Order Hold Transfer Function

Zero Order Hold (ZOH) is a type of digital to analogue conversion function that converts the discrete time input from the controller to the continuous time output. The transfer function provided by SKF for the ZOH in MB340g4-ERX is defined as below:

Confidential vendor-supplied data removed from this publically accessible electronic copy.

A reader seeking that data should contact SKF directly.

(5-11)

T_d : sampling interval of ZOH which is 100 µs in MB340g4-ERX

The Bode plot of the ZOH_{tf} is shown in Figure 5-5.

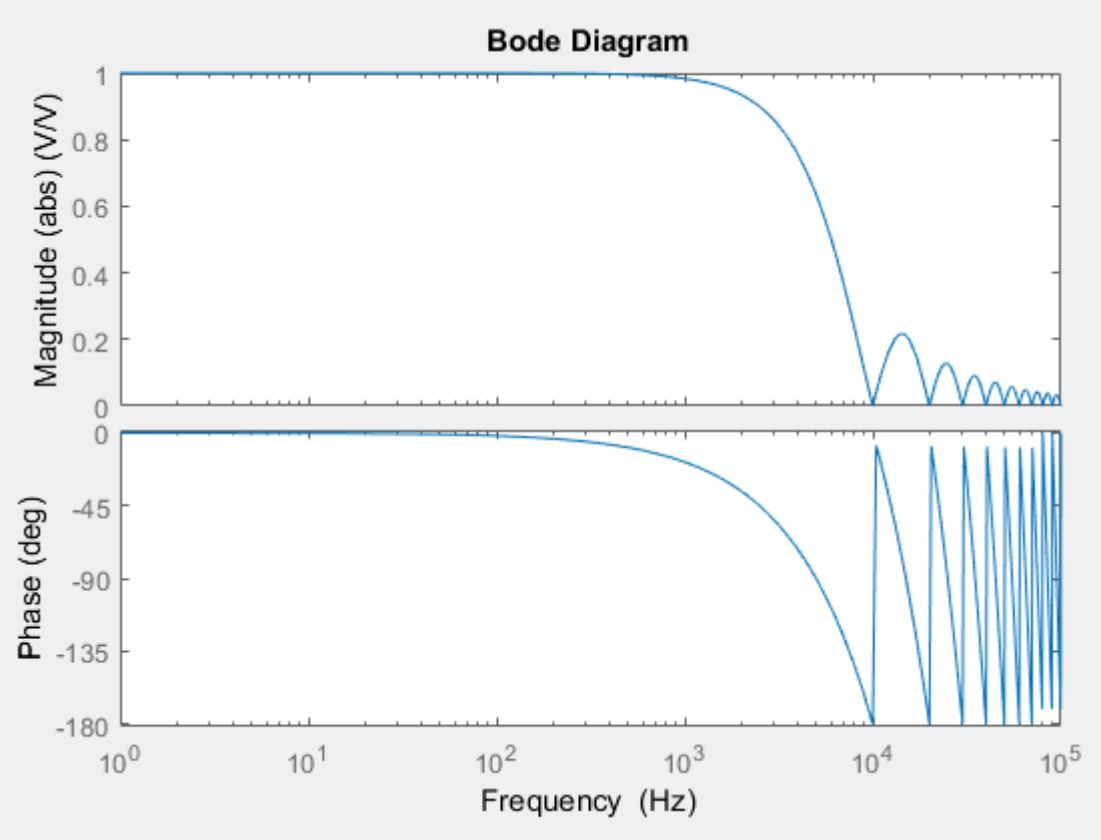

Figure 5-5: Zero Order Hold Transfer function (ZOH_{tf}) of MB340g4-ERX

The above sampling delays (ZOH and TD) could be approximated by Pade approximation methods. Pade functions approximate time delays of rational functions in s. Experience indicates that a third order Pade approximation is enough for most of applications (Maslen & Schweitzer, 2009). The above mentioned time delays were approximated by a third order Pade function in MATLAB for simulation of this system which is demonstrated in Figure 5-6.

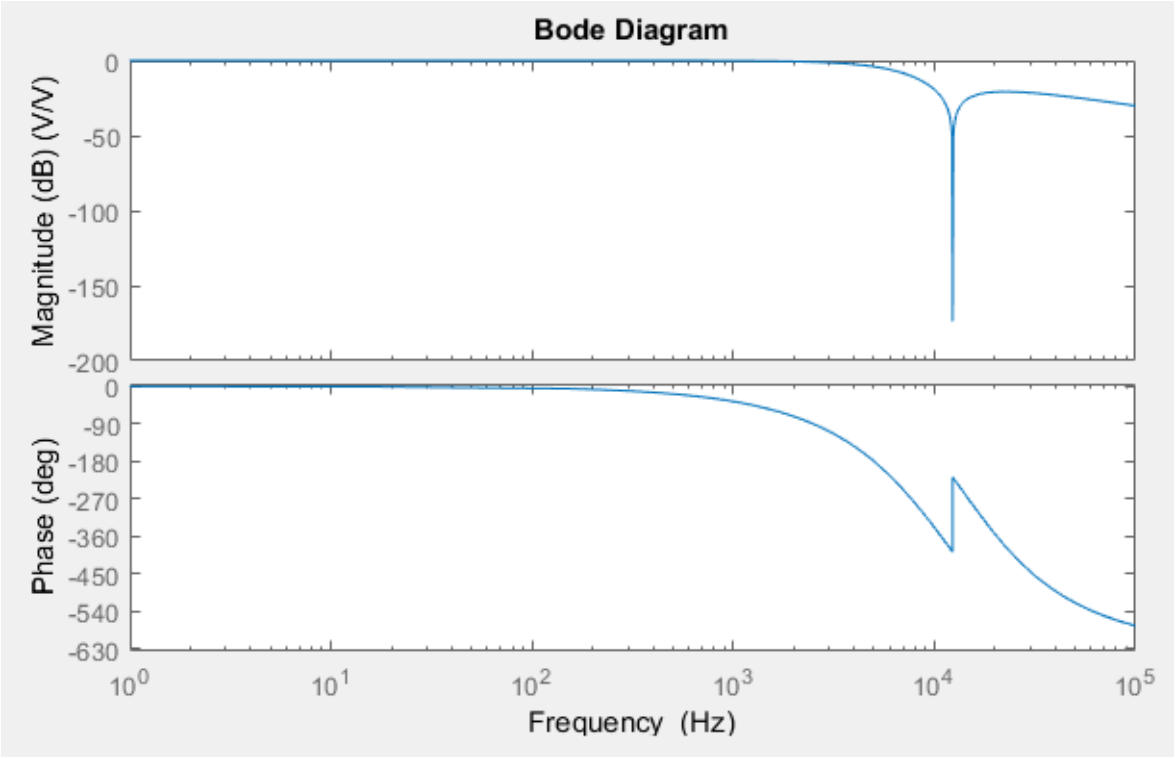

Figure 5-6: MATLAB Pade simulation of time delays in the controller.

5.7 Digital Controller Transfer functions

In diagnostics of AMB-supported rotors, normally, the hardware transfer function cannot be modified to change the behaviour of the rotor system. However, the transfer function of the digital controller can be modified. In the SKF MBRotor II equipped with the MB340g4-ERX controller, the digital controller parameters may be modified through the MBScope - Configuration Panel software which was demonstrated in Figure 3-4. This controller is a Single Input Single Output (SISO) controller. In this case, the position sensor reads the position of the rotor in that axis direction and sends the data to the associated axis controller. The digital controller processes the input and sends a command signal to the same axis without having any communication with the other axes of the digital controller. The control diagram of the MB340g4-ERX is shown in the MBRotorII control schematic in Figure 5-8.

The digital controller has several filters and transfer functions in addition to having the capability of controlling the bias current. Different filters and their functions are explained in the following sections.

5.7.1 PID controller and total gain

Each axis has a Proportional, Integral, and Derivative (PID) control algorithm. PID controllers are widely used in industrial control systems including the AMB controls. The PID calculates the error between the position set-point and the measured position from the position sensor and provides a control command output. Normally the set-point value is zero in magnetic bearings which is equal to the centre point of the AMB, which is the rotor's desired location.

The P value is a gain factor which multiplies the error value by the gain (P). It is similar to the effect of a spring. The integrator part of the PID, removes the residual error that necessarily exists for the P mode. In other words, the integrator removes the steady state error. The Derivative component provides output based on the current rate of change of the error. The derivative component provides a signal based on the radial velocity (derivative of position) of the rotor. The derivative component performance is similar to damping in fluid film bearing. However, the derivative component causes phase and gain change (+90°) across all frequencies and is not truly physically realisable. Therefore, instead of derivative component other filters such as phase lead or phase lag are used to damp the rotor resonances in the operating speed range of the equipment.

The PID controller also have an overall gain.

The transfer function of and ideal PID and the total gain is as follows:

Confidential vendor-supplied data removed from this publically accessible electronic copy.

A reader seeking that data should contact SKF directly.

(5-12)

PID_{tf} PID transfer function (V/V)

$TotalGain$ *: the overall gain in series with PID.*

P *: proportional gain*

D *: derivative gain (which is not used in the controller or its value is 0)*

I *: integrator gain*

5.7.2 Lead-Lag Filter

The lead-lag filter section in the configuration panel provides the settings for two pairs of zero and poles frequencies. The general transfer function of a phase lead or phase lag filter is as follows. Each axis has the setting for two transfer functions, demonstrated in equation (5-13), in series.

Confidential vendor-supplied data removed from this publically accessible electronic copy.

A reader seeking that data should contact SKF directly.

(5-13)

f_z *: zero frequency of the phase lead/lag transfer function*

f_p *: pole frequency of the phase lead/lag transfer function*

The pole of the transfer function causes the gain of the transfer function to decrease as frequency increases. The zero of the transfer function causes the gain of the transfer function to decrease as the frequency decreases.

In a phase lead filter the zero frequency is lower than the pole frequency. Therefore, the gain and phase increases between the two frequencies. This filter is normally applied for damping the resonances in the operating speed range of the equipment. The filter can damp the resonance by increasing phase lead which is termed phase stabilisation.

In some cases the resonances may not be damped by a phase lead filter. A phase lag filter could be applied which decreases the gain and the phase over the frequencies between the pole and zero of the transfer function. In this case the pole frequency is lower than the zero frequency. As this technique attenuates the gain in the specified frequencies, it is called gain stabilisation.

The phase lead transfer function of V13 is demonstrated in Figure 5-7. As explained above, the gain and phase have increased between specified frequencies.

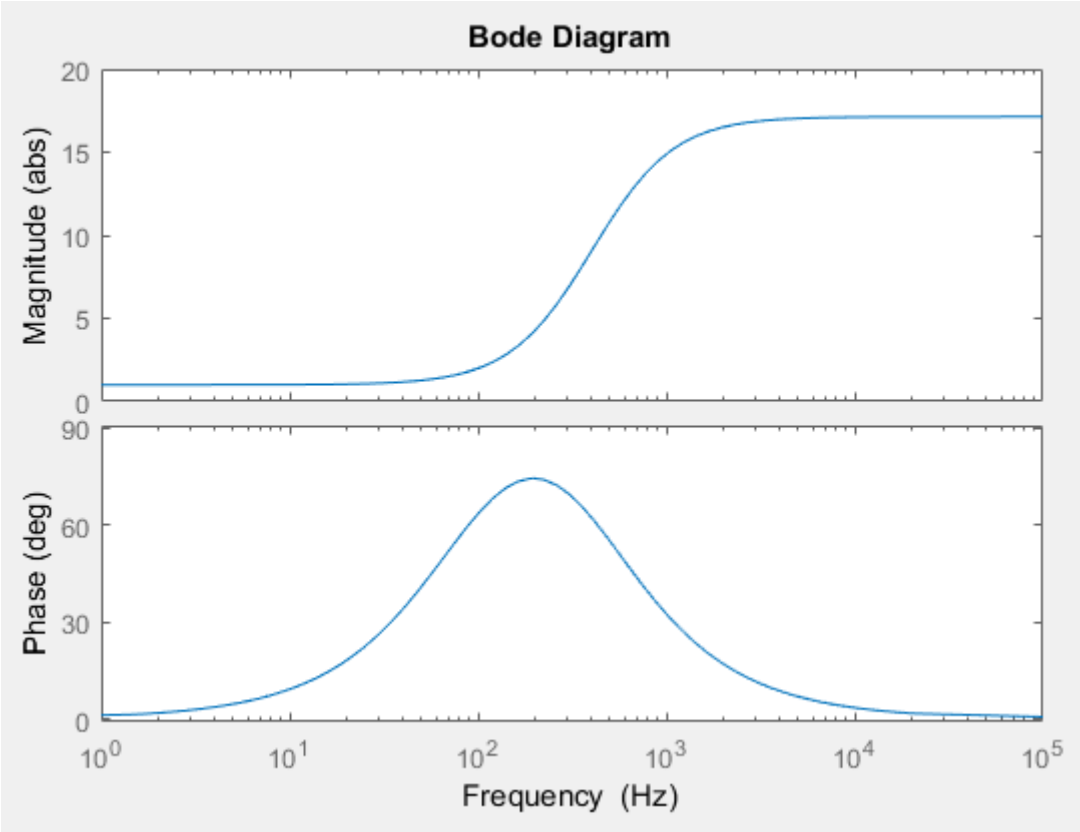

Figure 5-7: Phase Lead transfer function of V13 axis.

5.7.3 Low pass filter

Each axis has available settings for two low pass filters. The low pass filter can be used for removing higher frequencies than the operating speed range and it will make the system run acoustically quieter by attenuating the effect of the high frequency components of the magnetising currents. However, a low pass filter can decrease the phase lead which in turn can lead to a decrease in the damping of frequencies below and above the specified frequency including the system resonances. Although this filter is available, for this reason it has not been applied in the control of the MBRotor-.

5.7.4 Generic Filters

Each axis has four generic filter settings available. These settings are used for reducing the effect of resonances outside the operating speed range of the rotor. The Generic 2nd order filter transfer function is demonstrated as follow:

Confidential vendor-supplied data removed from this publically accessible electronic copy.

A reader seeking that data should contact SKF directly.

(5-14)

H_{tf} *: generic 2nd order filter transfer function*

f_N *: filter frequency of the numerator*

f_D *: filter frequency of the denominator*

ζ_N *: damping ratio of the numerator*

ζ_D *: damping ratio of the denominator*

5.8 Integration of FEA Model and Controller

The FEA state-space rotor reduced model was extracted in the previous chapter. This model needs to be integrated with the hardware and software transfer functions to create a complete rotor system model. The chosen values for the rotor hardware components, PID controller gains and digital filter settings are provided in Appendix 2.

The rotor model provides four outputs at the location of the displacement sensors. These outputs are extracted and pass through the position sensor transfer functions which consists of anti-aliasing, first order low pass filter and the sensor transfer functions which itself acts as a second order low pass filter. The output of each of these sensors goes to the digital controller where the feedback signal is compared with the set point which is the centre of the bearing. The error is multiplied by total gain and goes through the PID module. The PID output goes through multiple filters which are in series (Lead-Lag, 2nd order generic, etc.) and the command signal is sent to the power amplifier and bearing that acts as a low pass filter. The output of controller and bearing is the force that is acting on the specified nodes in the FEA model (which are the bearing locations). The integrated Simulink controller and the rotor model is shown schematically in Figure 5-8.

The MB340g4-ERX controller is a SISO controller for each of the four axes. The output of each position sensor is processed separately and the command signal is sent to the associated bearing quadrants separately.

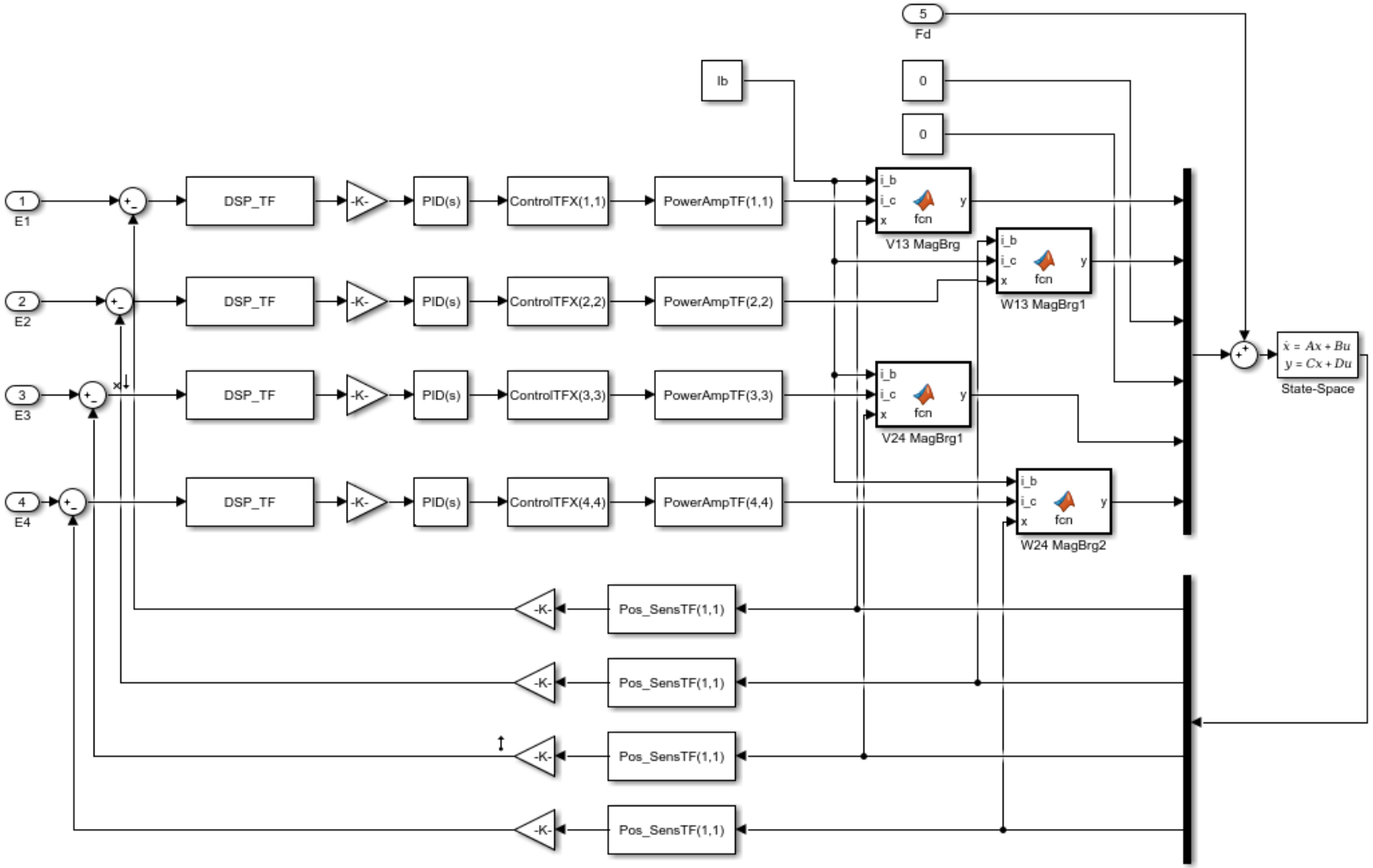

Figure 5-8: MBRotorII Simulink control schematic

5.9 Industry Standards

As AMB systems are becoming more popular in industry, there is a need for standards to define best practices and guidelines for end users and having more coherence between different manufacturers. ISO and API are the most common standards that have provided guidelines on AMB systems. It is necessary to have an understanding of the industry standards for dealing with industrial application and safely operating the equipment.

ISO 14839 has four parts that provide information for users to understand AMB systems and the differences between conventional bearings and AMBs. It also provides guidelines for shaft displacement vibration measurements and their limits. In addition, it provides guideline for evaluation of stability margins of the AMB system giving assurance to the end user that the AMB system meets the minimum design expectation. This standard is applicable to the industrial machines with the nominal power of above 15 kW.

ISO14839-2 (2004) defines the vibration zone limits for equipment with power consumption of above 15 kW and minimum radial clearance of C_{min} as set below:

Zone A: Normally newly commissioned machines have a maximum peak vibration levels lower than 30% of C_{min}.

Zone B: Normally machines accepted for long term operation have a maximum peak vibration levels lower than 40% of C_{min}.

Zone C: Normally machines with maximum peak vibration levels lower than 50% of C_{min} are not considered acceptable for long term operation.

Zone D: Machines running with maximum peak vibration levels higher than 50% of C_{min} is considered to be sufficiently severe to cause damage to the machine.

The above mentioned criteria are used in Chapter 6 for defining acceptable limits of vibration for the MBRotor-II.

ISO14839-3 (2006) defines where the signal should be injected and where the output signals are to be measured for defining the open loop and sensitivity functions. Figure 5-9 demonstrates where the signal should be injected and where the signal should be measured for assessing the stability of the AMB system.

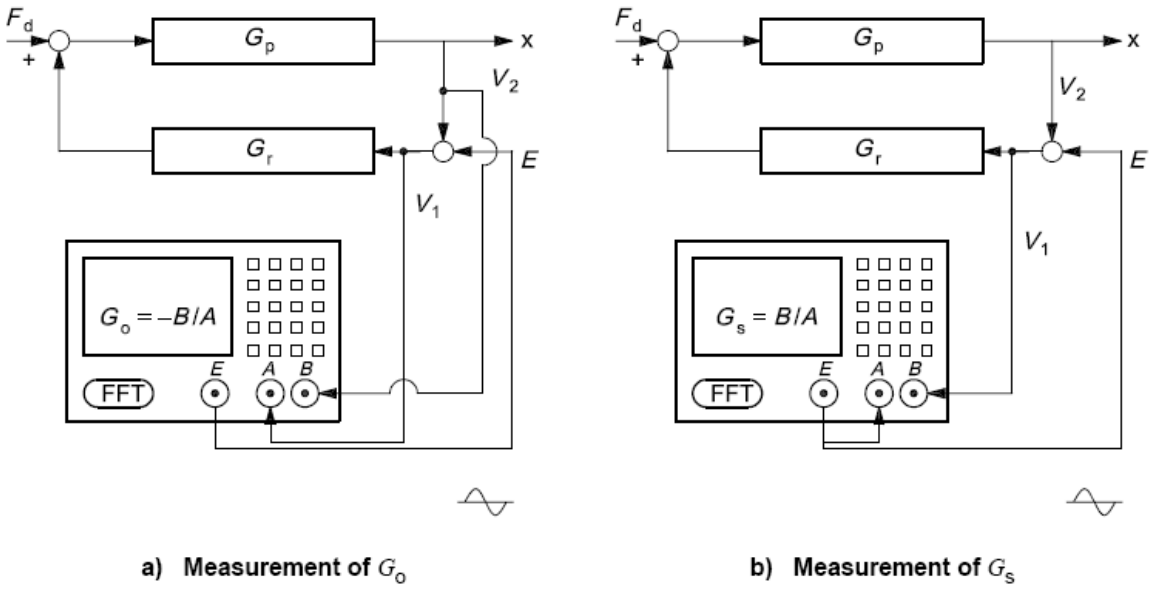

Figure 5-9: Signal injection and measurement for defining open loop and sensitivity transfer functions based on ISO14839-3 (2006).

where:

G_p is the transfer function of the plant

G_r is the transfer function of the AMB control system

E is the external oscillation signal

G_o is the open loop transfer function

G_s is the sensitivity function

ISO14839-3 (2006) defines the stability zone for peak sensitivity by adapting the guidelines of ISO14839-1 (2002). The peak sensitivity is defined in the frequency range of 2 kHz, or three times the rated speed, whichever greater. It should be noted that the maximum frequency should be limited to half of sampling frequency.

- Zone A: Peak sensitivity below 9.5dB (3 abs). The newly commissioned machines normally falls within this limit.
- Zone B: Peak sensitivity between 9.5dB (3 abs) and 12dB (4 abs). These machines are considered normal for long term operation.
- Zone C: Peak sensitivity between 12dB (4 abs) and 14dB (5 abs). These machines are considered unsatisfactory for long term operation.

- Zone D: Peak sensitivity above 14dB (5 abs). The machines with this sensitivity are considered severe to cause damage to machine.

There are two levels of stability defined by API 617. Level I screening criteria defines that all of the modes up to twice normal maximum continuous speed should be considered. For modes above 125% of normal maximum continuous speed, level II analysis should be performed if the minimum log decrement is below zero. For modes between normal maximum continuous speed and 125% of normal maximum continuous speed, a level II analysis should be performed if the log decrement is smaller than the value defined by API 617 which is as below.

$$\delta_{\min\, allowable} = 0.5 - 0.4\frac{N_{mode}}{N_{mc}} \tag{5-15}$$

Where:

N_{mode}: $critical\ speed\ at\ the\ mode$

N_{mc}: $maximum\ continuous\ operating\ speed$

Level II stability requires that for all modes up to maximum continuous operating speed the final log decrement should be greater than 0.1 and for all modes greater than 125% of maximum continuous operating speed, the log decrement should be greater than zero. For any modes between N_{mc} and 125% of N_{mc}, the log decrement should be greater than $\delta_{\min\, allowable}$ which is defined above.

API 617 Annex E (2014) specifies level I or level II stability analyses where Level I stability analysis shall be done on all AMB supported compressors. Both level I and level II stability analyses consider cross-coupling on stability analysis.

API 617 in several sections incorporates ISO14839 criteria and has a united approach rather than defining redundant criteria to ISO14839. As a part of its guidelines, API 617 recommends that the ISO14839-3 sensitivity transfer function should be implemented as a part of both level I and level II analyses.

5.10 Closed Loop, Open Loop and Sensitivity Transfer Functions

In this section the open loop transfer function of the controller system from the MBRotor data acquisition system will be compared with the open loop transfer function extracted

from the model based on the ISO standard. For this purpose, a sweep signal was injected at certain point in the rotor controller system and the output signal measured at the defined point. This was to validate the model and the functionality of the rotor system and it also provided the capability of optimising the controller parameters before implementing the parameters on the MB340g4-ERX.

ISO 14839-3 (2006) defines the points where the oscillator signals should be injected to the system and where the output signal should be measured to extract the closed loop transfer function of the system. The rotor must be levitated while the exciting signal is injected in the system and the output is measured.

Figure 5-9 defines the points where the signal should be injected and measured. The open loop transfer function is defined as follows:

$$G_0 = -\frac{V_2}{V_1} \tag{5-16}$$

V_2 the output measured signal

V_1 the input measured signal (injected)

The closed loop and sensitivity transfer functions could be extracted as follows:

$$G_c = \frac{G_o}{1 + G_o} \tag{5-17}$$

$$G_s = \frac{1}{1 + G_o} \tag{5-18}$$

G_c Closed loop transfer function

G_s Sensitivity transfer function

The open loop transfer function may be used to compare the theoretical model with the signals measured from the rotorkit. The sensitivity transfer function indicates the stability of the system and comparison with the evaluation criteria defined by ISO 14839-3.

The SKF MBScope Analyser module provides the capability of injecting the signal through the software and extracting the system output. This software module is capable of providing Open Loop and Sensitivity plots after injecting signal to different control axes of

the rotorkit. The strength (amplitude) of injected signals may be adjusted for different frequency ranges in order to avoid instability of the system as a result of high levels of excitation signal, especially at system natural frequencies. In case of high level excitation signals, high level vibration will cause the protection system to activate and drop the rotor from levitation.

A screenshot of the SKF MBScope Analyser tool is provided in Figure 5-10. Based on the information provided by the SKF engineering team the software open loop measurement is questionable for frequencies above 400 Hz. A control system should attenuate the signals for higher frequencies and natural frequencies. As it is shown in the open loop plot of the controller in Figure 5-10, the open loop controller amplifies the signal for frequencies above 400 Hz. This is in contradiction with the function of the actual control system. Therefore, the measured data above 400 Hz is not trusted.

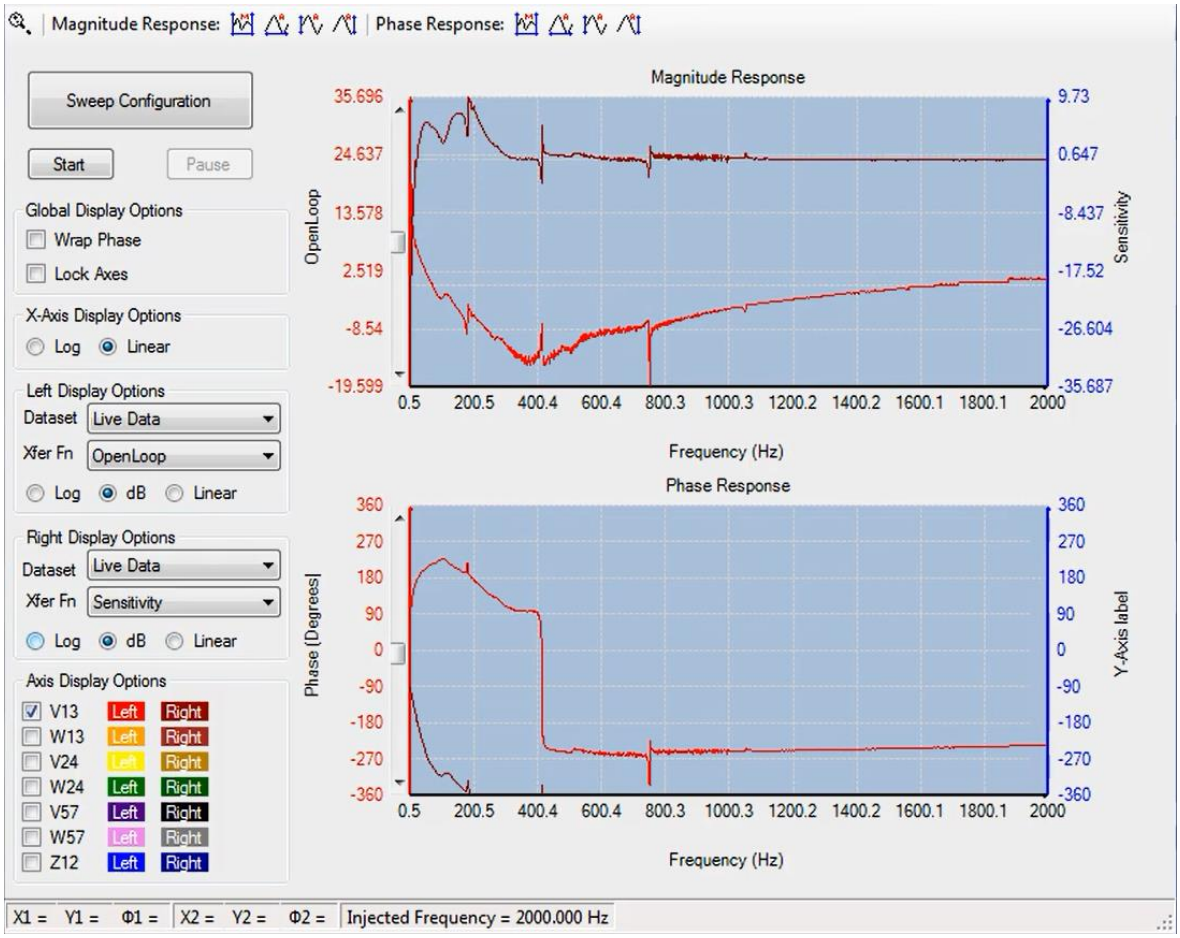

Figure 5-10: SKF MBScope Analyser demonstrating Open Loop and Sensitivity measured for V13 axis.

5.11 Comparison of Theoretical Model and Experimental Data

The open loop transfer function of the model created in Simulink was extracted. The input and output points for extracting the open loop transfer function were chosen based on the ISO 14839-3 definition. Figure 5-11 indicates the input and output points for extracting the open loop transfer function from the Simulink model.

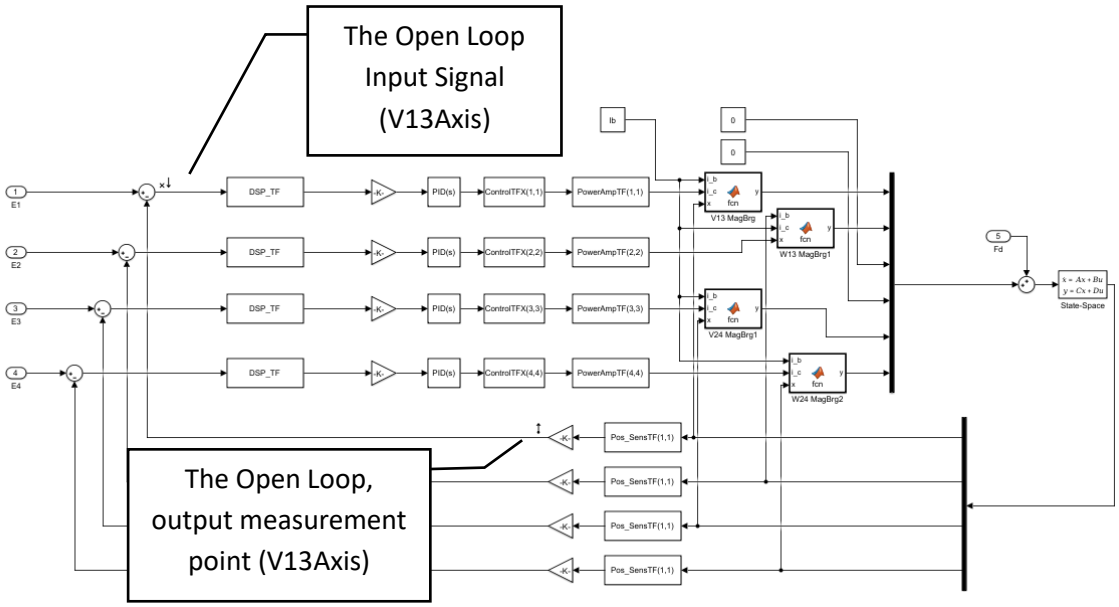

Figure 5-11: Simulink diagram showing the input and output point for measurement of the open loop transfer function of V13 axis.

The open loop transfer function plot is compared with the measured transfer function through the SKF MBScope Analyzer. Figure 5-12 and Figure 5-13 respectively plot the V13 and V24 open loop transfer function plots from the Simulink model (red) and Measurement data (blue) from the MBScope Analyzer. The plots show acceptable coincidence for frequencies up to 300 Hz. As the Simulink model transfer functions show, the open loop transfer function should attenuate the signal as the frequency increases. Below 300 Hz, there are minor differences between the model and the measured data that might be related to measured data errors or factors that have not been considered in the model, such as coupling with the motor or the support stiffness.

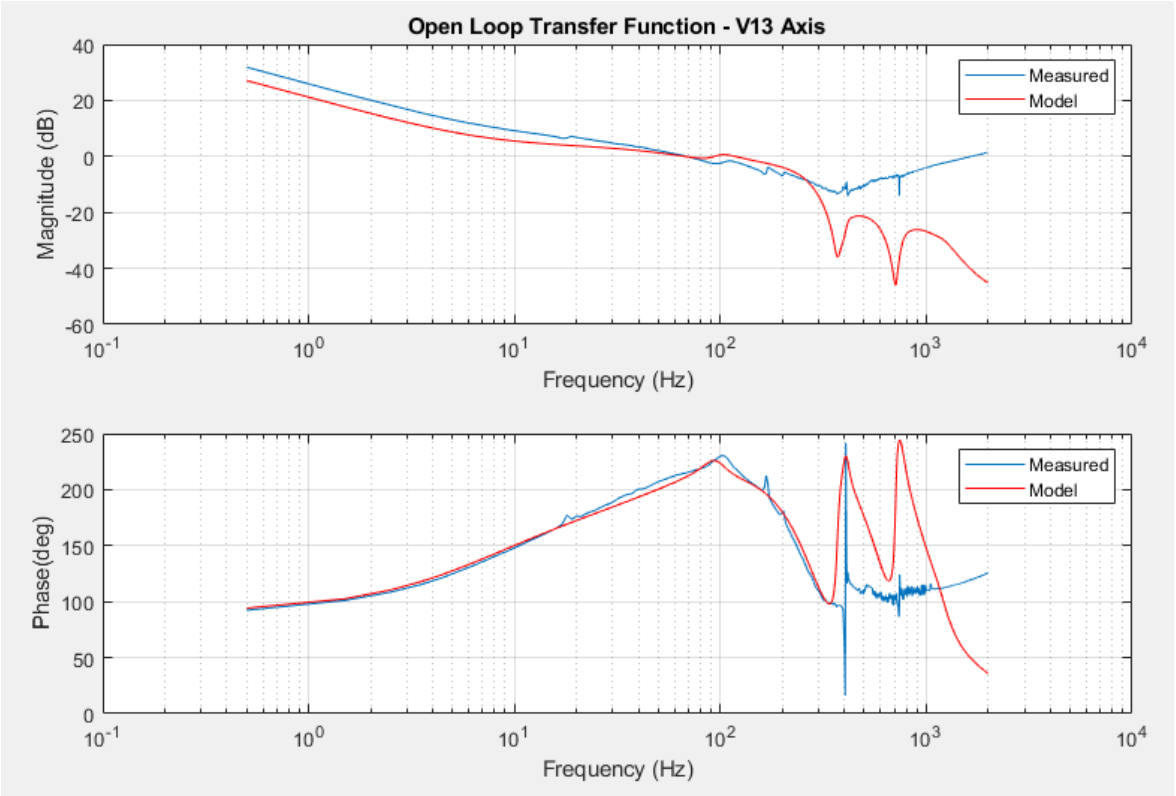

Figure 5-12: Open Loop Transfer Function comparison between Simulink Model and Measured Data – V13 Axis

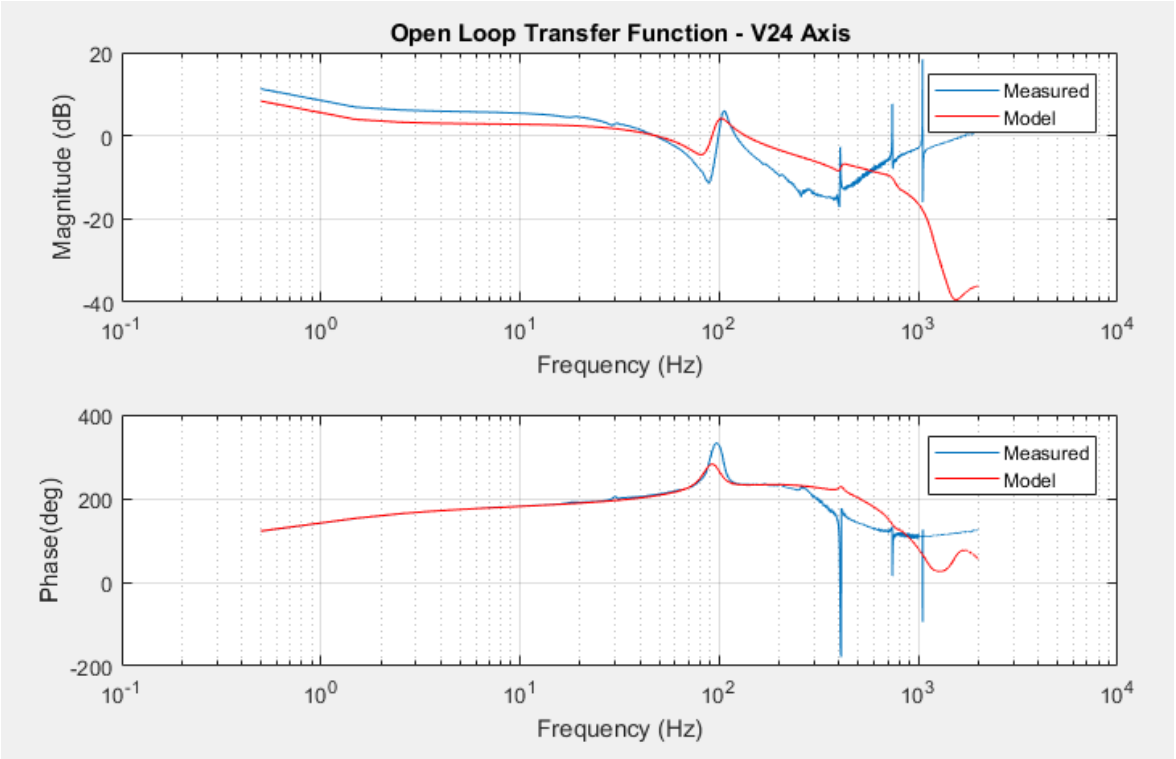

Figure 5-13: Open Loop Transfer Function comparison between Simulink Model and Measured Data – V24 Axis

The measured and modelled sensitivity transfer function plots for both V13 and V24 axis are shown in Figure 5-14 and Figure 5-15. Based on the criteria defined by ISO 14839-3 (Refer to section 5.10), the measured magnitude for both axes are below 3. ISO 14839-3 defines sensitivity of newly commissioned machines to be falling in this zone (Zone A) as described in section 5.10.

There are differences between the modelled and measured results. This might be related to many factors that were simplified in the model such as: small differences in the location of AMB and sensor (the nodes) in the model and their real location on the MBRotor causing large differences between the model and measurement (ISO14839-3, 2006); the rotor was modelled decoupled from the motor; measurement errors in injecting signals and measurement of the response (output); the rotor composition and material that was considered to be without any loss (no eddy current or loss); the support stiffness was assumed to be rigid in the model; some manufacturing simplification such as misalignment between the AMBs and the exact location of rotor within the AMBs are considered minimal.

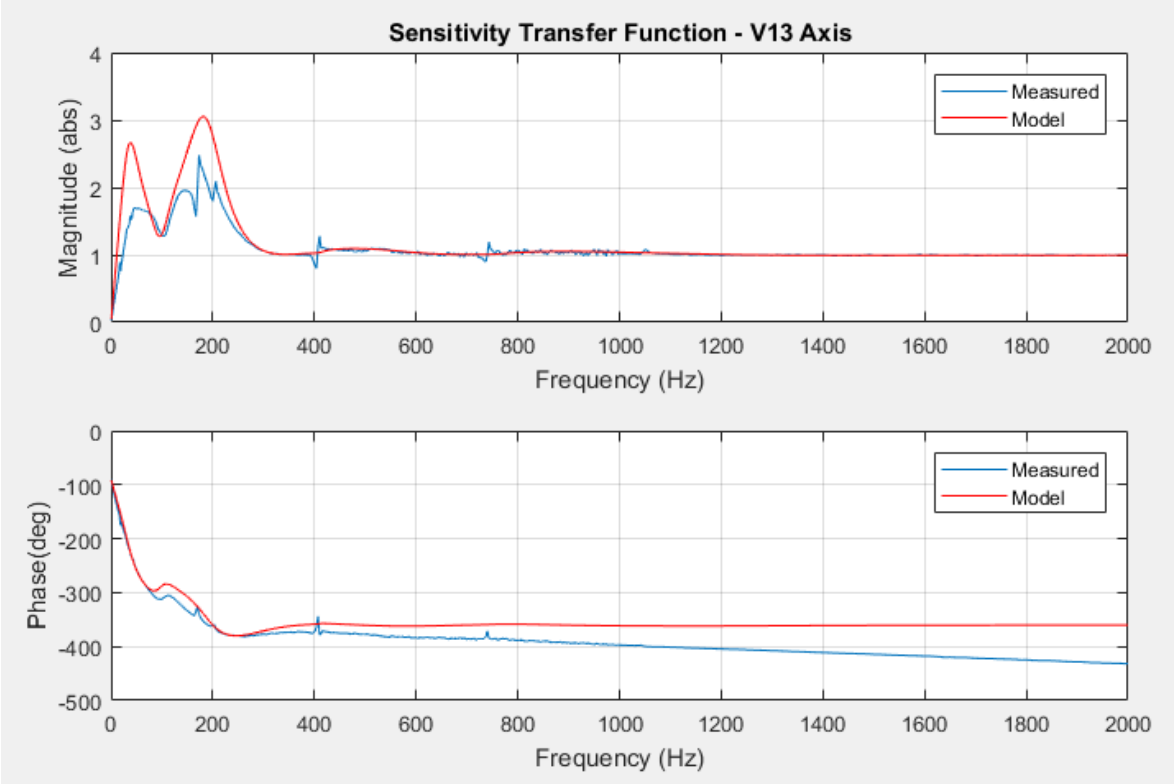

Figure 5-14: Sensitivity transfer function plot for V13 axis

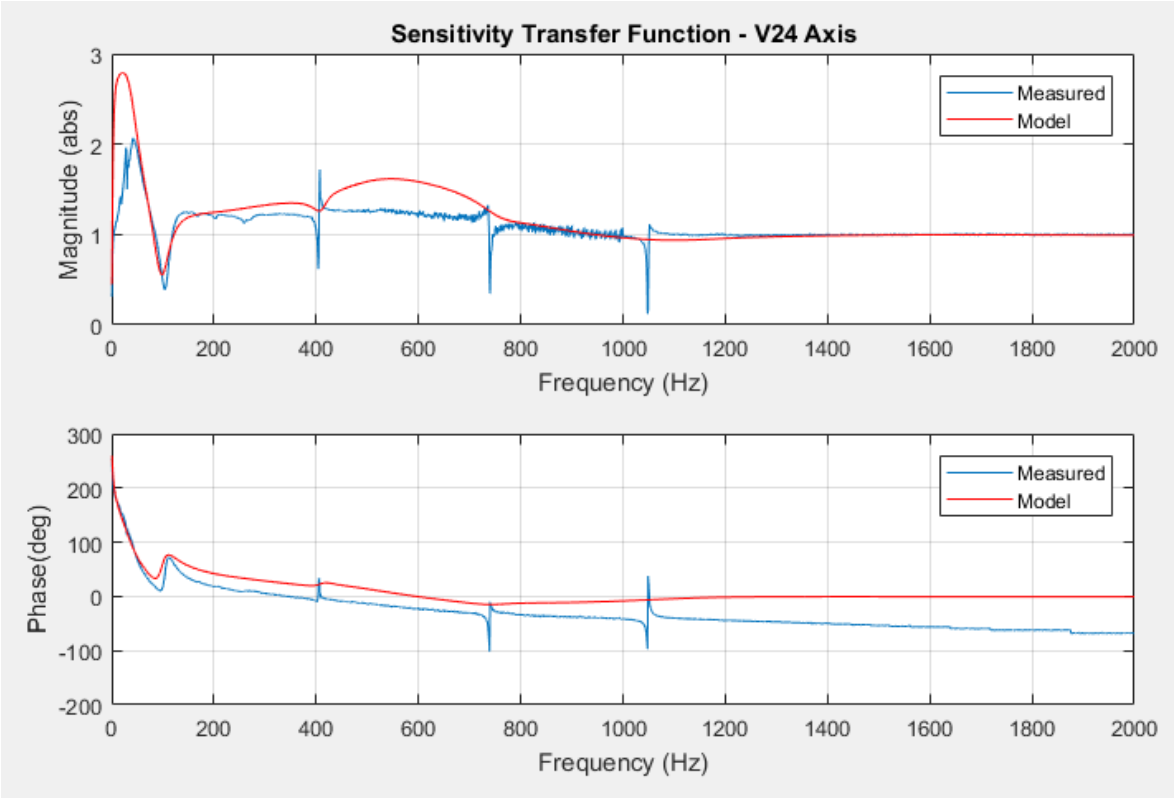

Figure 5-15: Sensitivity transfer function plot for V24 axis

5.12 AMB stiffness

The bearing stiffness and the control circuit are frequency dependent. The AMB output force divided by the displacement reading of the sensors for different frequencies provides the AMB system stiffness. This may be extracted from MATLAB-Simulink model. The points of signal injection and output measurement are shown in Figure 5-16. Figure 5-17 shows the Bode plot of the AMB stiffness transfer function extracted from the Simulink model. The model stiffness is in line with the desired stiffness (0.5-1 MN/m) extracted from the FEA model in section 4.8 for the operating speed of the MBRotor-II.

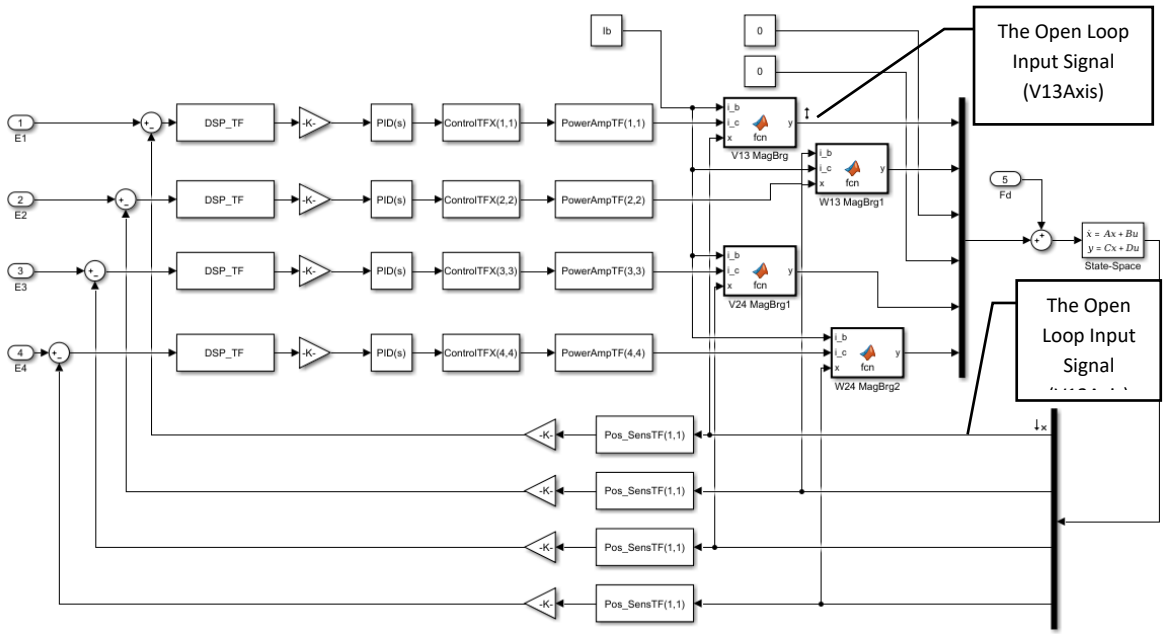

Figure 5-16: Simulink model and measurement and signal injection points for equivalent stiffness.

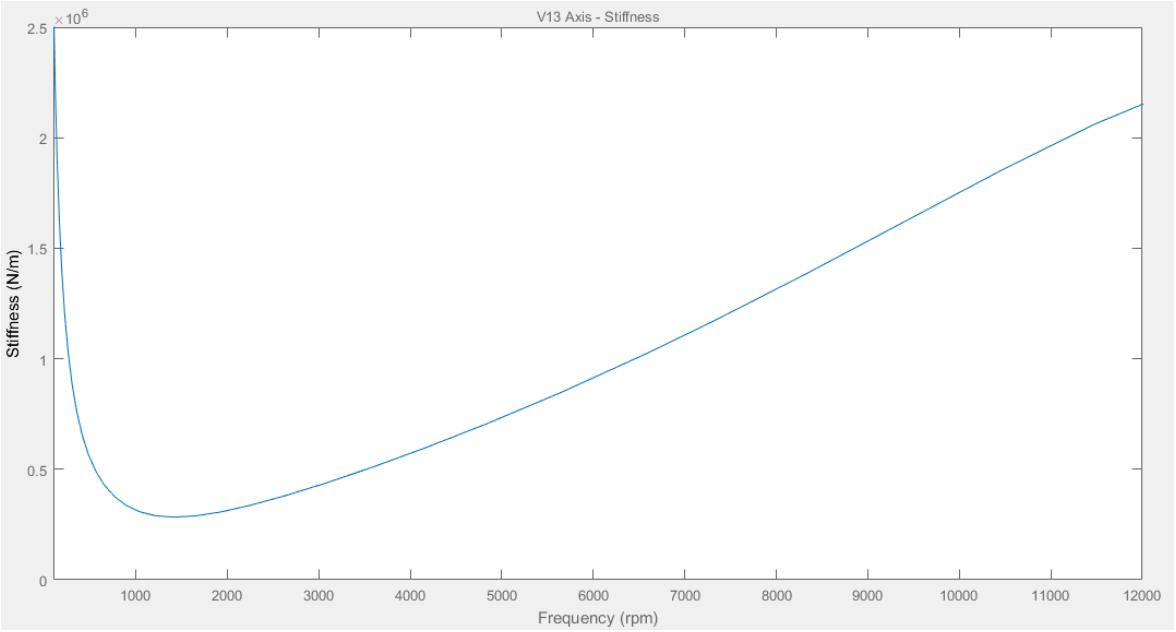

Figure 5-17: Stiffness of AMB for V13 Axis.

5.13 Critique

In this chapter, the actuators (AMBs) in the test rig are assumed to be linear in the operating range within the limit of auxiliary bearings. This has been implemented by introducing a bias current in the AMB. In practice, there might be small deviations, and AMB force vs. electrical current might not be linear when the rotor is operating on high vibration close to the auxiliary bearing inner race which is away from desired centre point of the bearing.

5.14 Summary

In this chapter, the AMB controller parts were studied and integrated with the rotor FEA model. The transfer functions of each controller component (which include displacement (position) sensors, PIDs, Lead Lag filter, 2nd order generic filters, low pass filter, digital signal processing delay, power amplifier and actuator (magnetic bearing)) were extracted. These transfer functions and the rotor FEA state space model were integrated in a Simulink model. The Simulink open loop transfer functions for different axes were compared with the measured data from the MB340g4-ERX hardware. The measured data shows noticeable coincidence with the measured data for each control axis. The sensitivity transfer function of each axis was compared against the ISO14839-3 stability criteria. The rotor stability falls within zone A which is for newly commissioned machines and suggests that the rotor is suitable for running for a long period of time. Finally, the stiffness of AMB was compared against the desired value extracted from rotor FEA and found to be suitable.

Chapter 6

Diagnostics and Fault Finding

6.1 Introduction

One of the important issues in industry is fault diagnosis of rotating equipment supported by AMBs. The rotordynamic behaviour of AMB supported rotors is dependent on the controller configuration and its filters. When compared to rotors supported by conventional bearings, AMB supported rotors have the advantage of additional monitoring parameters such as electric current. The measurement of current provides insight to the amount of force that the AMB exerts on the shaft, or from another perspective, the load on the controller and AMB which is required to keep the rotor in the centre of the bearing. This type of information is not available on other types of bearing such as fluid film or roller element bearings. As with equipment supported by fluid film bearings or roller element bearings, equipment supported with AMBs can experience failures associated with external forces exerted on the rotor (or even in some cases the controller) which might be the reason for these types of failure. Therefore, it is important to be able to diagnose the equipment based on the affects the failure on the measured data. In this chapter, different major defects that are faced in industry are studied. For this purpose different failure mechanisms are simulated on the SKF MBRotor-II rotorkit and the effect of the defect is studied. The selected failures were chosen based on the possibility and capability of simulating the failure on the rotorkit. Some failures, like fluid induced instability where the process fluid comes in contact with the rotor, could not be simulated on the rotorkit because of its limitations.

This chapter requires basic knowledge of rotordynamics such as understanding unbalance, phase and its changes to the rotor's behaviour as it passes through the resonance. For more information the reader is referred to references such as Bently and Agnes books (D. E. Bently & Hatch, 2003; Agnieszka Muszynska, 2005) or industry standards (ISO13373-2, 2016).

6.2 Data Acquisition Equipment Setup

MBScope Orbits, Trending and Snapshots toolsets which are provided as a part of SKF rotorkit, have limited capability in capturing high frequency data and analysing the data synchronously. The data required for diagnostics are vibration, current, shaft position, speed and phase that could be in the form of dynamic values (i.e. waveforms) or static values (i.e. overall vibration or current levels). These data can be used for extracting trends,

orbits, spectrum or waterfall plots, and shaft centre line plots. The MBScope software package has a limitation of 3 channels maximum measurement with a low sampling rate (1 sample/s) indicating that its purpose is primarily for acquiring trending data. The number of channels required for comprehensive measurement is 4 dynamic channels for vibration (displacement) measurement (two per bearing), 8 dynamic channels for measuring current values (four per bearing, one per quadrant) and one Keyphasor channel for measurement of phase, speed and changing the sampling rate as the speed changes, which is similar to order tracking.

To overcome the limitations of the MBScope, alternative external data acquisition hardware (Confidential vendor-supplied data removed from this publically accessible electronic copy.) was adopted to capture high resolution data (synchronous and asynchronous) for all the defined channels. The data acquisition hardware was connected to the already available transducer buffered output on the MBResearch board. On each dynamic channel of the data acquisition hardware, four types of waveform signals were captured. One synchronous time waveform with 128 Samples/rev and three asynchronous wavefroms with sampling rate of 1280, 2560, and 6400 samples/sec. The first waveform (synchronous) is dependent on shaft speed and the sampling rate changes as required to have 128 samples for each rotation. This provides a good quality time waveform by changing the sampling rate as the rotor speed changes to have a consistent 128 samples per each rotation. The three asynchronous waveforms are independent of shaft speed and the sampling rate fixed. They provide high quality spectra for rotordynamic and control system outputs. The scale factors of the sensors are extracted from the MBScope calibration toolset. The data acquisition settings for the V13 axis and the Keyphasor are shown in Figure 6-1. The Keyphasor asynchronous waveform was acquired in order to provide more detail in case the sensor signal became faulty.

Confidential vendor-supplied data removed from this publically accessible electronic copy.

Figure 6-1: V13 Position sensor (which is the same for all other dynamic channels) and Keyphasor sensor setting in the data acquisition system.

The equipment is setup to acquire one waveform per two static samples. The static samples are triggered when the shaft's speed increases or decreases by 10 rpm. This is considered a high sampling rate for industrial equipment as it requires a large amount of data storage. However, as this is laboratory test equipment, and the data capture is for short periods, capturing high data volume is not a limitation.

6.3 MBRotor-II Normal Run Up and Coast Down

On all industrial equipment, after equipment commissioning and acceptance, it is important to record the normal behaviour of the equipment as it provides information on the normal condition of the asset. More importantly, equipment run up and cost down characteristics provides vital information on the status of the equipment such as support stiffness, resonances, residual unbalance and the amount of controller effort required to levitate the rotor. This step is often neglected and leading to the operators facing the problem that they don't have the base line data to compare with the failure data. This commissioning and acceptance data is also vital for condition monitoring and predictive analytics where small changes or deviations trigger advance notifications even before the equipment reaches the alert and alarm thresholds.

The following plots demonstrate the MBRotor-II start up data. The Keyphasor speed trend is shown in Figure 6-2. The rotor reaches the speed of 9000 rpm and then coasts down to stop. The corresponding overall displacement vibration levels and its associated oscillating current for the V13 axis are shown in Figure 6-3 and Figure 6-4. Figure 6-5 shows the Bode plot for run up and coast down of the rotorkit. The resonance of the rotor is at 6502 rpm (108 Hz) which is in line with the FEA model of the rotor. Note that the Bode plot in rotordynamics field is the vibration response of the system based on the frequency of

rotation of the rotor in rpm (D. E. Bently & Hatch, 2003) as it is going through the start up and shutdown of the equipment.

Figure 6-4 shows the top current and bottom control current oscillation which is required to compensate for the vibration measured by the displacement sensor. The major component of vibration is 1X component and as the phase changes with the speed, it is an indication of unbalance. The overall vibration level is shown in blue colour (includes all vibration components 1X and non-1X). These two trends align with each other indicating that the majority of the vibration is caused by 1X excitations. The control current oscillation is required to counteract the effect of unbalance. Figure 6-6 shows the average top and bottom current which is required to keep the rotor in the centre of the bearing. The average current is made up of the average control and bias current components. As demonstrated in the previous chapters, the bias current is required to linearize the control of the AMB. The instantaneous current values for the V13 axis top and bottom current, which was captured at 9001 rpm, is shown in Figure 6-7.

There are different industry standards which defines the acceptable vibration zones for different types of equipment such as gas turbines, pumps, etc. with different power rating (ISO7919, 2009).

ISO14839-2 (2004) defines the vibration zone limits for equipment with power consumption above 15 kW for rotors supported by AMBs. However, this standard was used as a guideline providing acceptable vibration levels for MBRotor-II; although, the power rating of MBRotor-II is lower than 15 kW. The minimum radial clearance C_{min} for MBRotor-II is at the auxiliary bearings and was measured to be 360 μm. The vibration zones based on the above standard are defined as:

Zone A: Normally newly commissioned machines have a maximum peak vibration level lower than the Zone A/B boundary.

Zone B: Normally machines accepted for long term operation have a maximum peak vibration level lower than the Zone B/C boundary.

Zone C: Normally machines with maximum peak vibration levels lower than Zone C/D are not considered acceptable for long term operation.

Zone D: Machines running with maximum peak vibration levels higher than Zone C/D are considered to be sufficiently sever to cause damage to the machine.

Table 6-1: Vibration zone boundaries for MBRotor-II test rig (ISO14839-2, 2004)

Vibration Zone Boundary	Overall vibration limit (μm pp)
A/B	108
B/C	144
C/D	180

Vibration measurement axis	Vibration Level at 9001 rpm (μm pp)
V13	33
W13	26
V24	30
W24	26

The vibration levels at steady state operating speed (9000 rpm) fall within Zone A and are considered acceptable for continuous operation of the MBRotor-II.

This data was considered to represent a normal run of the MBRotor-II and was therefore used as the baseline. The baseline data included vibration levels (1X and overall), phase and the average gap voltage of the rotor at different speed.

Any change in any of the parameters stated is considered abnormal and the condition of the equipment should, as a consequence, be assessed.

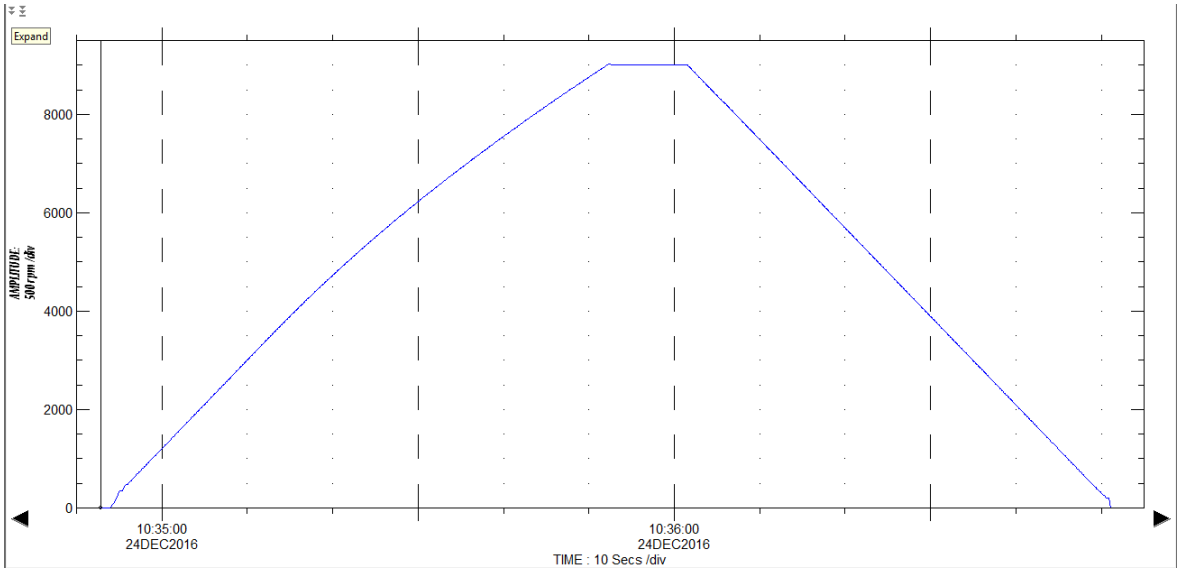

Figure 6-2: Speed trend for normal run up and coast down.

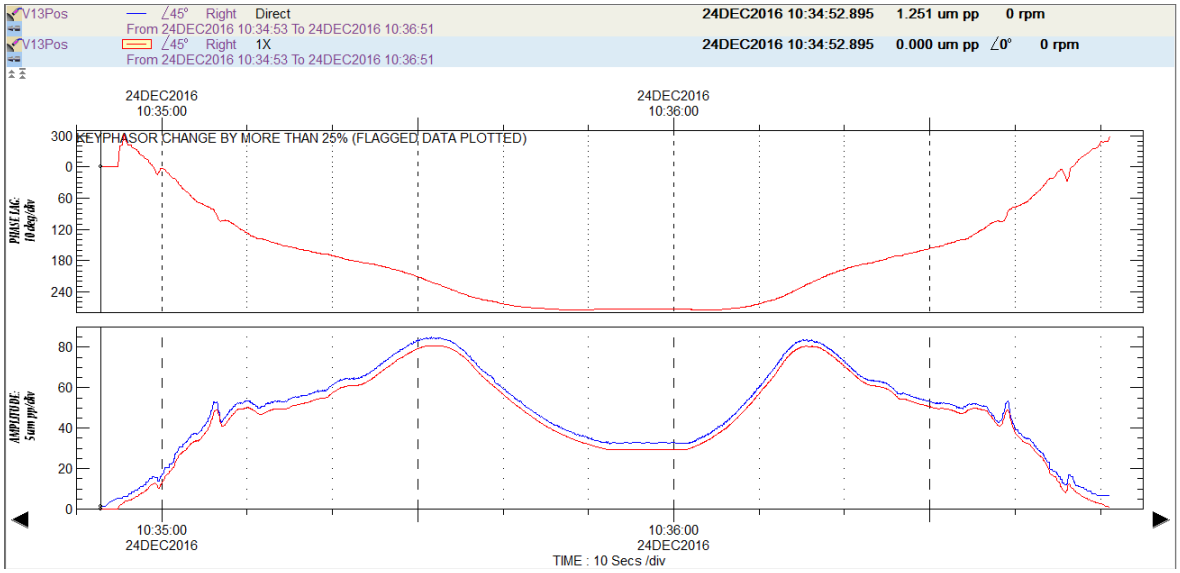

Figure 6-3: V13 axis overall (blue) and 1X (red) vibration trends

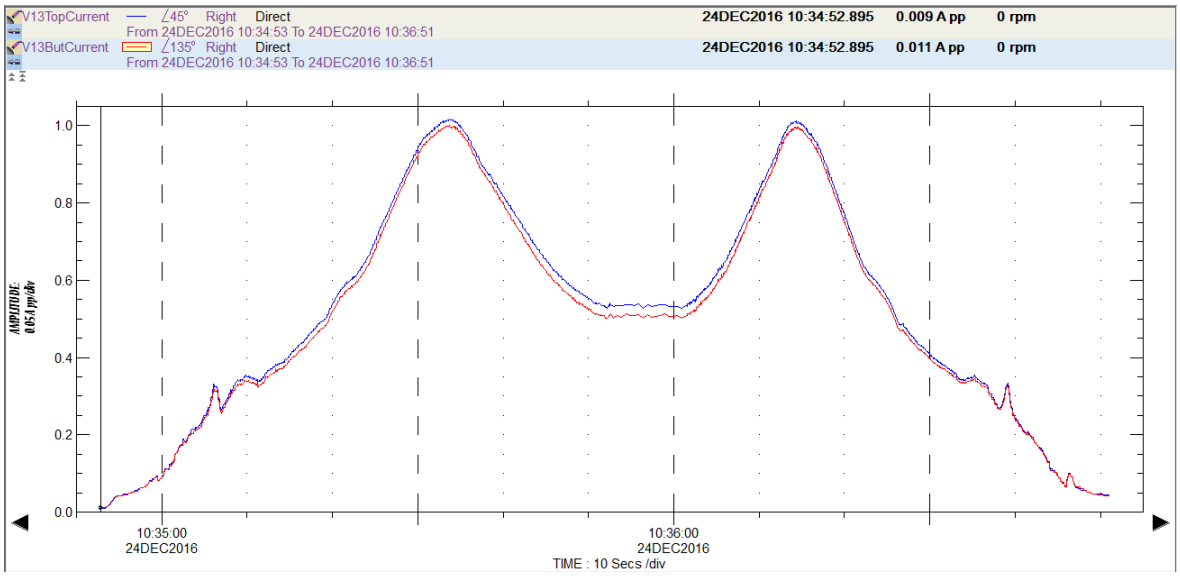

Figure 6-4: Top current (blue) and Bottom current (Red) oscillation for keeping the rotor in the centre of the bearing

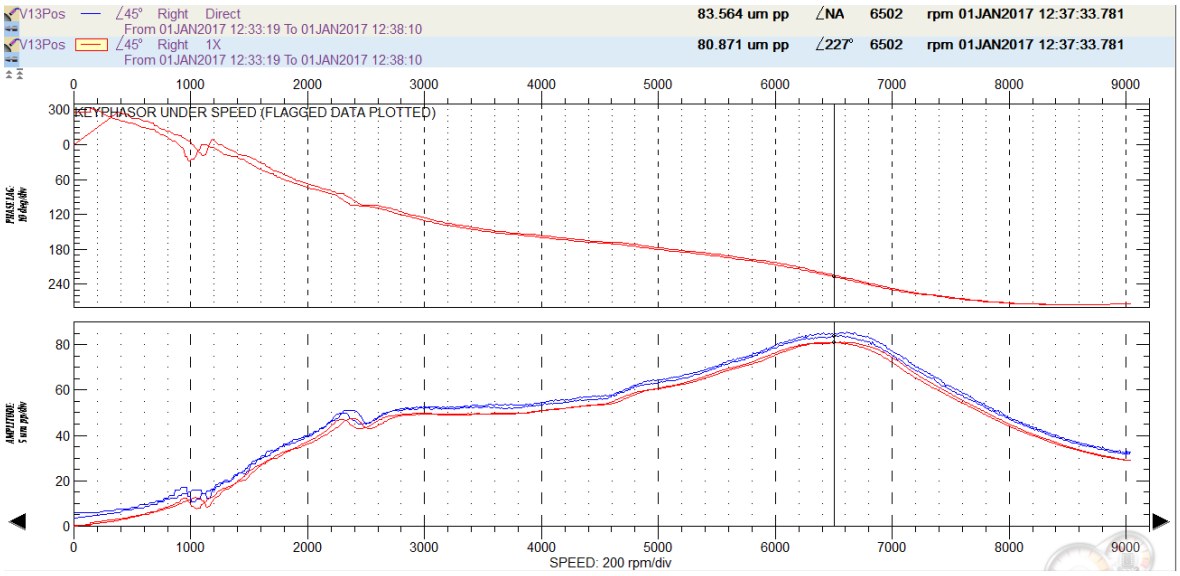

Figure 6-5: V13 displacement sensor Bode plot which shows the resonance at 6502 rpm

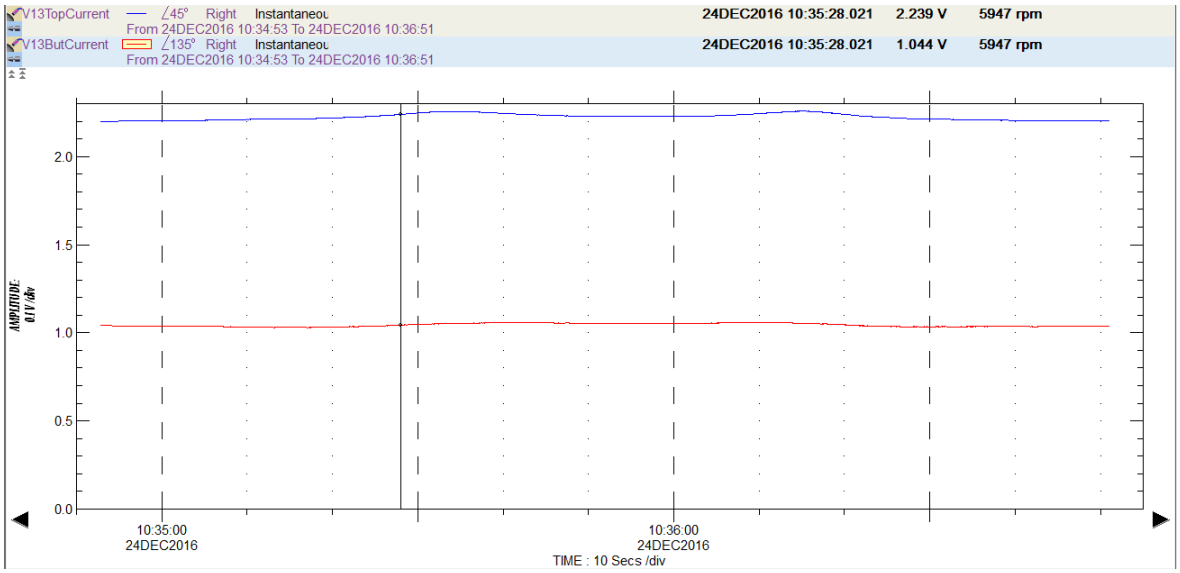

Figure 6-6: V13 axis average top current (blue) and bottom current (red) for keeping the rotor in the centre of the bearing.

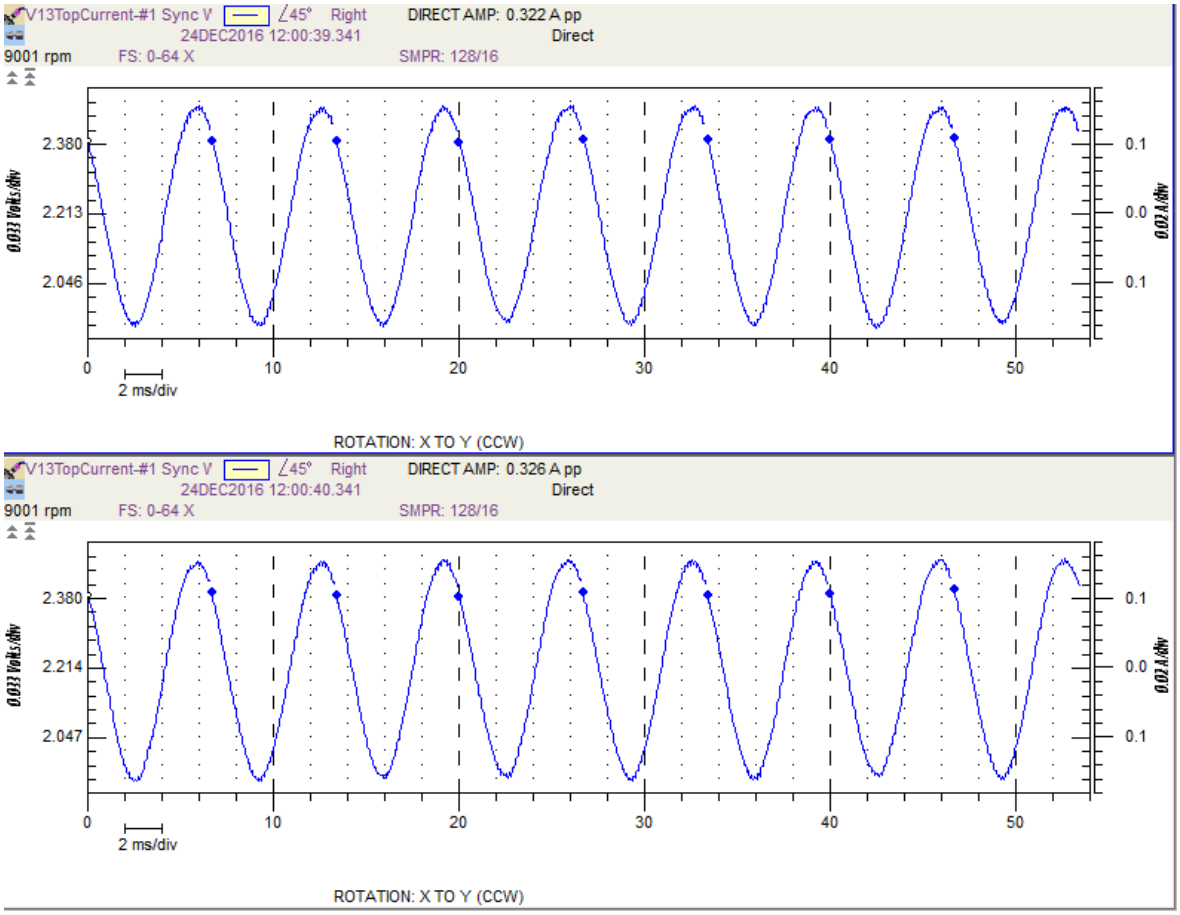

Figure 6-7: V13 axis top and bottom instantaneous current (captured at 9001 rpm)

6.4 Rubbing Simulation on the SKF MBRotor-II

Rubbing phenomena have always been a major deterioration issue in critical rotating equipment. Although rubbing is a secondary effect and not a root cause, it can cause other issues such as failure of bearings or seals that then reduce machinery performance, or in some cases, can cause failure of blades or stator components which then lead to costly maintenance outcomes. These phenomena have been widely studied. Padovan and Choy (1987) have studied the rubbing between rotor blades and the casing in high speed rotating equipment. Agnieszka Muszynska (2005) has reviewed the literature and modelled the interaction of the shaft with the stator. The physical contact of a rotor with the stator can cause impact, friction or changes of stiffness and in some cases thermal effects. The friction is caused by the tangential force between the rotor and stator and so depends on the surface material and normal forces. The friction will also cause thermal effects on the rubbing point (high spot). (2002) have studied the dynamic friction effect and coupled bending and torsional vibration of a rotor system. (2009) have investigated a partial rotor-stator rub. They modelled the rub phenomenon and compared the result with experimental studies. Based on their research the synchronous vibration level should increase and there would be some peak response at 1/3 and 2/3 of running speed of the rotor.

In this part of this thesis a practical diagnostics approach, focusing on rotors supported with AMBs, is considered for analysis of data captured on the AMB test rig. Rubbing phenomena are induced while the rotor is rotating at constant speed. The rub was simulated by a fixture attached to the base of the rotorkit. Figure 6-8 shows the rub stand assembly. The adjustable nut is made of plastic so it can simulate rubbing phenomena while at the same time avoiding damage to the rotorkit shaft. The height was varied by the adjustable nut which contacts the rotor. The rub stand was installed between the rotorkit disk and the Non-Drive End (NDE) bearing.

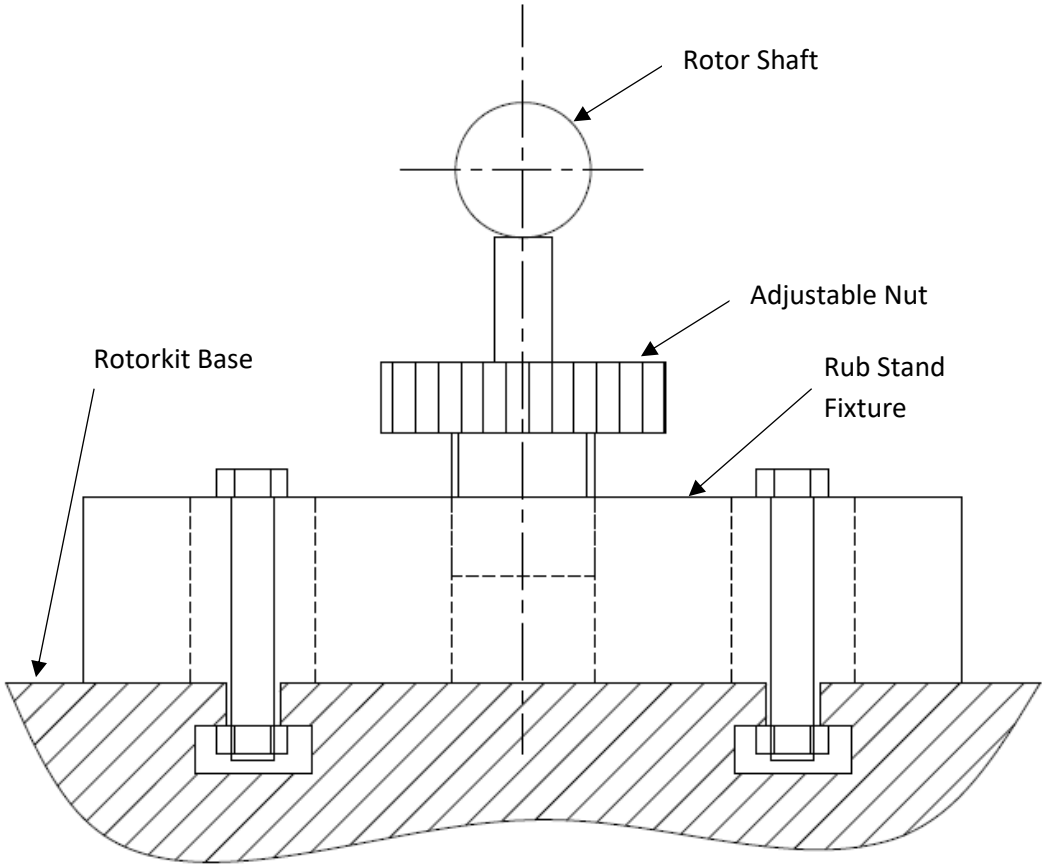

Figure 6-8: Rubbing stand schematic

The rubbing phenomenon, being closer to the NDE bearing, shows higher vibration amplitude on the V24 and W24 axes. Therefore, the vibration analysis focused on the signal which tripped the rotorkit as a result of high amplitude of vibration. Figure 6-9 shows the vibration trend of 1X (synchronous vibration in red) and overall vibration level in blue for the W24 axis. The amplitude of vibration reached the alarm limit and caused rotorkit to shutdown. The vibration increase is shown in the overall vibration trend (blue) while the trend is stable on 1X component of vibration. This is an indication that the high vibration levels are caused by non-1X vibration components. The peaks of the overall vibration signal shows the periods over which the rubbing phenomenon has occurred. There is no change in the 1X component and its phase which indicates the time of contact was insufficient to make a hot spot on the rotor. The rubbing was intermittent as the nut was adjusted at different times. The nut could not be adjusted while the machine was at stop since during the resonance the rotor would rub at the nut and high vibration would trip the rotorkit.

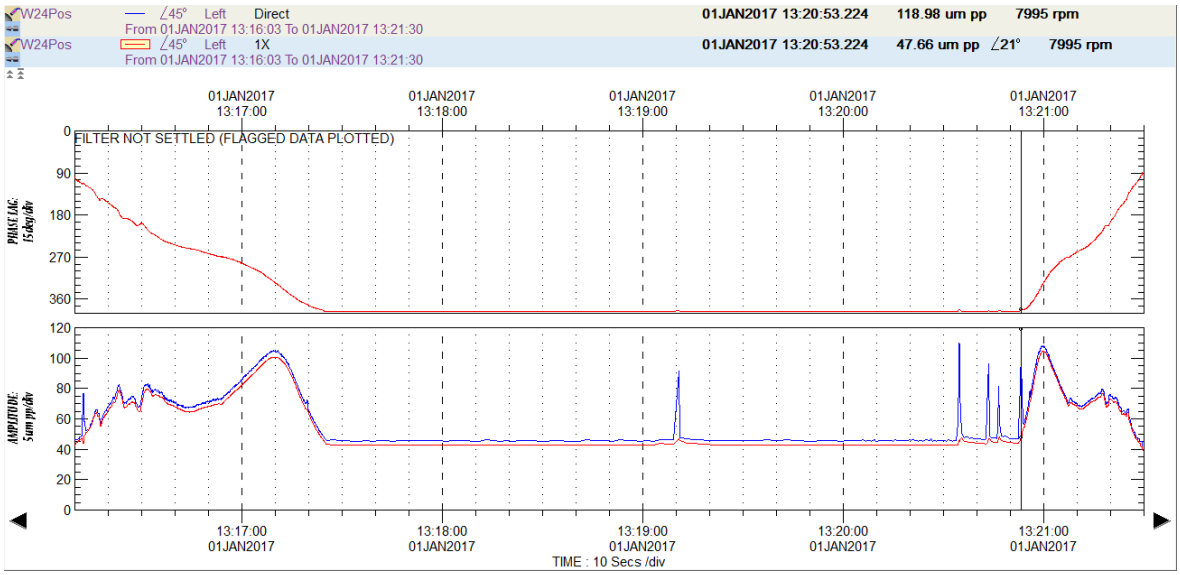

Figure 6-9: Vibration trend for the W24 axis showing high level of vibration during rubbing phenomena (direct vibration in blue and 1X vibration in red).

Figure 6-10 shows the full spectrum waterfall plot during run up, steady state speed and coast down (green, red, blue colour respectively). During rubbing at steady state speed sub-harmonic peaks (frequencies lower than running speed frequency) and super-harmonic peaks (frequencies higher than running speed) were observed. As noted earlier, these frequencies increase overall vibration level but not the synchronous frequency vibration level. The plot is divided into two halves; reverse precession vibration frequencies (left side) which are in the opposite direction of shaft rotation, and the forward precession vibration frequencies (right side) where the vibration is in the direction of shaft rotation. The black arrows show the synchronous vibration peaks for 1X-forward precession.

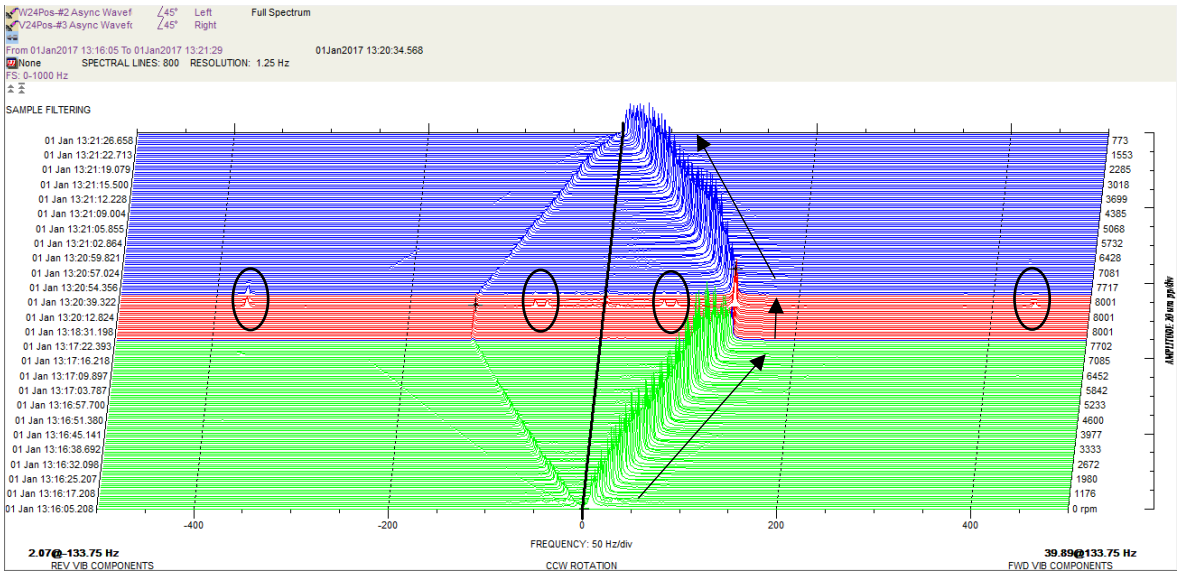

Figure 6-10: Full spectrum waterfall plot for NDE bearing.

Figure 6-11 shows the orbit plot of the shaft precession during rubbing, in blue, compared with the orbit of the shaft during the normal condition, in orange. As observed, the hard rubbing against the rubbing nut has caused bouncing of the shaft and abnormal vibration of the shaft. The main component of vibration in the normal condition (orange colour) is 1X, related to unbalance forces. The blue orbit plot shows other frequency components that are added to the unbalance vibration which may be identified more clearly in spectrum plots. Note that the hard rubbing threshold or contact point could not be defined in the measured orbit. The location of rubbing is not at the bearings but between bearing and the rotor disk. The hard contact/rub is like an impact that caused the rotor to bounce back at the rub location which shows itself in a different way at the measurement location.

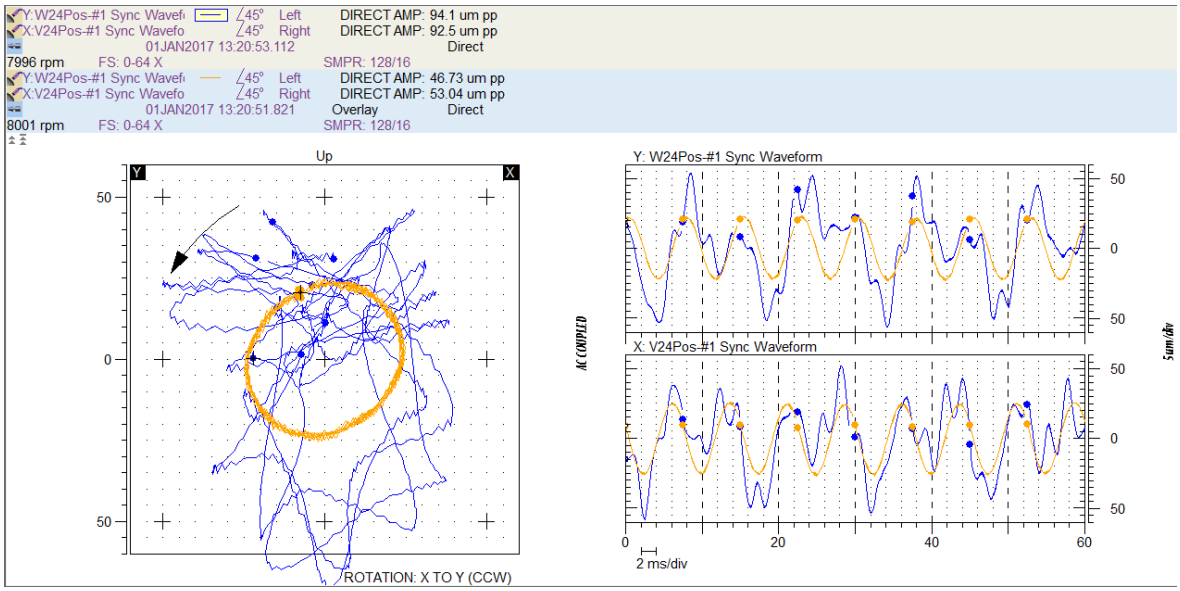

Figure 6-11: Orbit plot for the NDE bearing during rub in blue and in normal condition in orange.

Figure 6-12 shows the NDE bearing full spectrum plot showing both reverse and forward precession frequency components. Rubbing against the rubbing nut produces a wide spectrum of energy that can excite the natural frequencies of the rotor. Figure 6-13 shows the Campbell plot of the MBRotor-II which was extracted from the FEA model. The dashed blue lines show the 1X, 2X, 3X, and 4X of rotor speeds and the black lines show the damped natural frequencies of the rotor across the speed range of the horizontal axis. As a result of gyroscopic forces and coupling of the forces in two axes, the forward and reverse damped natural frequencies of the shaft change as the speed increases (Refer to equations (4-19),(4-20) which demonstrates equation coupling). The black squares show the damped natural frequencies of the rotor at 8000 rpm (the rub speed of the rotor). The 367 Hz (reverse) and 443 Hz (forward) peaks identified in the full spectrum plot approximately match the Campbell plot values of 377 Hz and 442 Hz. The sub-synchronous peaks at 60 Hz and 74 Hz might be related to friction as a result of tangential forces. However, these peaks could not be associated with critical speed frequencies or the running speed frequency. Abuzaid *et al*. (2009) studied the effect of a partial rub theoretically and experimentally on a rotor. Based on their research the synchronous vibration level should increase and there would be some peak response at 1/3 and 2/3 of running speed of the rotor. However, these peaks were not observed with the rubbing phenomenon and the captured spectrum plots on MBRotor-II. There has been other research on full annular rub of the rotor in auxiliary bearings which occurs in the case of shaft drop (deactivation of the AMB). Such research P.

Keogh and Cole (2017), Keogh and Patrick (2012) and (2017) mainly focus on the shaft rubbing against the auxiliary bearing in an emergency situation or shaft drop. The type of contact considered in these papers is full annular rub and which is different from partial rub studied in this thesis.

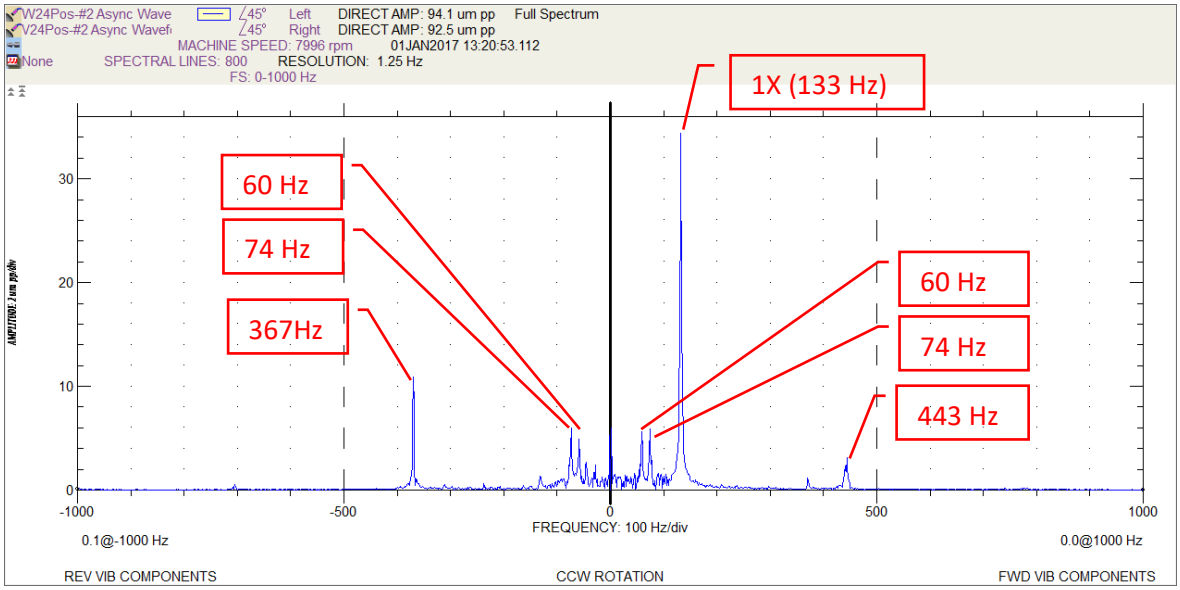

Figure 6-12: NDE bearing full spectrum plot before the high vibration shutdown.

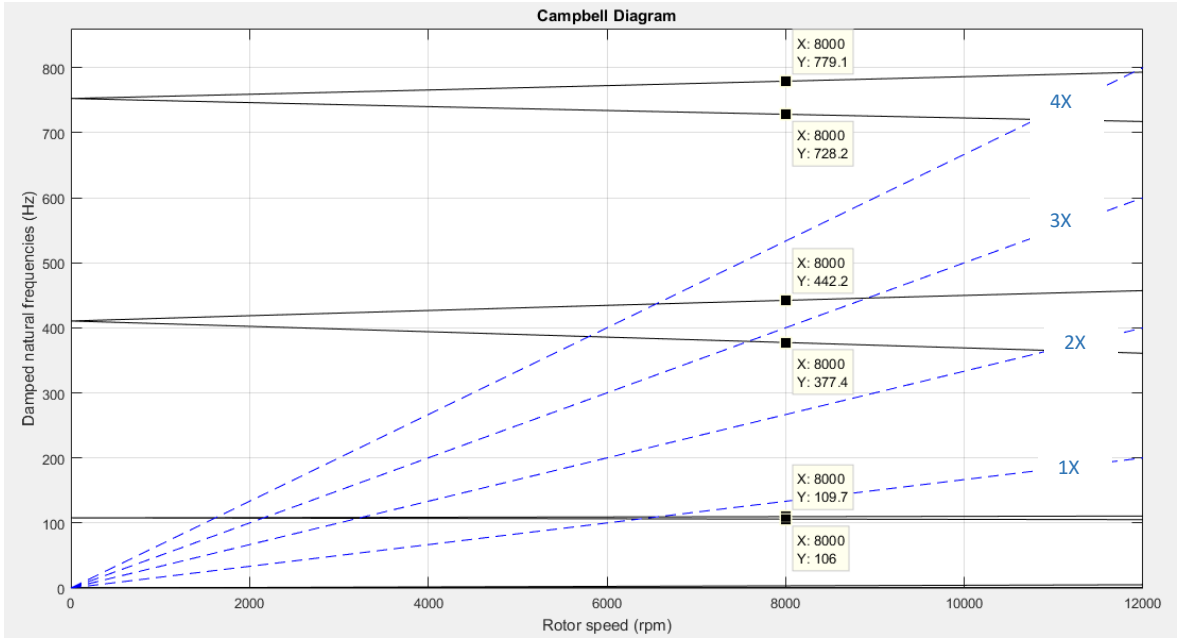

Figure 6-13: Campbell plot of the MBRotor-II rotor.

In the case of AMBs, the shaft centre line plot should show the rotor position in the middle of the bearing. The instantaneous gap voltage can be used as a measure of the shaft centre line position in steady state operation. The specification for shaft centre line position filter

is provided in Table 6-2 and this type of filter is shown on top of each shaft centre line plot. Figure 6-14 shows the shaft centre line plot during constant speed of 8000 rpm and under rubbing conditions. MBRotor-II shaft has a low mass compared to the base and as such the rubbing forces on the shaft will cause the shaft centre line to be moved away from the steady state condition for the duration of rubbing. Figure 6-15 shows the same plot but 'zoomed in' for clarity. It is observed that during the rubbing the shaft has excursions from the bearing centre line. The abnormal movement caused by rubbing against the rubbing nut has caused a total movement of 5 μm of the shaft centre line. Figure 6-16 demonstrates the shaft orbits in the bearing clearance including contact with the rubbing nut.

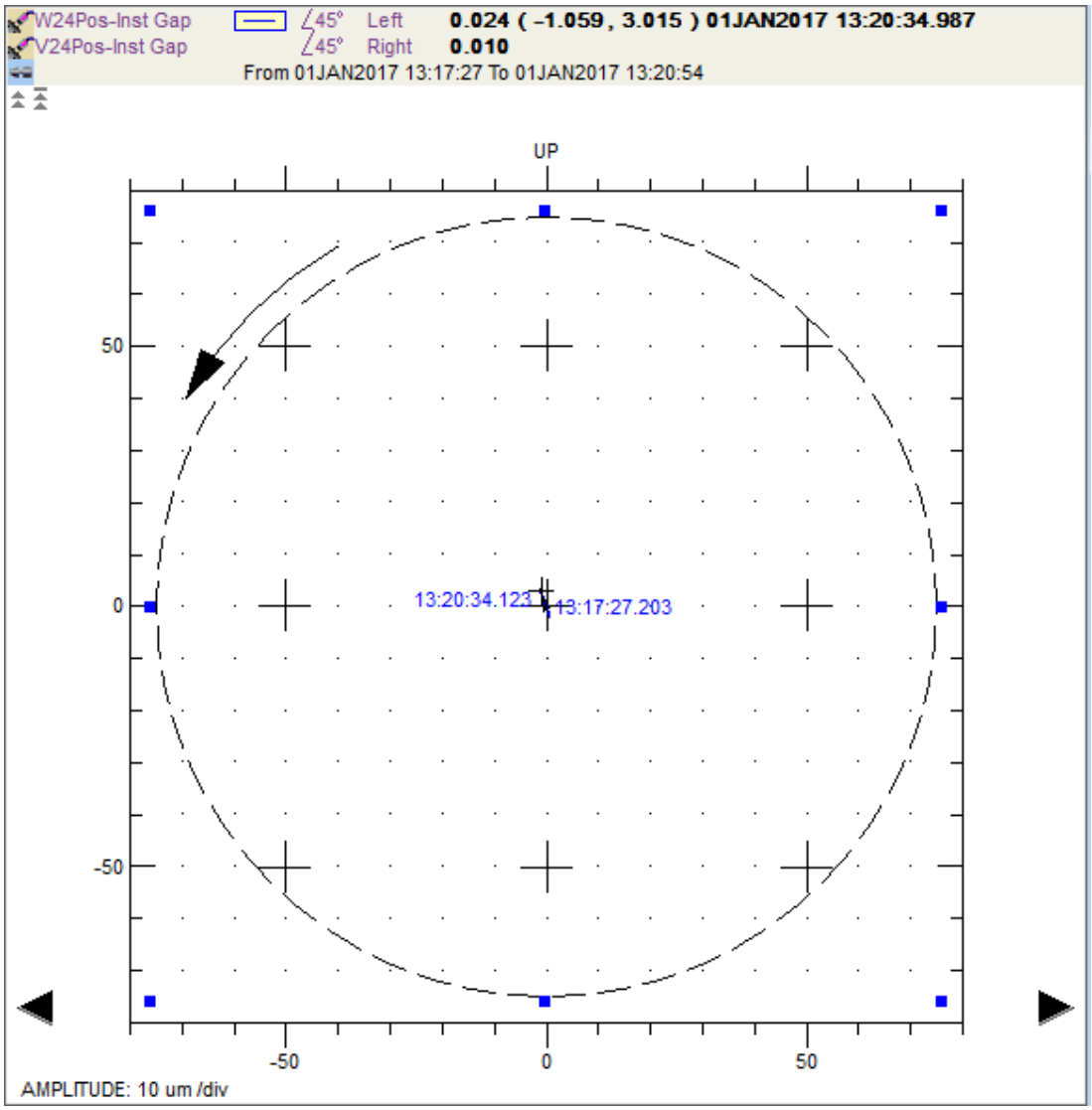

Figure 6-14: Shaft centre line plot for NDE bearing showing the position of the shaft (based on instantaneous gap voltage) compared to the clearance of the bearing (dashed circle).

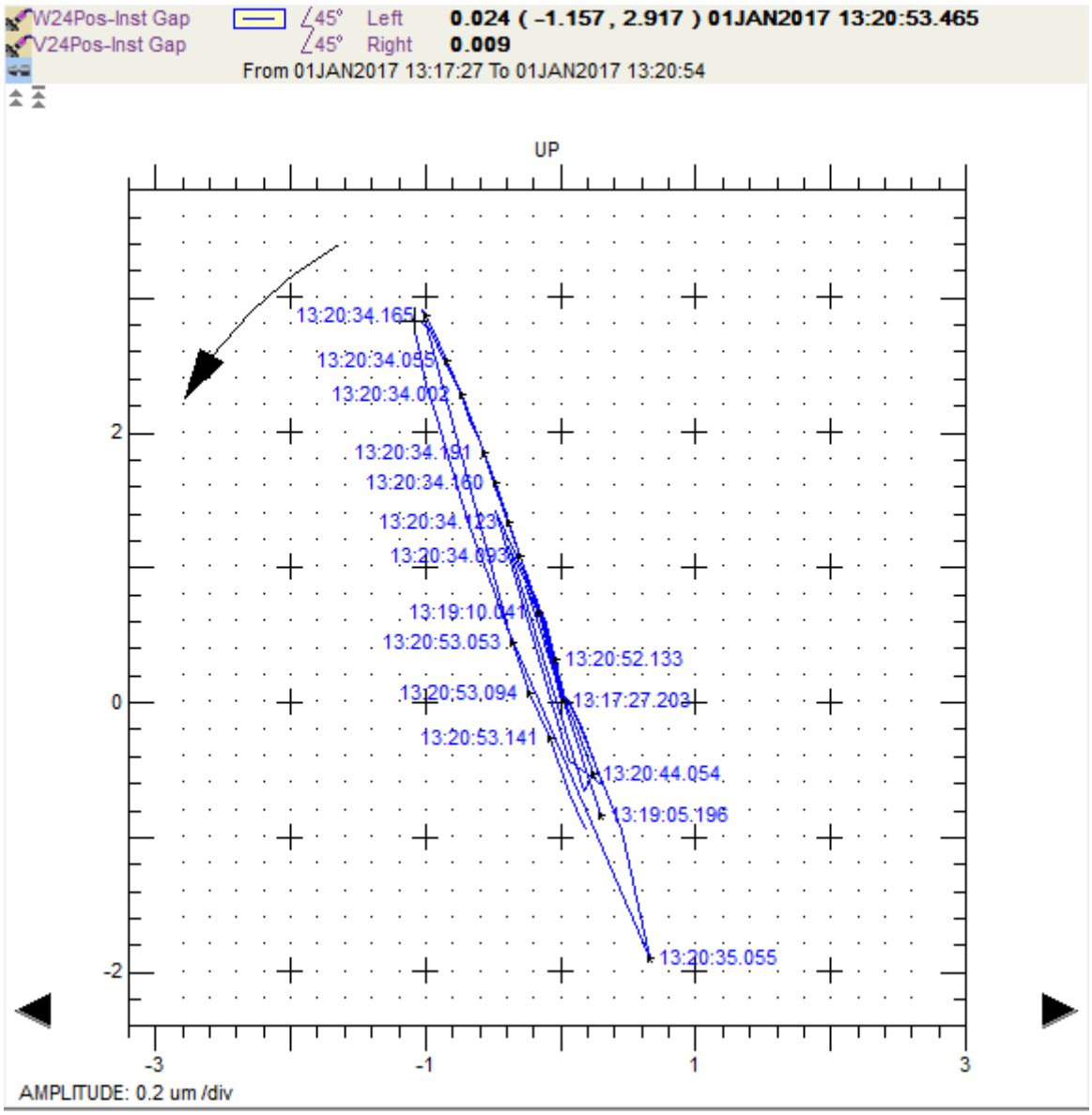

Figure 6-15: Shaft centre line plot for NDE bearing (zoomed) during steady state and rubbing condition.

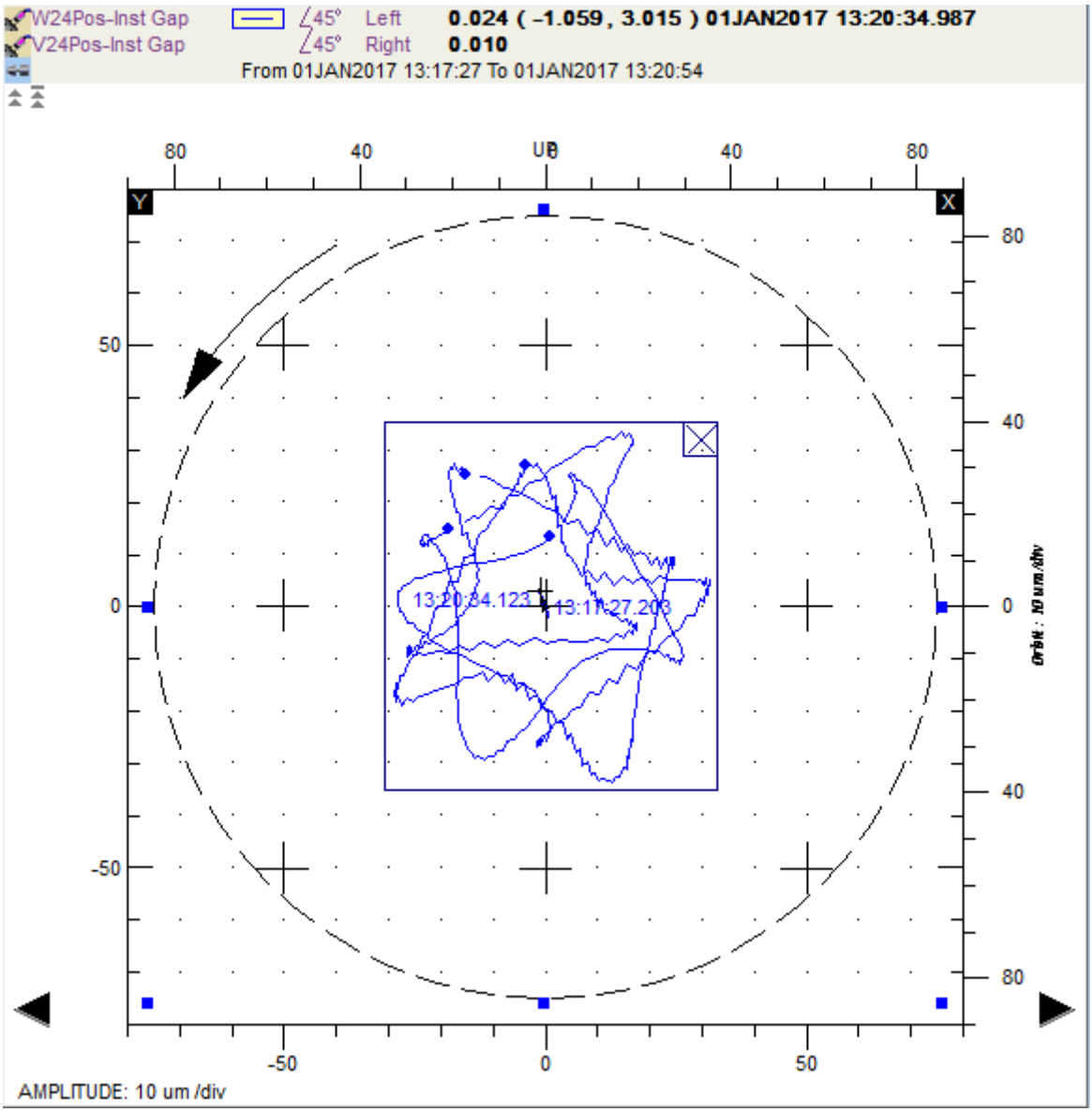

Figure 6-16: Shaft centre line plot for NDE bearing including shaft orbit during the rub condition.

The DAQ specification for measurement of instantaneous and average gap voltage filter is shown in Table 6-2.

Table 6-2: Instantaneous and average gap voltage measurement for shaft centre line plot.

Confidential vendor-supplied data removed from this publically accessible electronic copy.

Partial rubbing of a rotor against and stationary parts, for a simple rotor (e.g. MBRotor-II), has been modelled by Agnieszka Muszynska (2005) and the result is shown in equation (6-1). The vibration pattern extracted from the model can be compared to the vibration pattern of the rotorkit.

$$z(t) = R_s e^{j(\Omega t+\nu)} + \left(\dot{z}_0 + \zeta\omega_n \frac{P(1+j\mu)}{K} e^{j\nu} - j\Omega R_s e^{j\nu}\right) \frac{1}{\omega_d} e^{-\zeta\omega_n t} \sin\omega_d t + \frac{P(1+j\mu)}{K} e^{j\nu} \left(-1 + e^{-\zeta\omega_n t} \sin\omega_d t\right) \quad (6\text{-}1)$$

where:

z : the response of the rotor equal to $x + i\ y$

R_s : obstacle radius measured from the bearing centre

Ω : rotor rotation speed

ν : angular orientation of the stator obstacle

ζ : rotor damping factor

P : average value of radial force over the orbital cycle

μ : dry friction coefficient

ω_n : rotor natural frequency

ω_d : rotor damped natural frequency

The first part of the equation is the synchronous vibration caused by unbalance of the rotor. The second term is the rotor damped free vibration which depends on the rotor speed, initial velocity and the position of the obstacle. The last component is the response of the force P.

Agnieszka Muszynska (2005) has modelled two cases of rubbing. Rubbing with a low contact force (impact) and a high contact force (impact) between the rotor and stator which is shown in Figure 6-17, using equation (6-1).

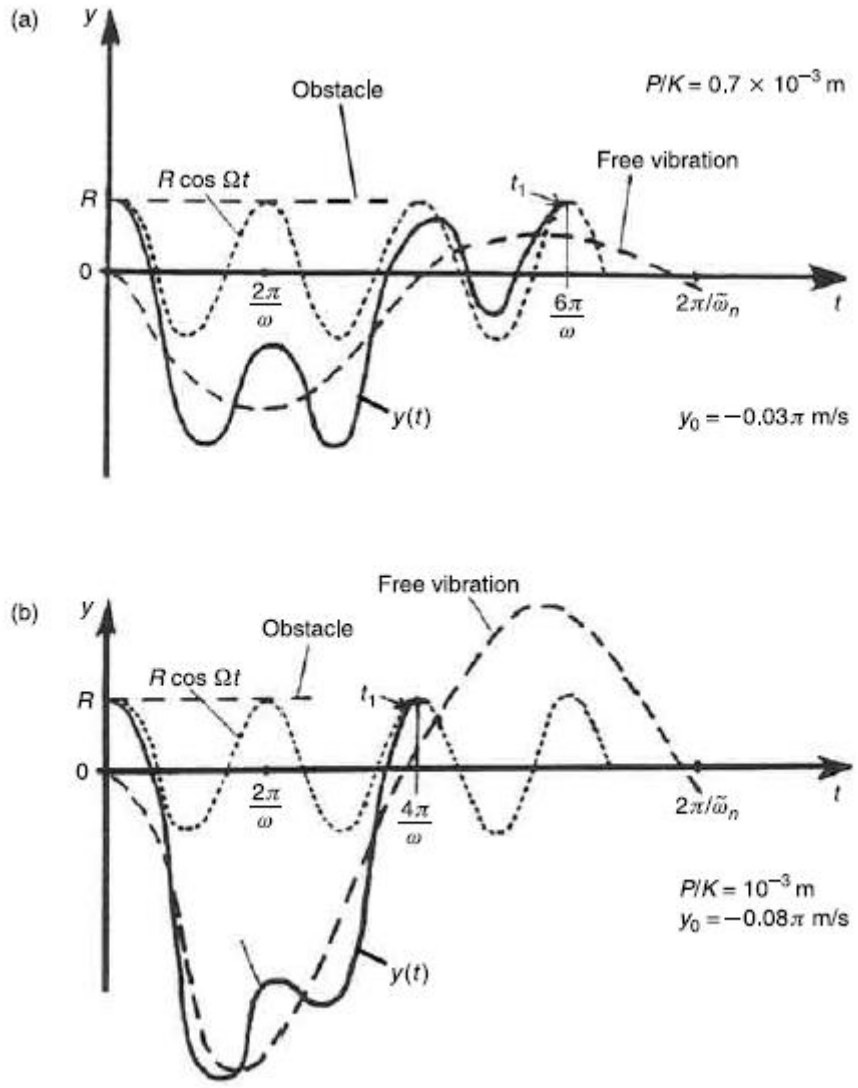

Figure 6-17: Modelled rotor rub against stator. (a) low contact force (P) and low initial velocity. (b) high contact force (P) and high initial velocity between the rotor and stator

The MBRotor-II NDE position sensor data during a portion of the rubbing is shown in Figure 6-18. The position time waveform measurements show a similar response to Figure 6-17(b) which indicates high impact forces on the rotor. The MBRotor-II rotor has low mass and stiffness compared to the structure and the stiffness of rubbing stand. This causes the rotor to bounce back severely after the contact. Based on the experimental results of Agnieszka Muszynska (2005), low contact force results in 1/3, 1/4, and 1/5 subharmonics while high contact forces result in 1/2 subharmonics which is similar to the observations of the rub

experiment in this thesis. Note that the previous experience was gained on rotors supported with fluid film bearings while the current research investigates the failure effects of AMB supported rotors.

The patterns observed in Figure 6-17(a) are common in industrial applications where rotor rubbing against a seal occurs, the weight of the rotor is high and seal material is soft compared to that of the rotor (Ehtemam, 2012), (Ehtemam, 2016).

Figure 6-19 and Figure 6-20 show the current measurements on quadrants of the NDE bearing which shows the controller's strong effort to correct the shaft position. The opposite quadrants (V2 – top current vs. V4 bottom current) show signals which are out of phase, indicateing strong signals that were sent by addition and subtraction of the control signal from bias current in opposite quadrants.

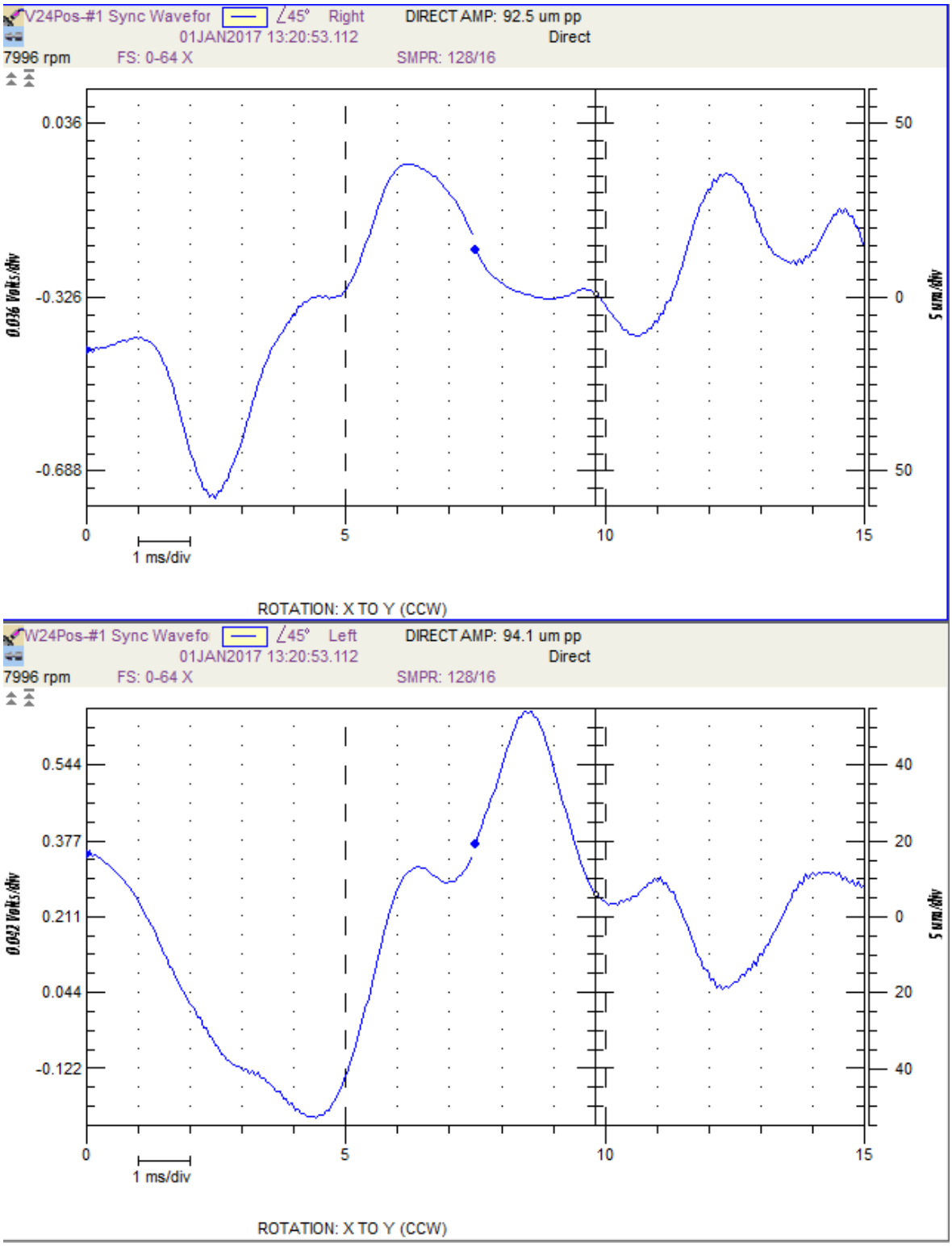

Figure 6-18: NDE bearing position sensor time waveform during rubbing

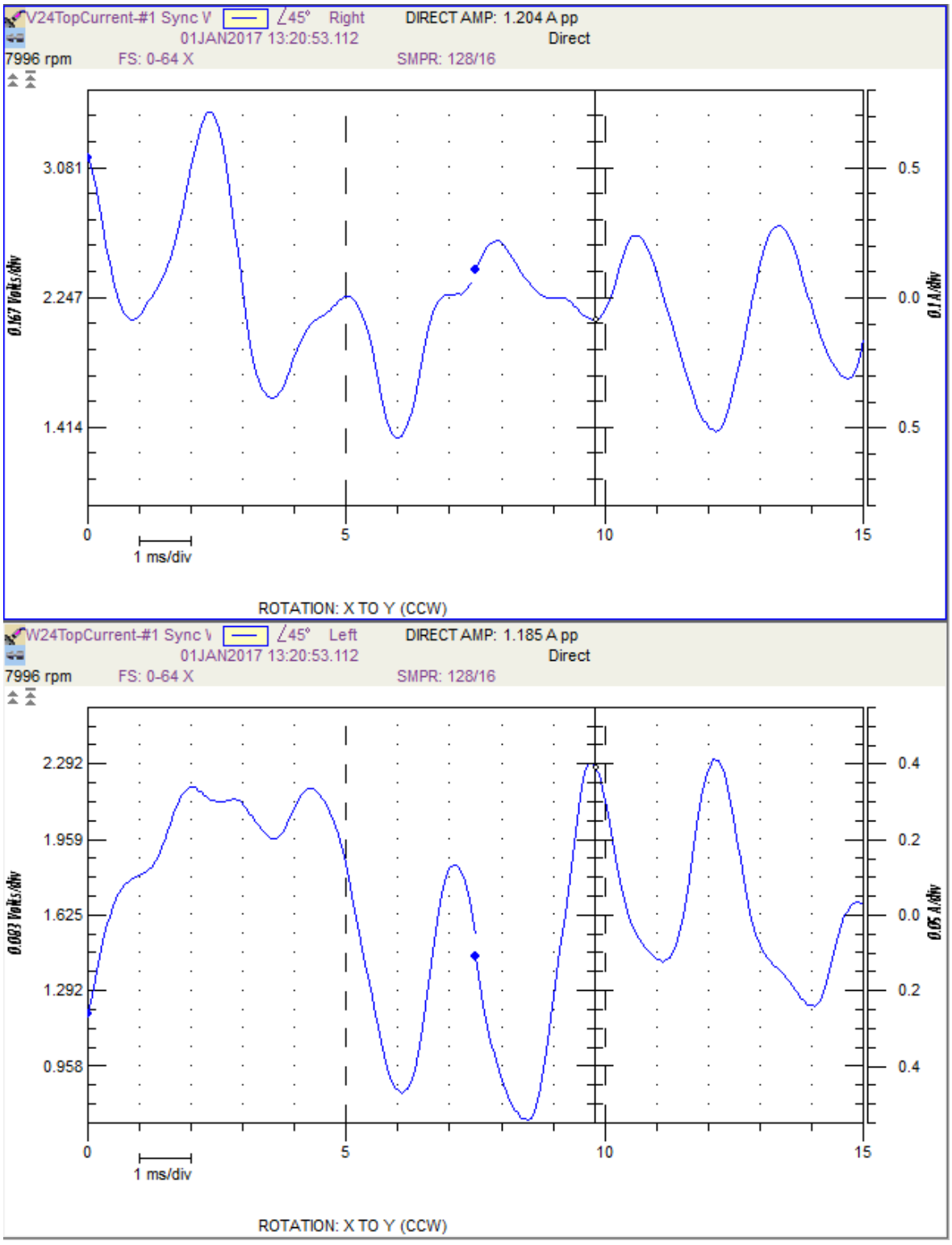

Figure 6-19: V2 and W2 current time waveform measurement during rubbing

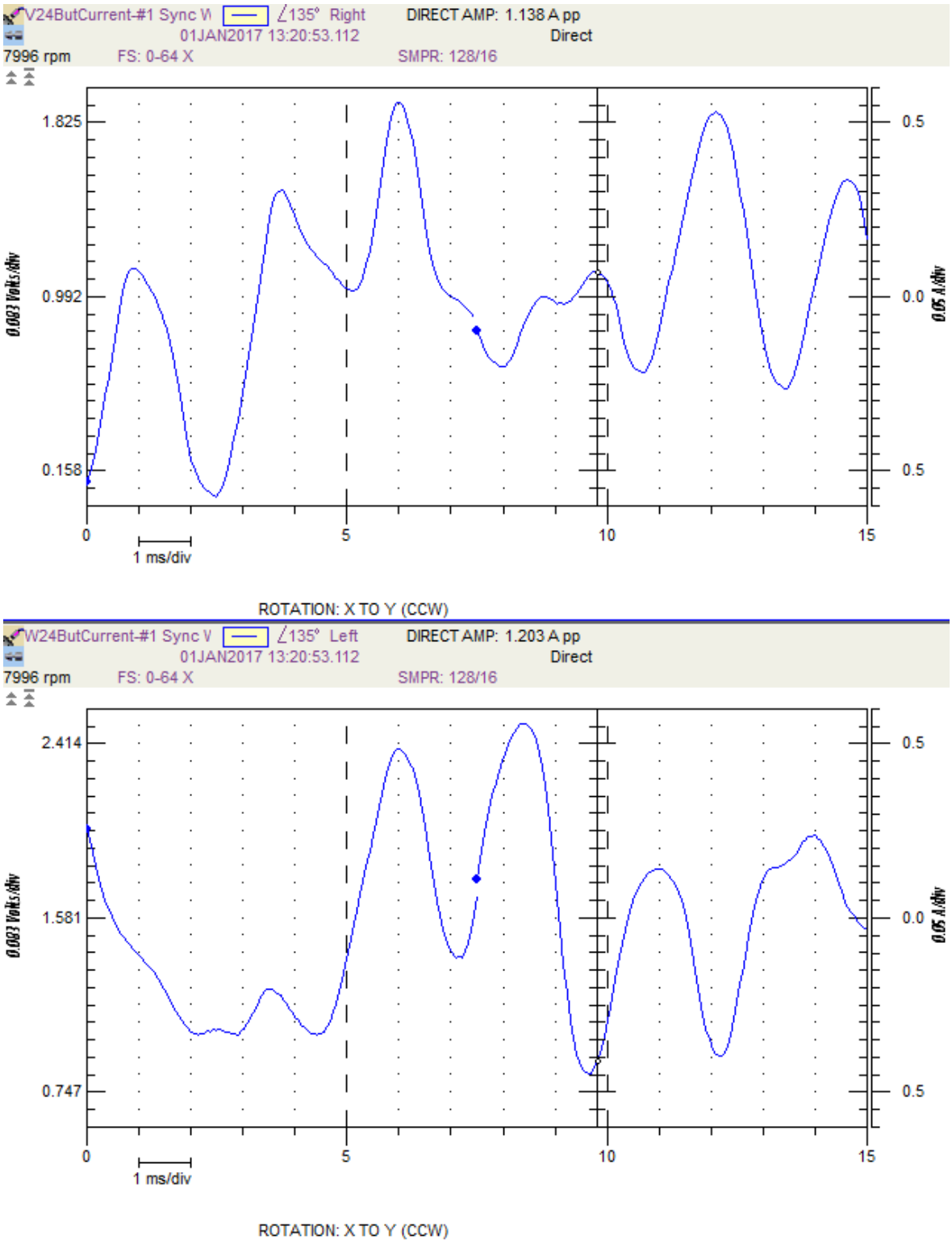

Figure 6-20: V4 and W4 current time waveform measurement during rubbing

In summary, rubbing the rotor against a stationary part causes an impact and friction on the rotor. The impulse excites the resonances of the rotor that were observed in the waterfall and spectrum plots. The natural frequencies at a specific speed was extracted from Campbell plot that was derived from the FEA model. The orbit plot of the shaft shows

high vibration of the rotor as a result of impact and bounce back. The average shaft centre line plot also shows the movement of the shaft centre as a result of forces applied by the stationary part on the rotating part. Rubbing can cause some sub-synchronous frequencies that were observed on the spectrum plot. Rubbing has minimal effect on the unbalance response and its associated phase of the rotor on the rotorkit experiment. However, in industrial applications, rubbing against stationary components, such as seals, might cause heating of the rotor at the point of contact which causes the temporary shaft bow. The shaft bow results in changes in unbalance response of the rotor and its associated phase (1X component). This phenomenon has been described as the Newkirk effect and has been studied in detail (Dimarogonas, 1973; Goldman, 1995; Newkirk, 1927).

Rubbing is a secondary effect arising from other issues in the rotor system. The root cause might be high unbalance forces, misalignment, instability in the bearings (fluid film or AMB), process forces, wrong maintenance practices that might change the clearances of the machinery or in some cases mounting that caused distortion to the casing. Therefore, the root cause of this phenomenon should be identified rather than replacing the components in the rotating equipment which is a common mistake (Ehtemam, 2012), (Ehtemam, 2016).

6.5 Misalignment of the Motor and the Rotor

One of the common rotating equipment problems in industrial applications is the misalignment in the machine string (Fluke, 2013). This problem causes reliability and availability issues due to downtime of the operating asset. Misalignment can cause failure of the coupling between the driver and driven equipment. It can cause increased loads on the bearings which causes higher operating temperatures in the bearings and coupling. Misalignment creates higher vibration levels as a result of higher cyclic forces that can cause fatigue. AMB supported rotors have the advantage of providing the bearing current measurement which is an indication of controller effort required to force the shaft toward the bearing centre. Such an indication is not generally available on other bearing types.

Misalignment may be caused by different reasons. Misalignment in multi-bearing rotating equipment normally happens during the commissioning and installation or after major overhauls while recommissioning the equipment. Misalignment might also occur as a result of deterioration in the structure or the foundation of the machine. Misalignment of

connections, such as process pipes, may cause external forces to be exerted on the casing of the machinery that can lead to distortion and misalignment of the equipment. In AMB supported rotors, it is important that the sensors are calibrated to measure the AMB centre as a reference point. Spangler et al. (2017) have used bias current perturbation for defining the magnetic centre of the AMB. The proposed solution works based on the behaviour of small number of selected points for defining the effective air gap that compensates for the difference between theoretical model output and the measurement results. The SKF MB340g4-ERX controller uses the MBScope-calibration toolset to move the shaft centre line until it touches the auxiliary bearing in each of the four directions related to each quadrant of the AMB. The result of the procedure is used to define the magnetic centre of the bearing and define the scale factor of the sensors (knowing the clearance of auxiliary bearing with the rotor).

In process equipment thermal growth of the equipment is an important factor that needs to be considered in alignment (Yung, 2001). During operation, process equipment might experience high levels of temperature differential compared to the non-operating conditions. The alignment values during the cold condition have to be provided by the vendor considering the equipment design or by doing hot alignment checks. When the driver and driven equipment comes to thermal equilibrium, the centre line of the two shafts should be aligned.

For demonstrating the misalignment phenomenon on the MBRotor-II, the motor was misaligned deliberately by putting a 1 mm thick washer under the motor mount as shown in Figure 6-21. The misalignment in AMB supported machine strings can be checked even during stand still conditions, by comparing the measured currents before and after coupling (in case of MBRotor-II, the electric motor). Figure 6-22 shows the MBRotor-II uncoupled from the electric motor. In case of misalignment between the motor and the rotor, the AMB has different currents that compensate for the eccentricity of the shaft as it is forced away from the AMB magnetic centre by the coupling. The position and current values for decoupled and coupled conditions of the MBRotor-II is demonstrated in Table 6-3. The position gap voltage is the same with and without misalignment condition. This indicates that the rotor centre position is the same in both conditions because of the flexible coupling. However, the bearing current values changed as a result of misalignment

between the motor and the driven rotor demonstrating that controller effort is required to keep the shaft in the centre of the bearing.

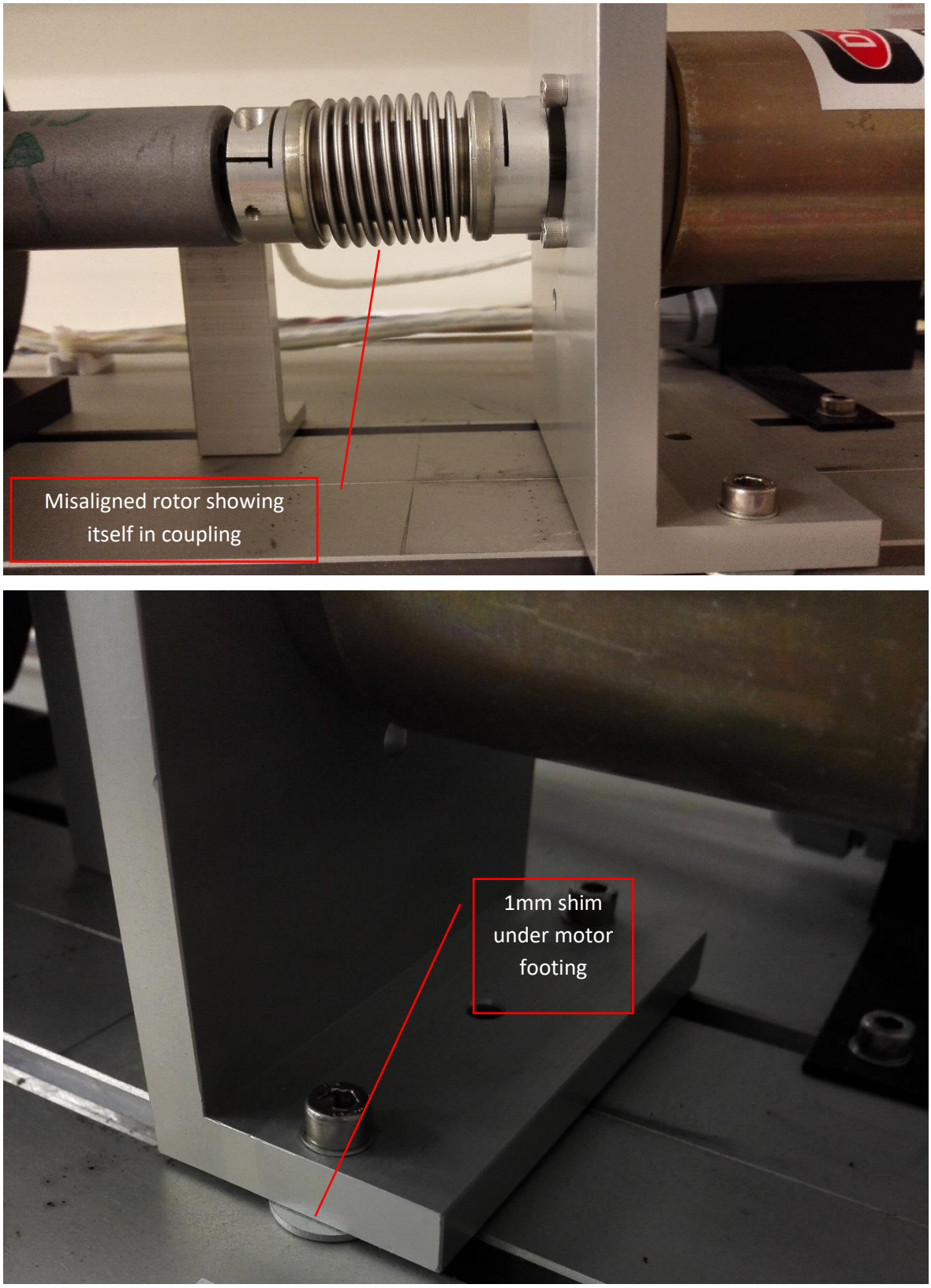

Figure 6-21: Misaligned rotor with a 1mm shim under motor footing.

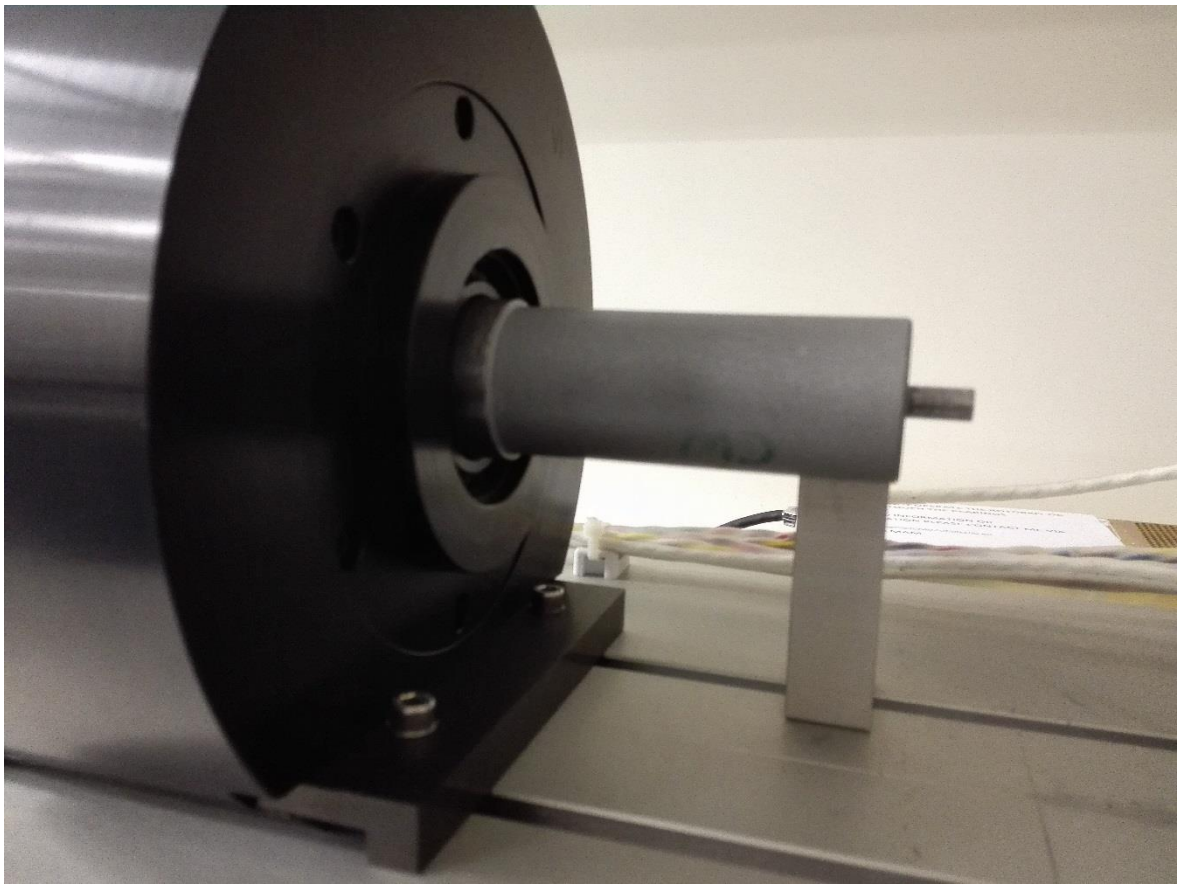

Figure 6-22: MBRotor-II uncoupled from the electric motor.

Table 6-3: Position and current values for coupled and uncoupled condition of the rotor.

	Axis	Uncoupled Rotor	Misaligned Coupled Rotor	Unit
Position Gap Voltage	V13	-0.081	-0.081	V
	W13	-0.5	-0.5	V
	V24	-0.344	-0.344	V
	W24	0.177	0.177	V
Top Current	V13	1.2708	1.3314	A
	W13	1.4274	1.4562	A
	V24	1.3512	1.3824	A
	W24	1.0122	1.0212	A
Bottom Current	V13	0.6594	0.5982	A
	W13	0.4644	0.4344	A
	V24	0.5556	0.5232	A
	W24	0.8748	0.8652	A

In the case of a rigid coupling, it is expected there would be different position gap voltage due to the misaligned coupled rotor compared with uncoupled rotor. In addition, the

current difference would be higher showing higher controller effort attempting to move the shaft to the bearing centre.

As expected, the run up and run down vibration behaviour of the rotorkit is different when a misaligned coupled rotor and aligned coupled rotor are compared. Figure 6-23 shows the Bode plots of different runs for the W24 axis. The direct vibration level differs between the two runs while the 1X vibration stays almost the same. This indicates that there are other frequency components in the experiment with misalignment. Figure 6-24 shows the spectrum plot of vibration for the rotor at 2130 rpm. At this speed, as can be observed in the Bode plot the direct vibration level (bottom plot) differs from the normal run (top plot). This could be associated with 2X (twice the running speed of the rotor) which is usually associated with misalignment (D. E. Bently & Hatch, 2003). In addition, at this speed the second natural frequency of the shaft (approximately 415 Hz – refer to Figure 6-13) is excited. Bouaziz et al. (2011) have theoretically modelled the behaviour of misaligned rotors. In their studies, they showed that the rotor shows 2X and 4X superharmonic peaks predominant in spectrum plots for AMBs with four, six and eight magnets. However, the MBRotor-II having misalignment, shows a predominant vibration peak with running speed frequency and a lower peak amplitude at twice running speed frequency. The four times running speed was not observed, unlike that modelled in their theoretical model. At the speed of approximately 2130 rpm, the rotor second critical frequency (~415 Hz) is also excited. These differences might be related to assumptions in their modelling such as a rigid shaft, the coupling being considered as a ball and socket joint located in the intersection of the axes. In comparison, the MBRotor-II has a very flexible coupling and a flexible shaft that passes the first bending mode approximately at 6500 rpm.

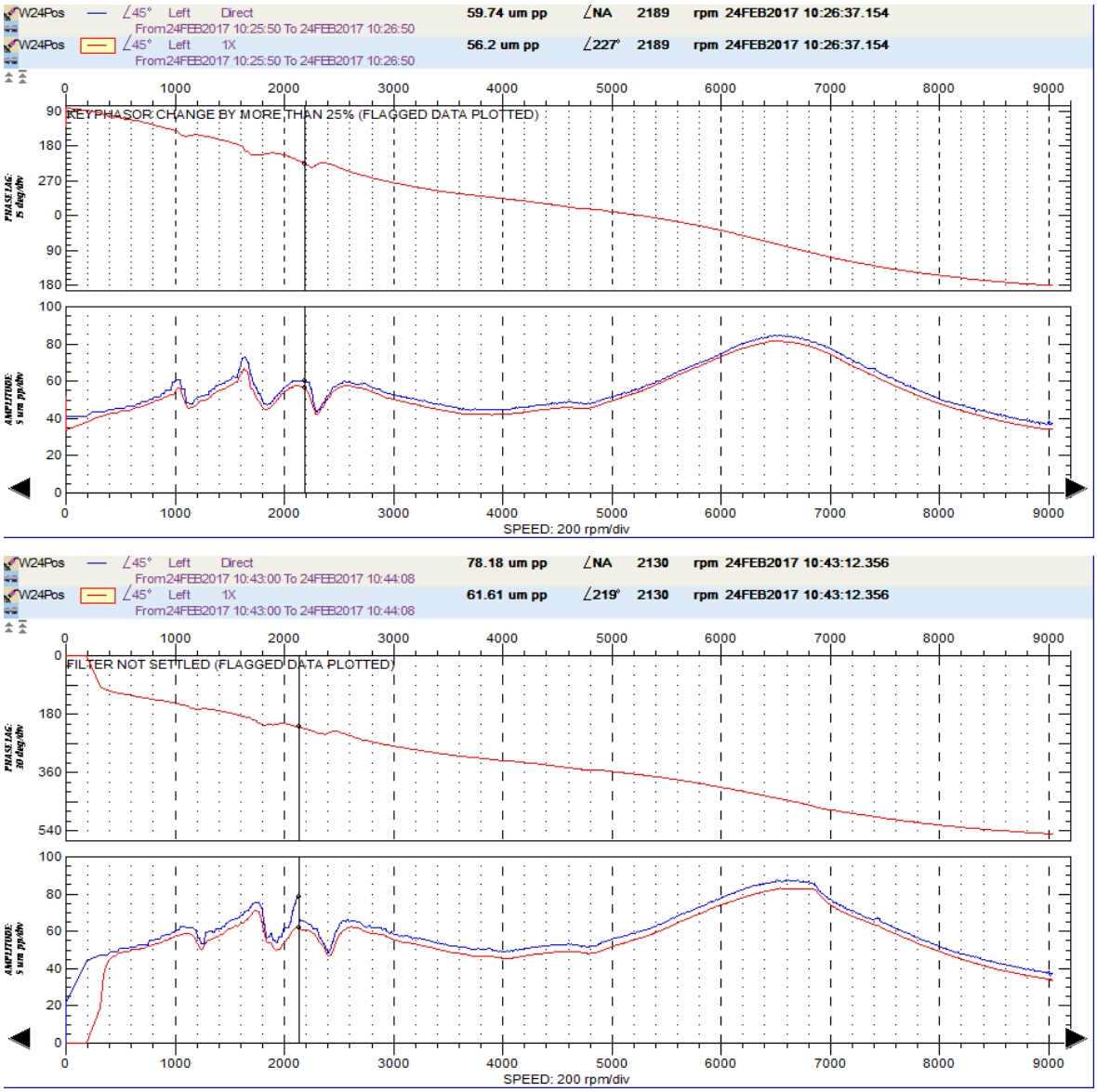

Figure 6-23: Bode plots for aligned (original) run up –top plot - and misaligned run up – bottom plot- for W24 position measurement

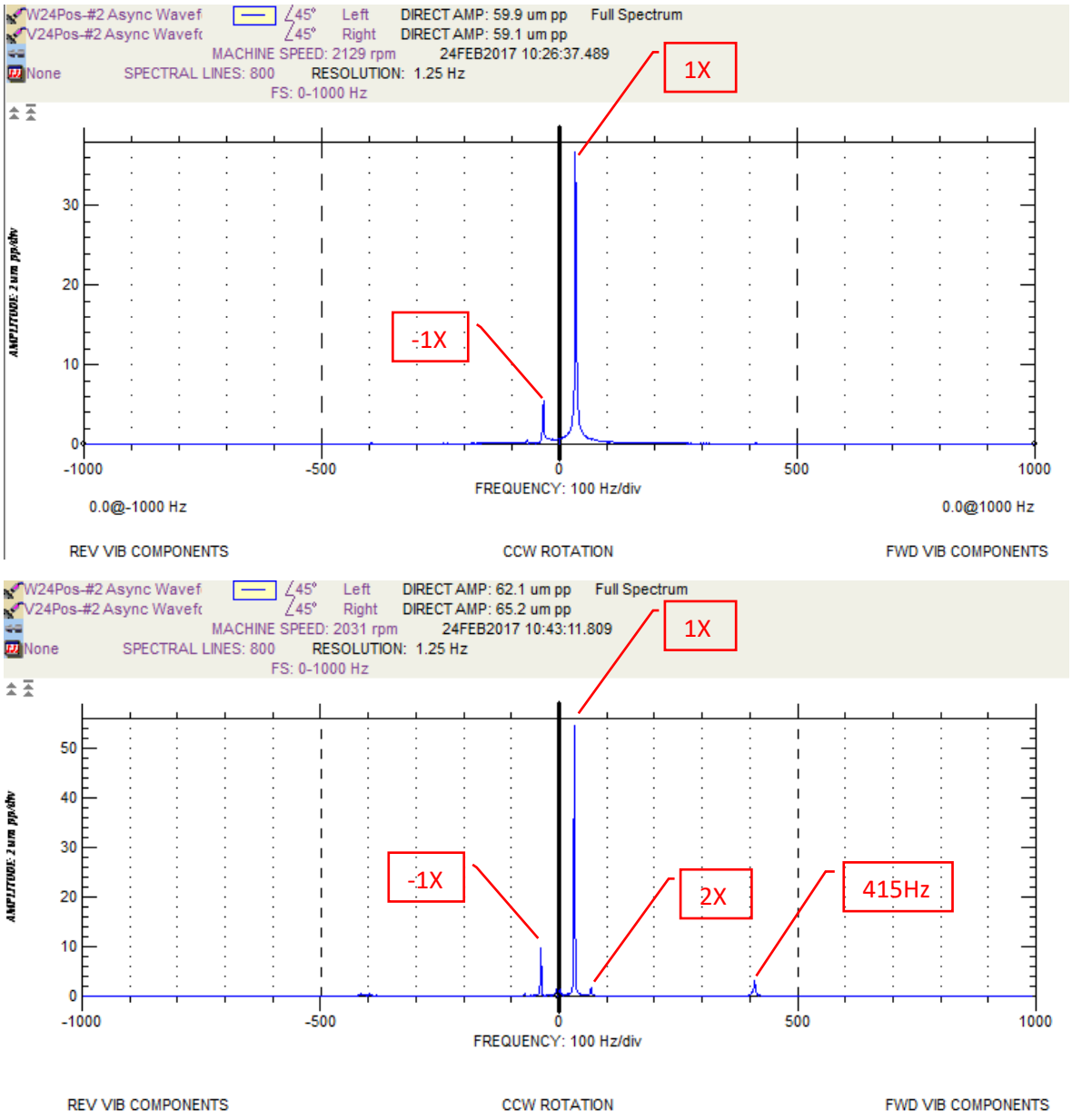

Figure 6-24: Spectrum plot for rotor at speed of 2130 rpm showing different component of vibration frequencies. Aligned (original run) top plot and misaligned run bottom plot.

In summary, the AMB has the advantage of providing bearing control currents which are related to force or the effort that the controller makes to keep the shaft in the centre of the bearing. These measurements, in addition to the shaft position and frequency of vibration, may be used to diagnose misalignment issues in an AMB supported rotor. Comparison of the uncoupled and coupled rotor current and position data provides information about shaft misalignment. In addition, existence of, or higher magnitude of 2X running speed frequency in the spectrum plots could be an indication of misalignment which can be cross validated with the bearing current values. These results may be

compared with the conditions existing when the equipment was running under acceptable alignment.

6.6 Balancing the Rotorkit

One of the common issues in rotating equipment is the state of balance of the rotor. The unbalance is the result of centre of gravity of the rotor not being located on the rotation axis of the rotor. It is normal to have some degree of unbalance on any rotor even during commissioning when the machine is new. This unbalance could be caused by manufacturing tolerances. As the equipment ages, deposits may accumulate on the impeller or erosion of the impeller that might cause the rotor to become unbalanced. The rotor can be balanced in the field by adding or removing mass at the balance plane(s) or, alternatively, by balancing on a high speed balancing machine. AMB supported rotors can modify the axis of rotation so that it passes through the centre of gravity of the rotor. However, the unbalance magnitude still should be within limits and the vibration caused by unbalance should not go above those limits. Digital control for unbalance compensation can be done by inserting a notch filter tuned around the rotating speed which makes the rotor rotates around its centre of gravity rather than centre of geometry. However, if the unbalance causes high levels of vibration, this cannot be done as the rotor will rub against the stator. In other words, the rotor control is “loosened” to allow the rotor to freely rotate about its centre of gravity rather than its geometric centre. This method is possible for only small corrections as the air gap is decreased. Therefore, it is important to balance the rotor to avoid these circumstances.

Field balancing of a rotor may be implemented by conventional methods mentioned by Bently (2003) and Muszynska (2005). This can be done by adding trial mass and measuring the effect of the mass at the running speed on vibration levels and phase. Consequently, the magnitude and phase of the balance mass (location on balance plane) can be calculated to reduce vibration levels at operating speeds.

The MBRotor-II has a flexible rotor that runs above first critical speed which is at 6500 rpm. The second critical frequency is at 24360 rpm which is well above the running speed. This indicates that at the running speed of 9000 rpm, the first mode is still the dominant mode of vibration. This is confirmed by polar plots of all four position sensors (Figure 6-27) showing similar phase and amplitude of vibration at running speed. This indicates the

running deformed shape of the rotor is similar to a half sinusoid. For balancing this mode, the best balance mass location is in the mid span on the balance disk provided. Moreover, the MBRotor-II has limited provision for adding balance masses in planes close to the AMBs. For more information on balancing, the reader is referred to Bently and Muszynska (D. E. Bently & Hatch, 2003) for different type of balancing.

It is worth noting that the location (phase) of any trial mass should be approximately defined by determining the angle of unbalance on the rotor (heavy spot). In case of lack of consideration, the trial mass might increase the vibration and causes the trip to activate if the rotor is already experiencing high level of vibration. This was noted on the MBRotor-II which had vibration levels more than 85 µm pp on different axes before balancing. If the wrong spot for the trial balance mass is chosen, the vibration levels can reach trip. As an example, adding a trial mass of 1.8 g in direction of V1 axis (0 degrees phase with respect to V13 axis) on the rotorkit at the disk shown in Figure 6-26 caused the vibration to reach over 120 µm pp at approximately speed of 2150 rpm as shown in Figure 6-25. In this case, the rotor had not reached steady state speed for measuring the effect of the trial weight mass and calculating the balance mass. It is important to note that in high efficiency industrial machines, the clearances are tight and high levels of vibration might cause the rotor to rub against the stator at tight clearance locations such as seals. This will reduce the asset's performance and might cause reliability issues in the long term.

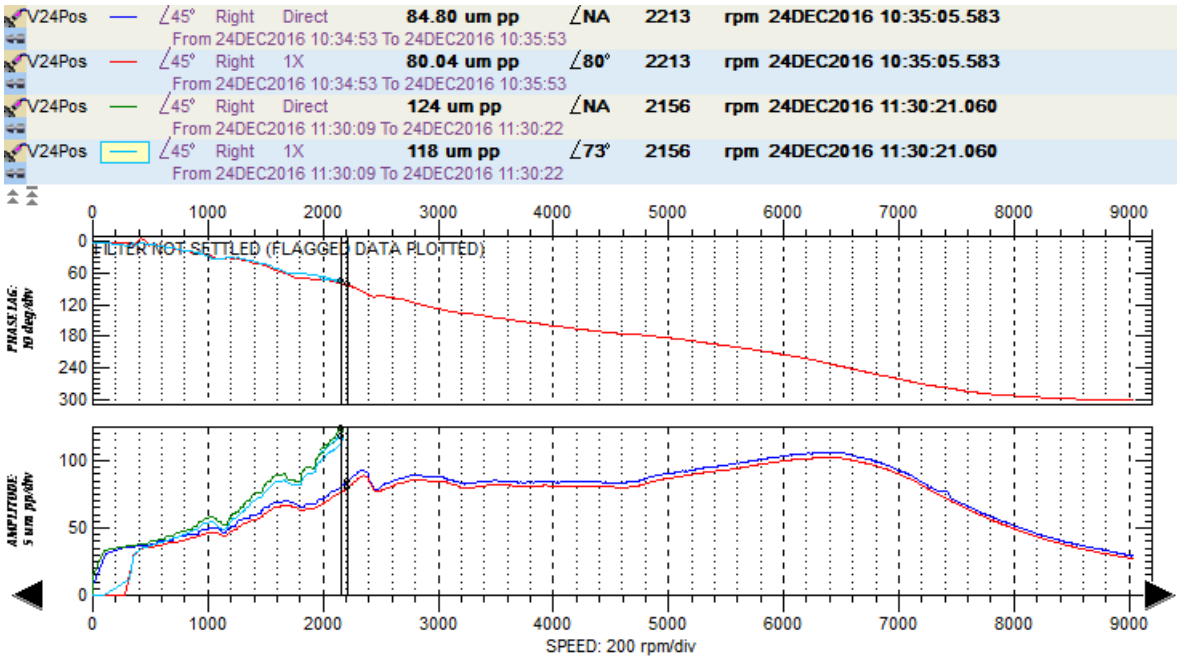

Figure 6-25: Vibration levels of V24 axis during normal run (blue/red) reaching 9000 rpm and with trial mass (green/cyan) reaching 2213 rpm with vibration level of 124 µm pp

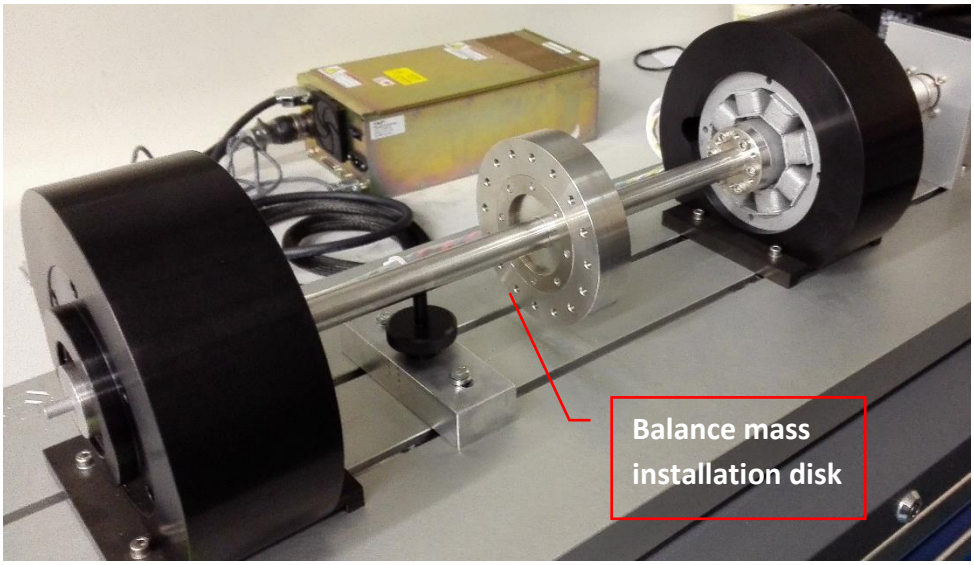

Figure 6-26: Provision for Balance weight installation on MBRotor-II

Figure 6-27 are polar plots displacement for different axes. The heavy spot (location of unbalance) can be identified by drawing a tangent line at low speed. The trial mass should be installed in the opposite direction to the vector drawn in Figure 6-27.

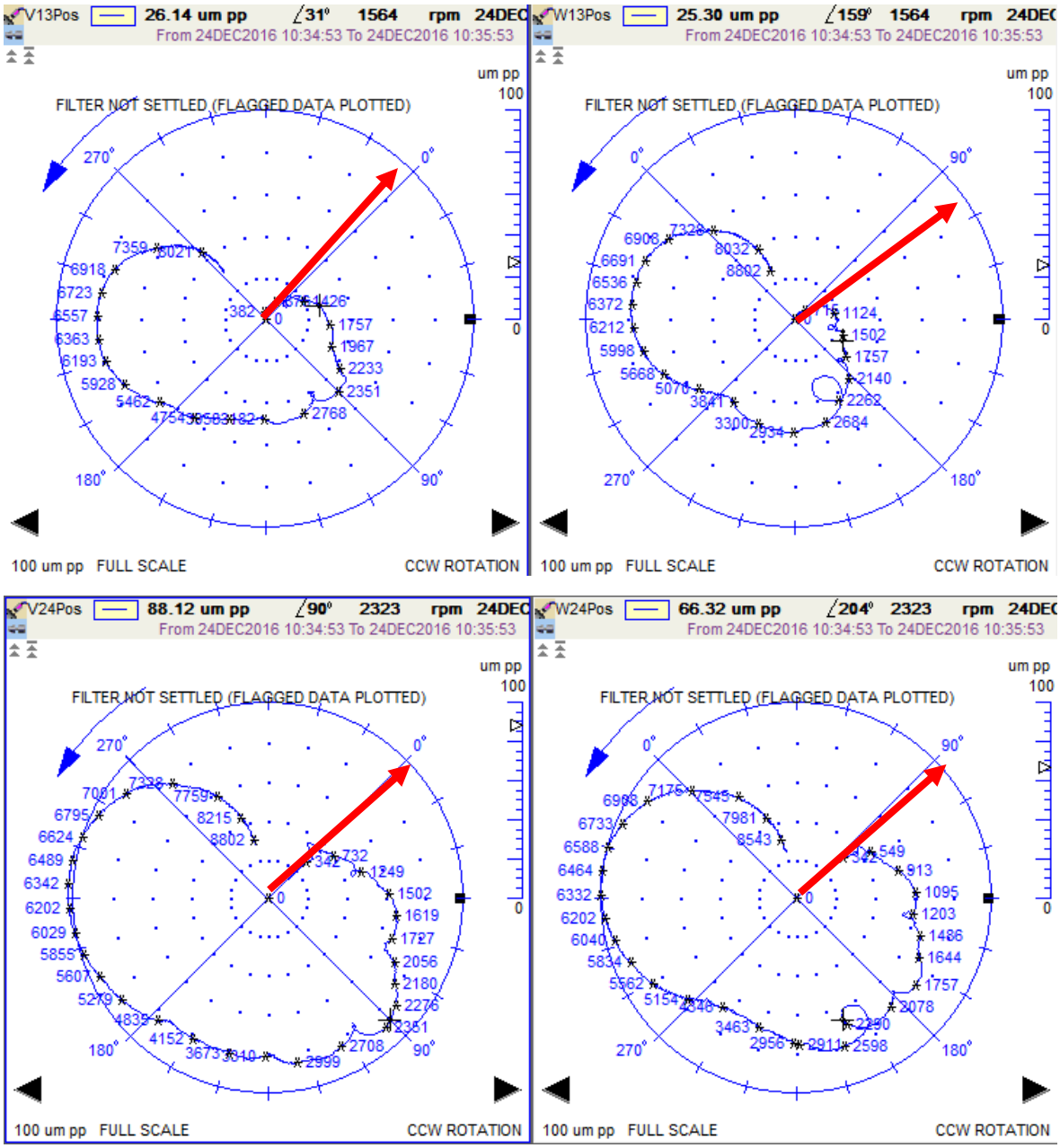

Figure 6-27: Polar plots for V13, W13, V24 and W24 indicating the location of the heavy spot.

Adding a trial balance mass of 1.82 g in the opposite direction of V13 axis reduced the vibration levels as shown in the polar plots of Figure 6-28.

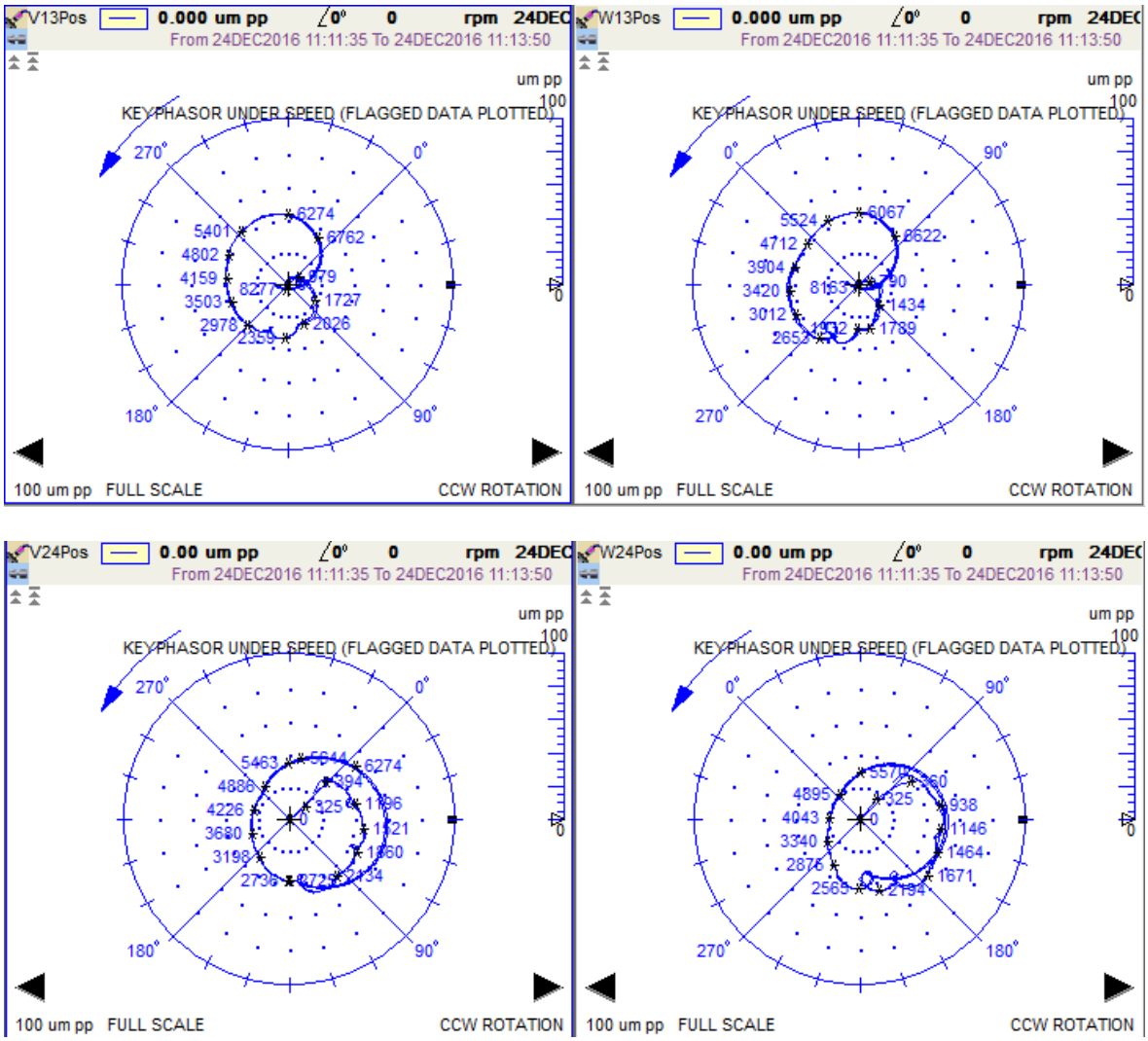

Figure 6-28: Polar plots for V13, W13, V24 and W24 indicating the effect of a 1.82 g trial mass in the opposite direction of the heavy spot.

Table 6-4: Unbalance response of MBRotor-II (No mass attached, trial mass attached)

Run Type	Axis	Speed (RPM)	1X Amplitude (um pp)	1X Phase (deg)
No attachements	V13	9000	29.5	273
	W13	9000	24	18
	V24	9000	27.3	302
	W24	9000	23.6	32
Trial weight	V13	9000	8	221
	W13	9000	7.5	327
	V24	9000	37.9	128
	W24	9000	32.4	220

The angle and mass for final balancing of the rotor can be extracted based on the equation (6-2) (D. E. Bently & Hatch, 2003) where all of the parameters are vectors at the operating speed.

$$\boldsymbol{m} = \frac{-\boldsymbol{O}}{\boldsymbol{T} - \boldsymbol{O}} \boldsymbol{m_{cal}} \tag{6-2}$$

$\boldsymbol{O}$ **:** Original response vector of the rotor without any attachment for each axis

$\boldsymbol{T}$ **:** Total response vector of the rotor after attaching the trial mass for each axis

$\boldsymbol{m_{cal}}$ **:** Vector of the trial balance mass for each axis. The angle is measured the opposite direction of rotation

The final angle and mass of the balance mass for different axes are shown in Table 6-5.

Table 6-5: Mass size and location for balancing the MBRotor-II at 9000 rpm

Axis	Speed (RPM)	Mass (g)	Angle (deg) *Reference: measurement axis
V13	9000	2.2	165.6
W13	9000	2.2	-106.8
V24	9000	0.8	176.5
W24	9000	0.8	-94.6

Another factor that needs to be considered in balancing the rotor is the balance mass should be attached to a point that compensates for unbalance response on all the axes. Where the balance mass is calculated for just one axis (location), it is possible to reduce the unbalance effect on that axis (location) while still having high unbalance vibration on the other axes (locations). The average of the mass and the location of the above calculation is a mass of 1.5 g at 170 degrees referenced to V13 axis (1.5 g$\angle$170°). The closest available screw-in mass was 1.8 g and the closest hole for the installation was 180 degrees from the V13 axis. The mass is coincidently the same as the trial mass on the rotor; however, it proves that the trial mass determined by the heavy spot was correct. Figure 6-29 compares the effect of adding the balance mass (cyan colour) to the original run (red colour).

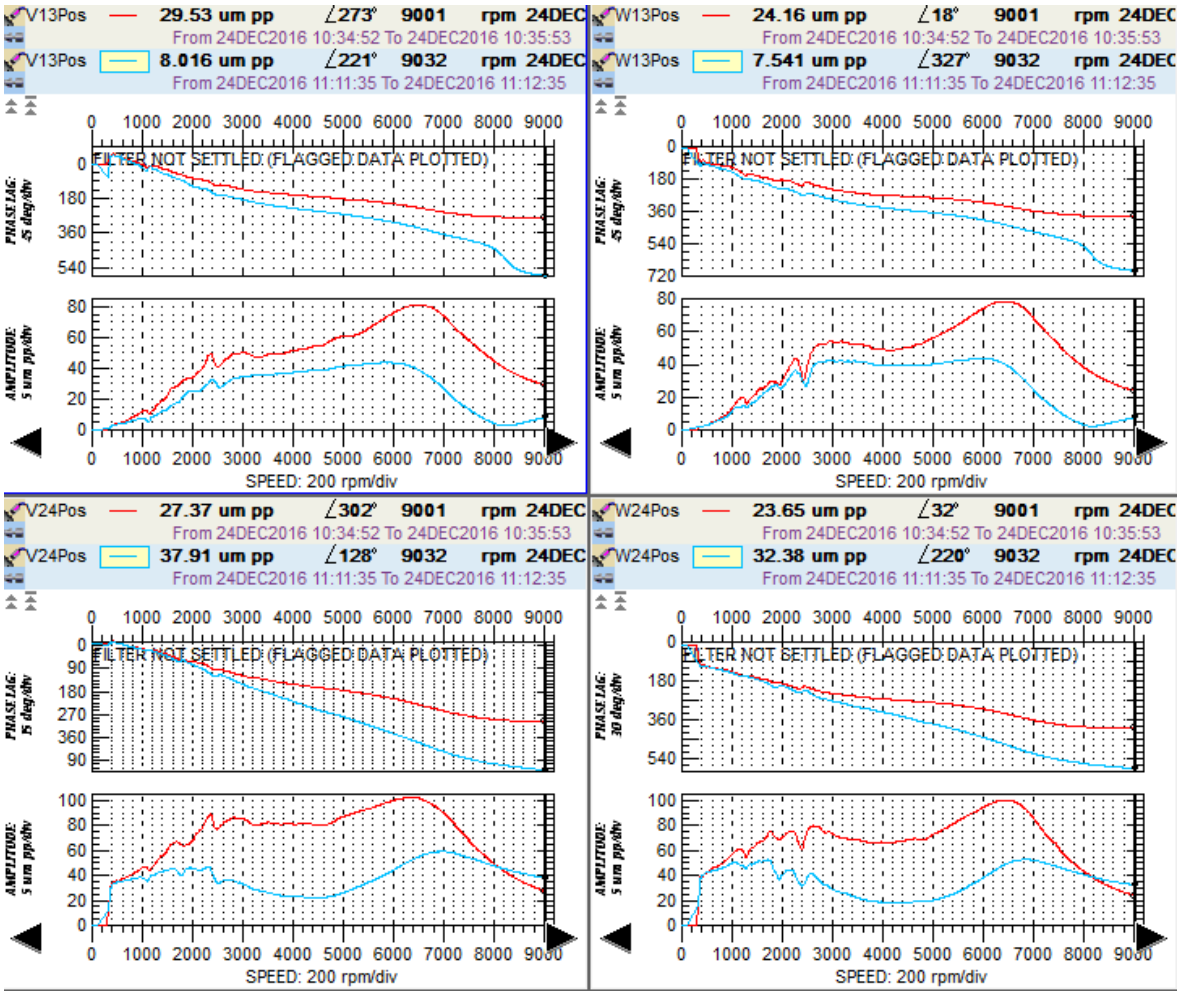

Figure 6-29: Unbalance response of the rotorkit original run (red) and after balancing for all axes (cyan)

Where the aim is to balance the rotor for lower vibration levels on the V13/W13 axes, a balance mass of 2.05 g was added at 157.5 degrees (closest available mass to the closest available balancing hole). This has resulted in lower vibration levels on axes V13/W13 (3.3 μm pp on V13 and 2.6 μm pp on W13) and higher vibration levels on axes V24/W24 (49 μm pp on V24 and 41.8 μm pp on W24).

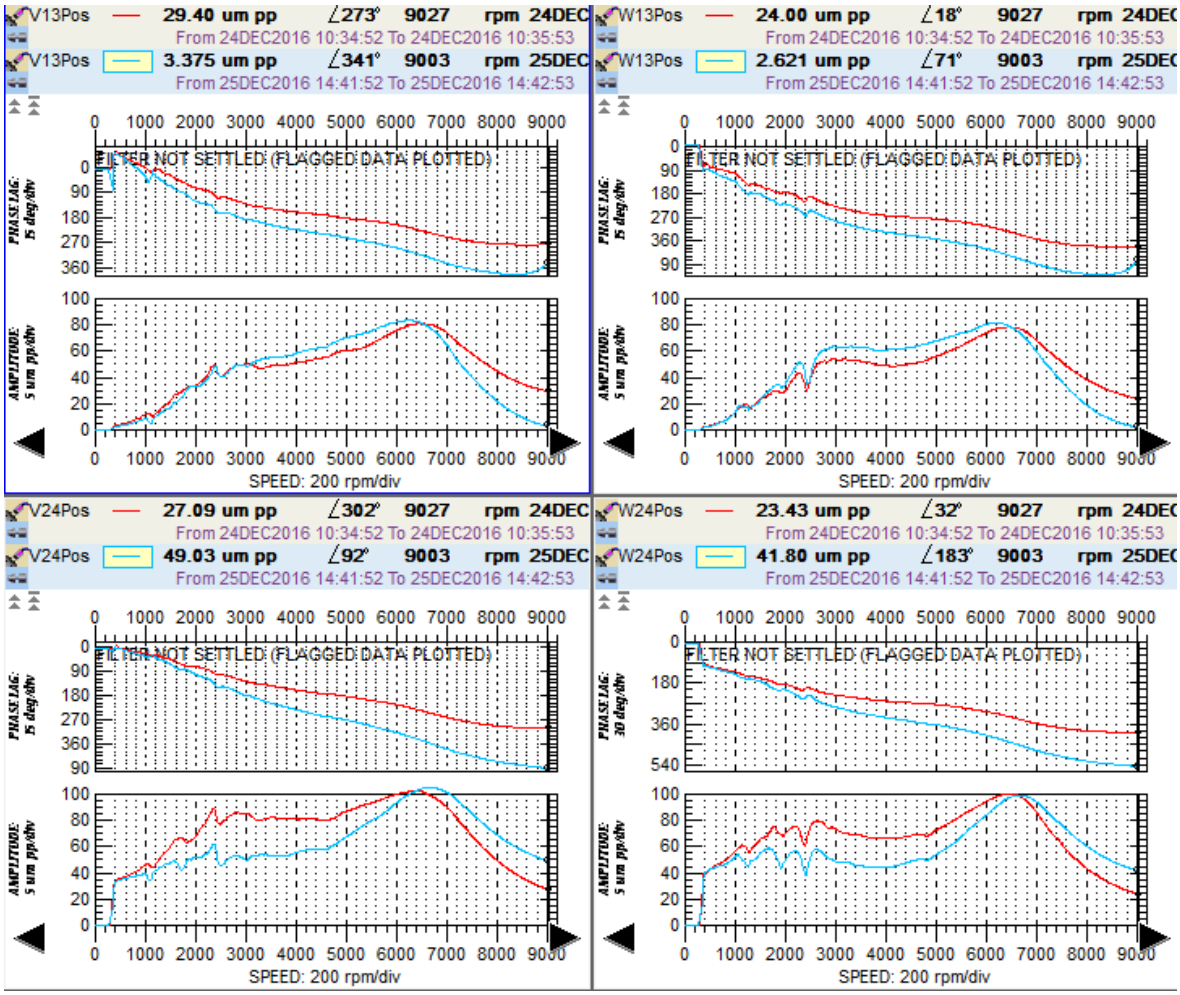

Figure 6-30: Unbalance response of the rotorkit original run (red) and after balancing for V13/W13 (cyan)

As mentioned earlier, the AMB controller can change the centre of rotation from the geometrical rotor axis to its centre of mass. This would reduce the unbalance response of the rotor to negligible values. Normally, this is done by implementing a notch filter tuned around the running speed. Figure 6-31 shows vibration orbits for the Drive End (DE) and the Non-Drive End (NDE) bearings. The vibration levels were reduced dramatically. Figure 6-32 shows the trend of vibration before and after the Automatic Vibration Control (AVC) was activated.

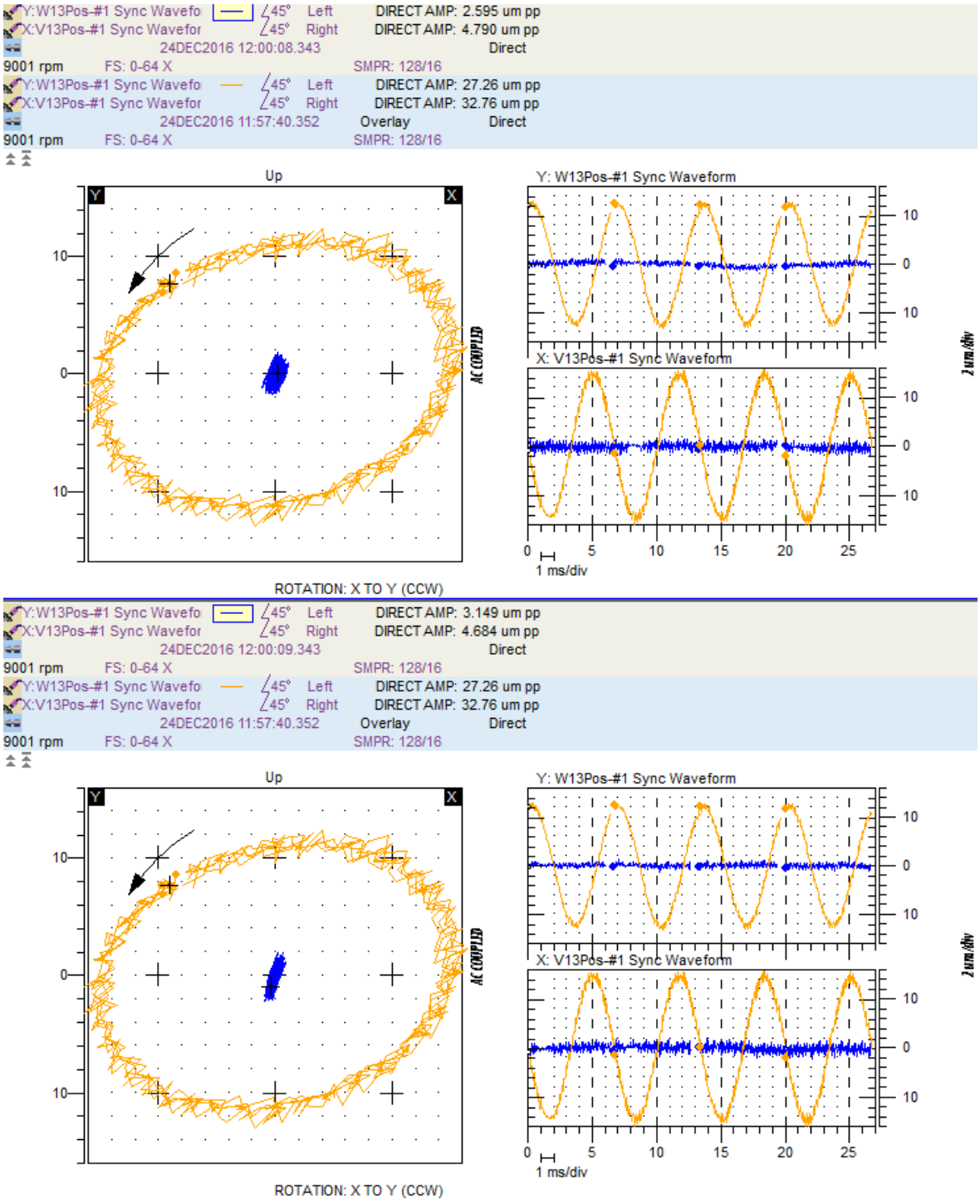

Figure 6-31: Vibration orbits for DE and NDE bearing before (orange) and after (blue) Automatic Vibration Control (AVC)

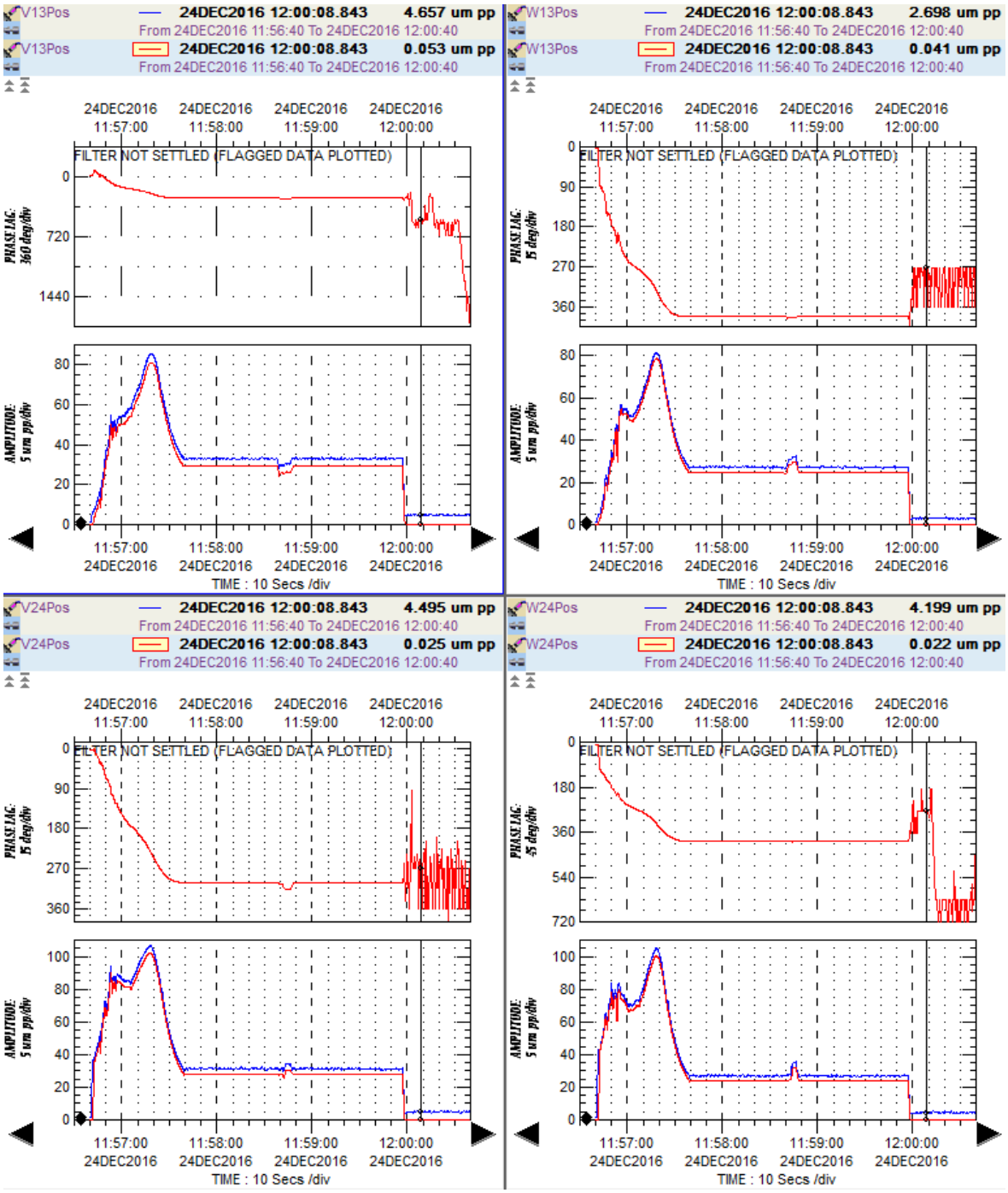

Figure 6-32: Vibration trends for vibration displacement sensors during the run up and after activation of AVC

6.7 Identifying Controller Issues

One of the important aspects of diagnostics of rotors supported by AMBs is to differentiate mechanical issues from controller issues. The majority of the mechanical failures can be identified by analysing vibration signatures. Most of the mechanical failures (which are imbalance and misalignment (Fluke, 2013) and (Agnieszka Muszynska, 2005)) are revealed

in the form of harmonics of running speed (e.g. 1X, 2X, etc.). One of the methods of identifying controller issues is to compare the model of the controller against criteria defined by the ISO standards (ISO14839-3, 2006). In case the AMB supported rotor model is not available or could not be extracted, one of the methods of identifying a controller issue is to inject excitation signals in the controller loop and assess the behaviour of the controller. The controller open loop and sensitivity can be assessed by the criteria proposed by ISO standard (ISO14839-3, 2006). These experiments for identifying controller issues can be implemented while the rotor is in the stand still position. The result of the experiment is compared against the original parameters, when the system was stable - where that data is available.

However, there are some occasions when the controller issues cannot be identified just by comparing the open loop response or sensitivity response of the system by the ISO method. The case study below provides information on how to diagnose controller issues through vibration analysis although it passes ISO standard requirements.

Section 5.7.4 described the generic 2nd order filters. Each axis can have up to four generic 2nd order filters. In this case study the 2nd order filter parameters for the V24 and W24 axes have been modified as per Table 6-6 from their original (stable) values to the modified values. The modified values caused the rotor to become unstable to the point that rotor came into contact with auxiliary bearing. Note that while rotor is rubbing against the auxiliary bearings, the controller continues to function (not switched off).

Table 6-6: Generic 2nd order filter on V24 and W24 modification. Original (stable) parameters vs. modified (unstable) parameters.

Filter number	Parameter	Original Value	Modified Value	Unit
$H_{tf,1}$	f_N	1500	415	Hz
	f_D	1000	415	Hz
	ζ_N	0.1	0.05	
	ζ_D	0.4	0.3	
$H_{tf,2}$	f_N	615	766	Hz
	f_D	615	766	Hz
	ζ_N	0.5	0.05	
	ζ_D	0.6	0.2	
$H_{tf,3}$	f_N	442	1170	Hz
	f_D	458	1170	Hz
	ζ_N	0.25	0.07	
	ζ_D	0.25	0.2	

The modified parameters reported in Table 6-6 were inserted in the model of the SKF rotorkit to create a revised model. The open loop and sensitivity transfer functions were compared with the original model and the original measured values (Figure 5-15). The results are shown in Figure 6-33 and Figure 6-34. As per the ISO guidelines, the peak sensitivity for the V24 and W24 axes, even for the modified values, are within zone A. The newly commissioned machines normally fall within peak sensitivity below 9.5 dB (3 abs).

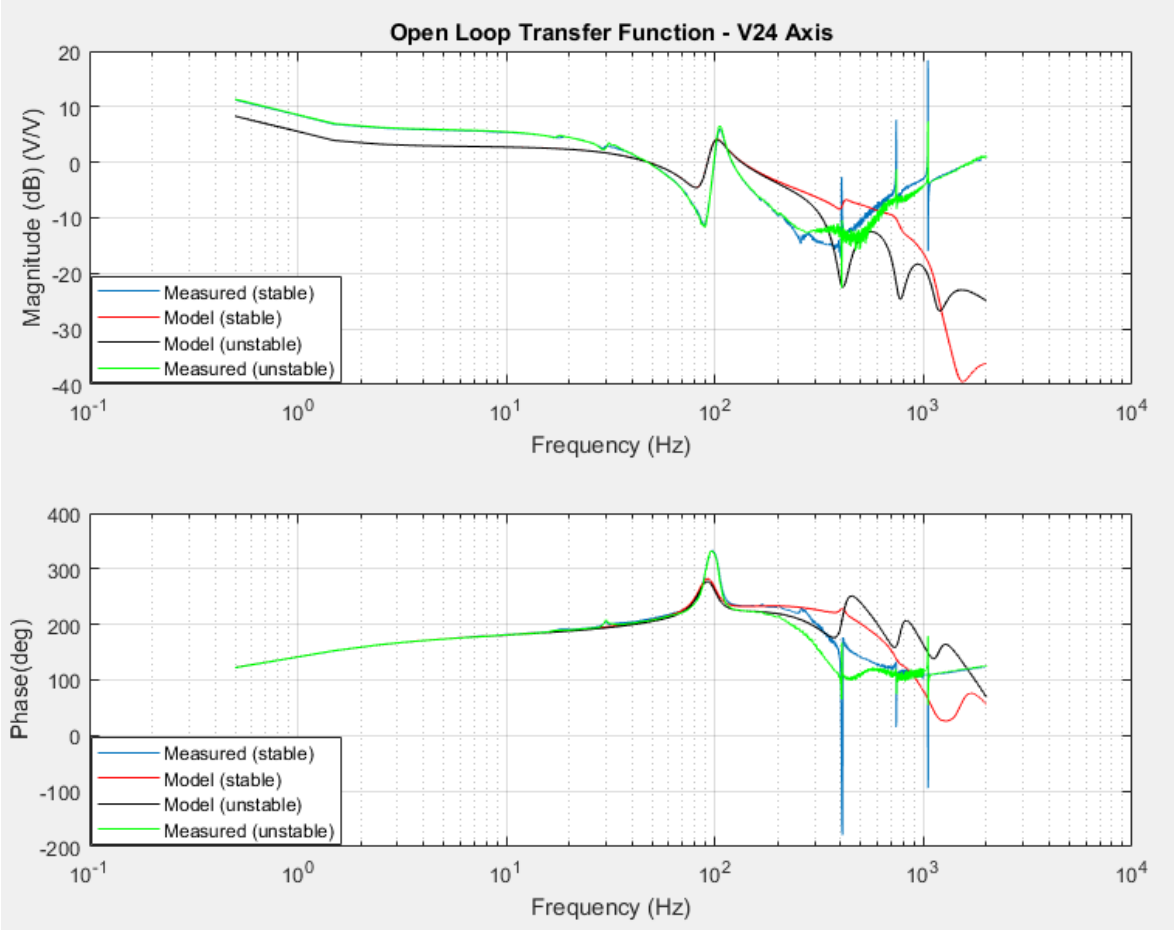

Figure 6-33: Open loop transfer function for original parameter of V24 and W24 compared against modified (unstable at around 8000 rpm above) values.

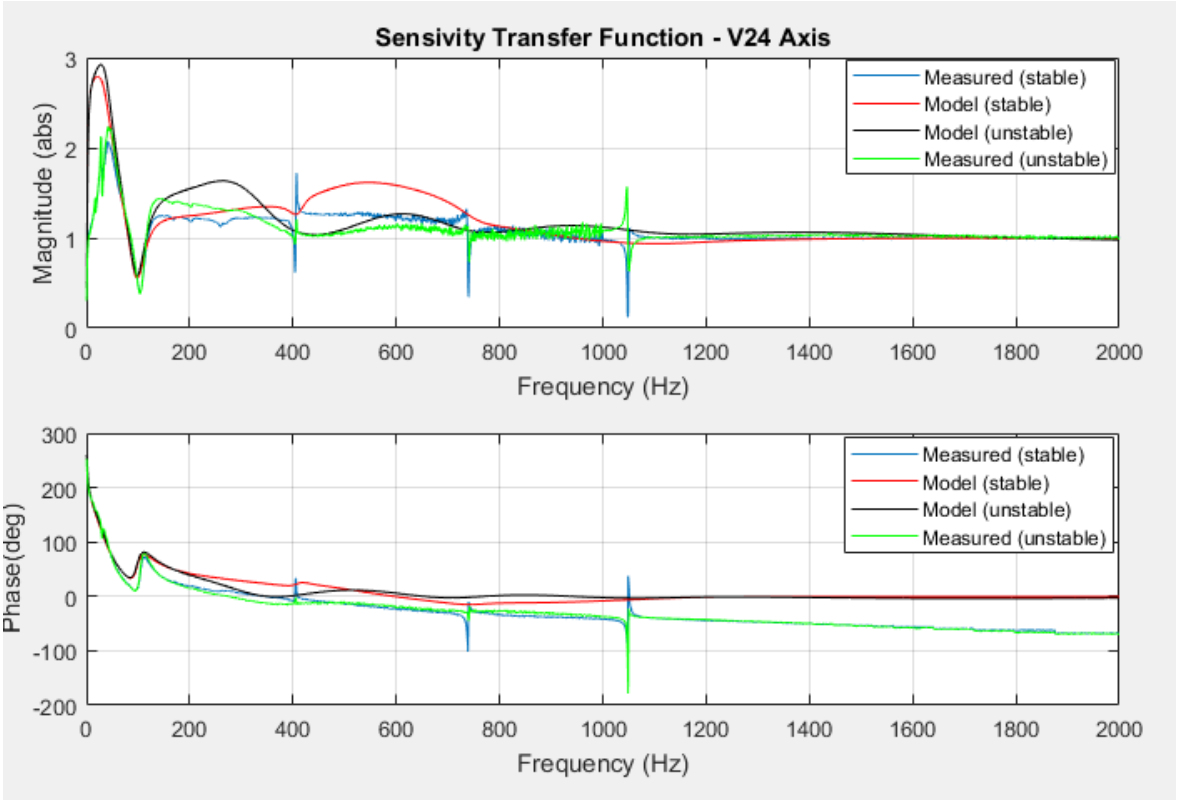

Figure 6-34: Sensitivity transfer function for original parameter of V24 and W24 axes compared against modified (unstable at around 8000 rpm above) values.

After implementing the above modified parameters, the rotorkit was driven up to its steady state speed of 9000 rpm. However, the rotorkit tripped because of high level vibration on the V24 and W24 axes at 8350 rpm. During coast down the vibration reached 355 µm pp on W24, which is almost the full clearance of auxiliary bearing (360 µm). This also indicates the rotor was rubbing against the auxiliary bearings. The 1X component stayed at low levels (50 µm pp) while direct vibration levels reached 355 µm pp. This indicates there were other vibration frequencies that contributed to the high level of vibration. Further analysis via the full spectrum plot, shown in Figure 6-36, and correlation with a Campbell plot, shown in Figure 6-13, indicates the second backward resonance of the rotor had been excited. Comparison of the orbit plots from the displacement sensors and bottom current sensors for the NDE bearing (V24-W24 axes), shown in Figure 6-37 and Figure 6-38, indicates the bearing current values reached its minimum. In other words, the bottom quadrants of the AMB magnets did not provide sufficient current to control the shaft movement because it reached its minimum level of current. Note that the signs of rubbing in this case differ from those for a partial rub. The rotor is experiencing full annular rub which is rubbing around the auxiliary bearing. It is also different from a complete rotor drop as the controller is still

trying to hold the rotor by providing current to the AMBs. Figure 6-35 shows that after MBRotor-II tripped during coast down, the controller regained control of the rotor.

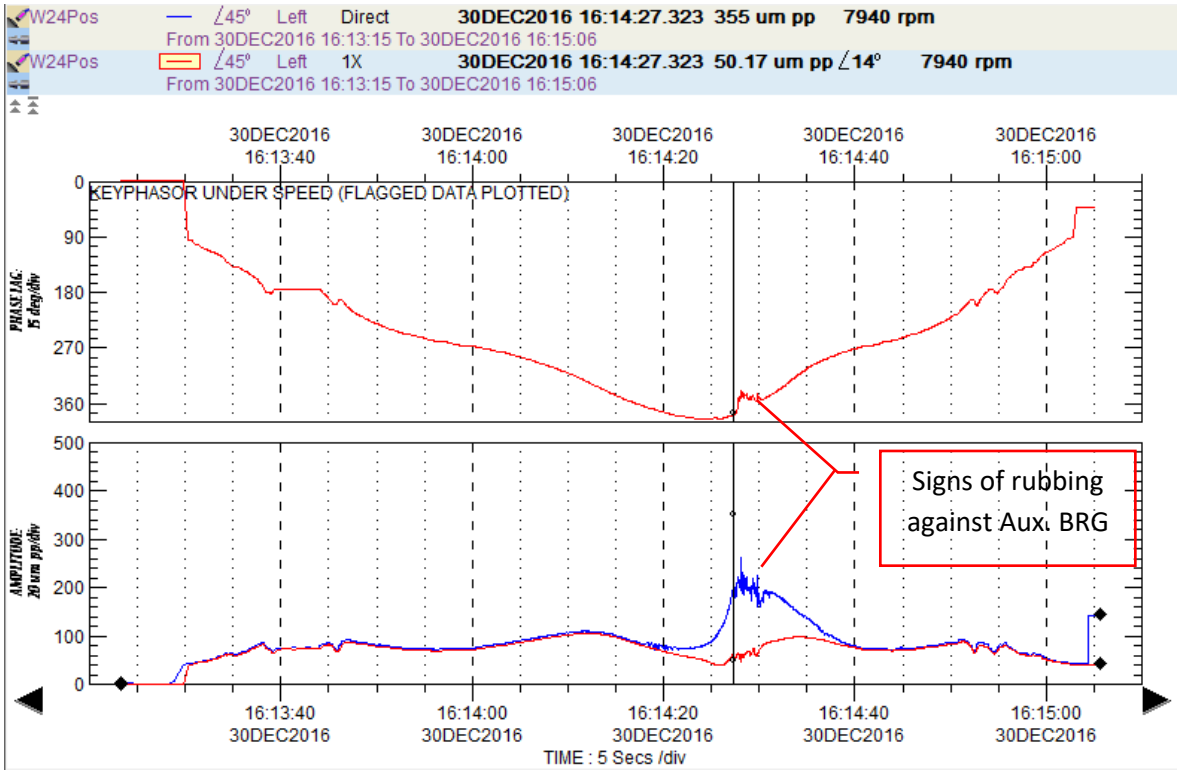

Figure 6-35: W24 vibration trend with modified parameters. The rotorkit tripped approximately at 8350 rpm due to high level of vibration

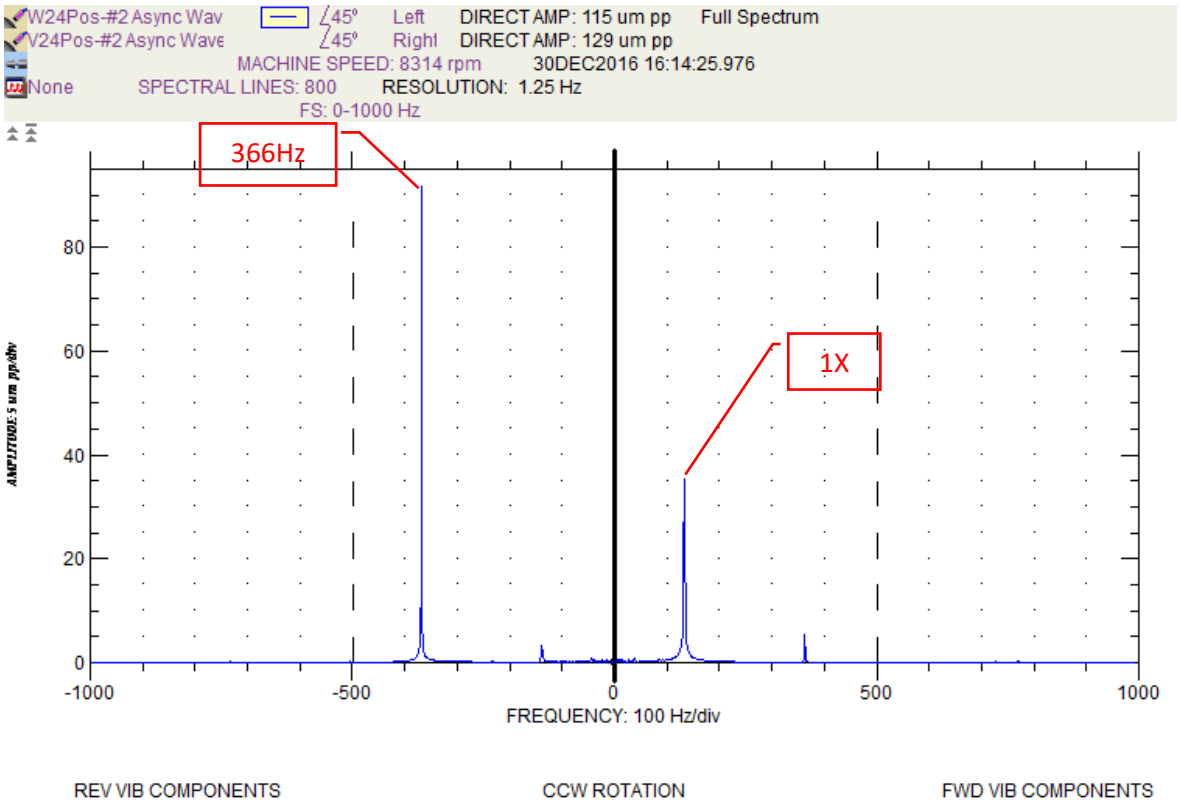

Figure 6-36: Full spectrum plot of V24-W24 axes when the rotor has reached 8314 rpm.

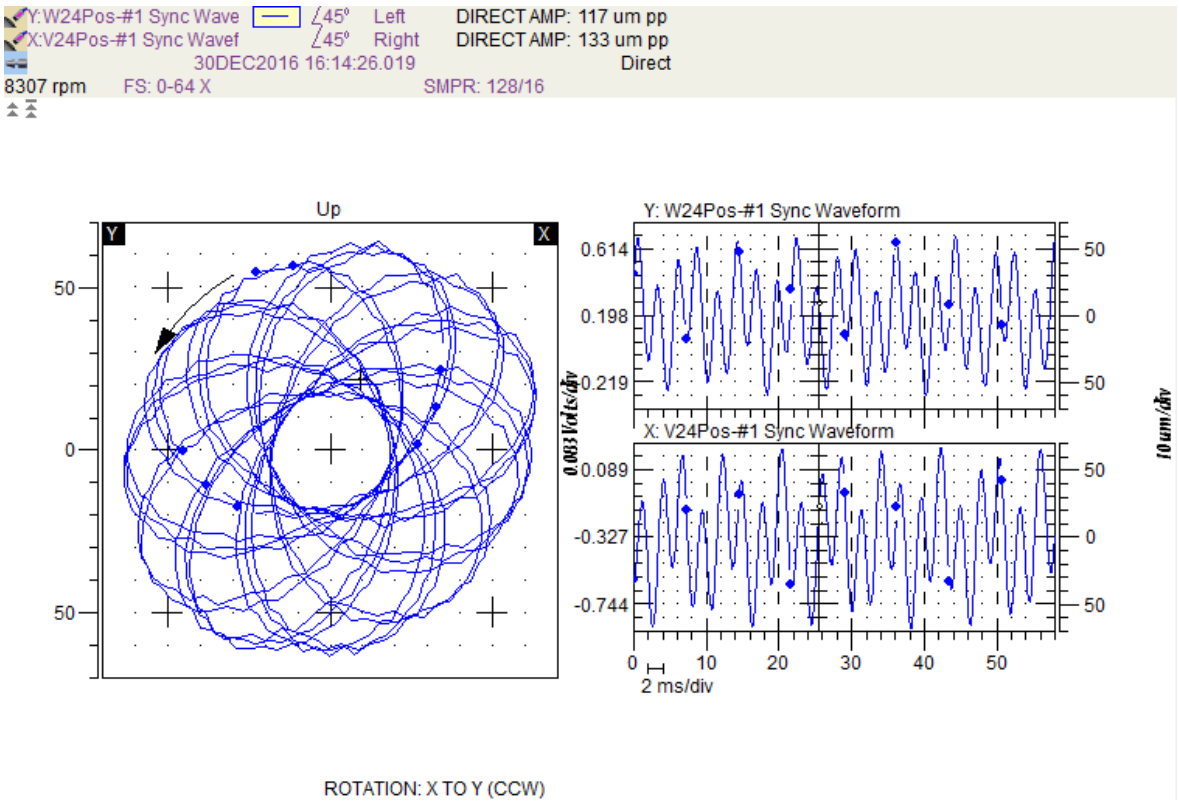

Figure 6-37: Orbit plot of V24-W24 axes (NDE Bearing) showing major frequency component to be non-1X

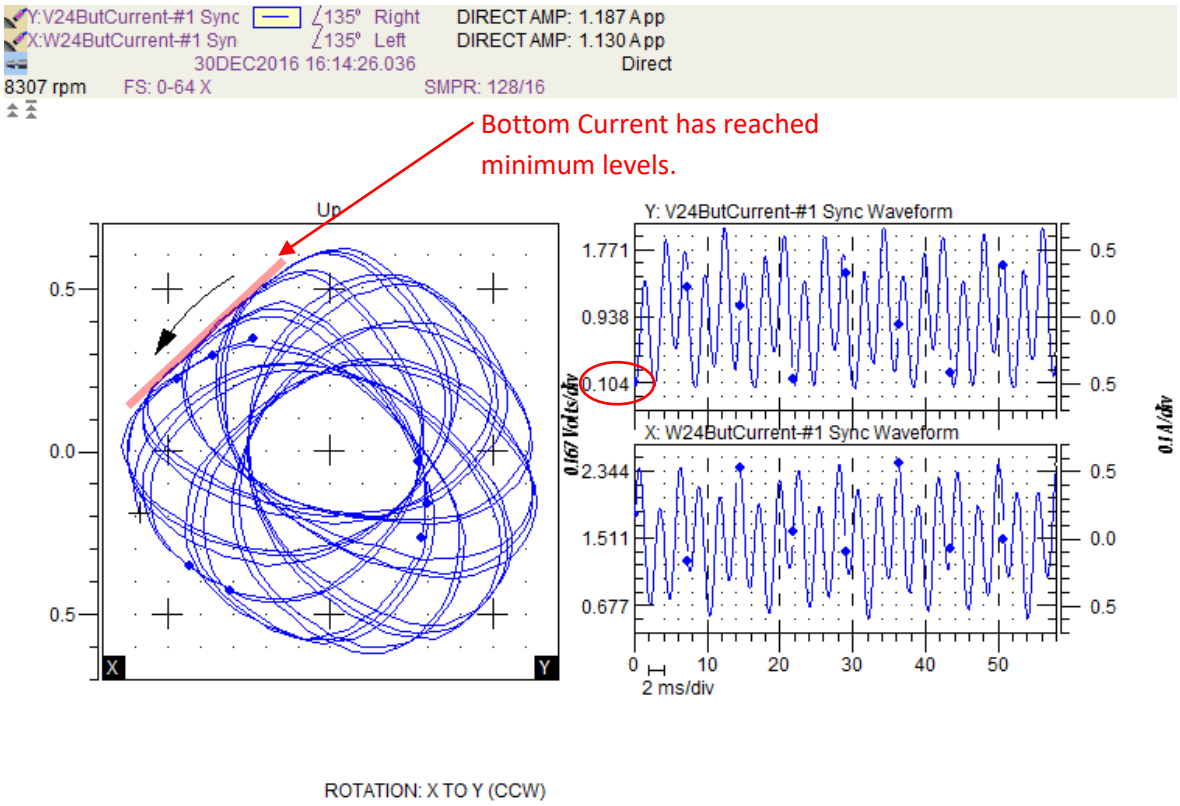

Figure 6-38: Bottom current orbit for V24-W24 axes. Current level reached its minimum level of 0.1A

As explained in section 5.9, API617 (2014) recommends Level II analysis be implemented and compared with the acceptance criteria. For this purpose the logarithmic decrement was compared against the acceptance criteria. Based on this guideline, critical modes up to twice maximum continuous speed should be considered in the evaluation. The maximum recommended continuous speed for the MBRotor-II is 9000 rpm (150 Hz). Therefore, all of the modes up to 300 Hz should be considered. Considering the previous analysis, only the first critical speed of the rotor needs to be considered in this analysis which falls below the maximum continuous running speed N_{mc}.

The logarithmic decrement δ can be extracted based on equation (6-3) (Inman, 2017):

$$\delta = \frac{2\pi\zeta}{\sqrt{1-\zeta^2}} \tag{6-3}$$

ζ: damping ratio at the mode (can be extracted by MATLAB for each mode)

δ: logarithmic decrement

The logarithmic decrement value for the first mode of the rotor is provided in Table 6-7. The acceptance criterion for the modes below maximum continuous running speed is to have a logarithmic decrement above 0.1. As indicated in Table 6-7, the MBRotor-II passes this criterion, even with modified values.

Table 6-7: Logarithmic decrement values for original and modified values of the 2nd Generic filter

	Original Setting	Modified Setting
1st mode Logarithmic Decrement	1.73	1.86

Figure 6-39 shows the open loop Bode plot of the V24 axis for normal parameters compared to the modified parameters. The stability margins are indicated on the plot. The modified values have caused the phase reach 180 degrees around 350 Hz to 370 Hz (red ellipse in the figure). Although, the gain margin is approximately 14 dB, it does not provide enough damping to the closed loop system. As mentioned earlier, not all of the natural frequencies could be damped by gain compensation (as the example of provided modified parameters). The original parameters dampen the natural frequency in this range by phase compensation.

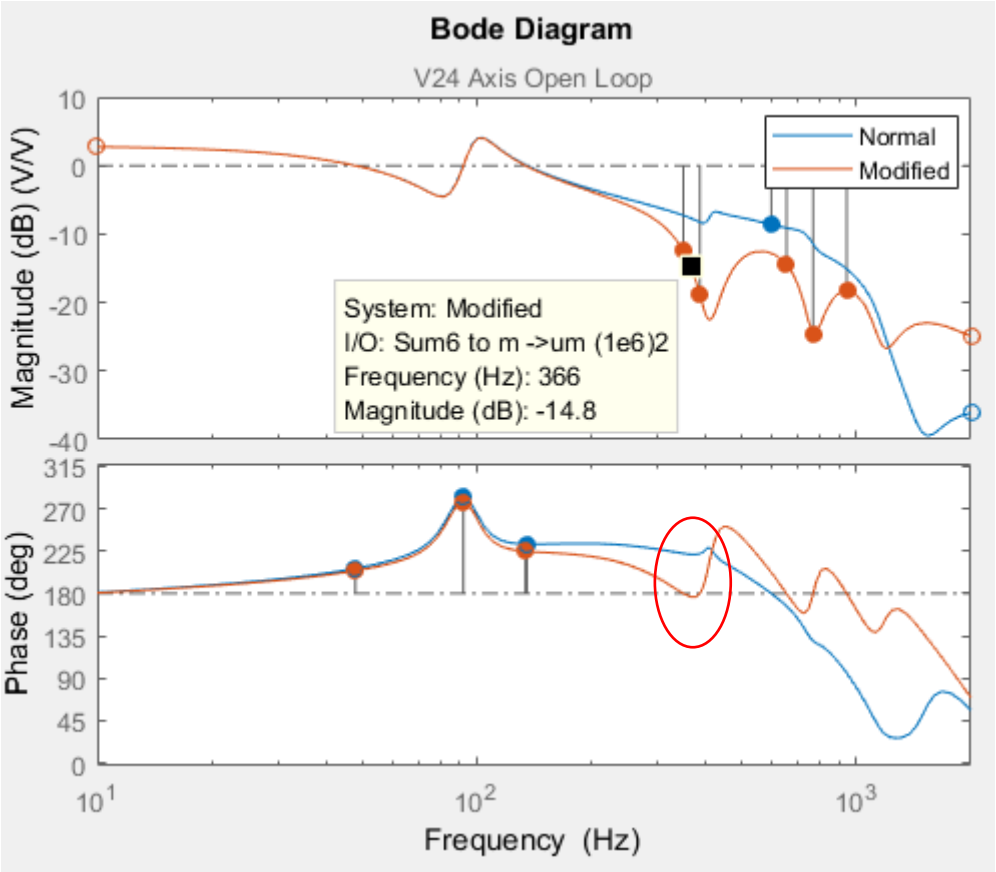

Figure 6-39: Bode plot of V24 axis showing stability margins

As stated in section 5.7.4, the generic 2nd order filters are used to reduce the effects of resonances outside the operating speed range of the equipment. Non-optimal filter values might result in lower damping of the resonance which might lead to high levels of vibration, as demonstrated in this section. Although the modified filter setting parameters passed the criteria defined by the industrial standards, the rotorkit was unstable as it reached the frequencies where there is not enough phase to damp the natural frequencies. The industrial standards should consider other criteria and plots such as phase in Bode plots or root locus for providing additional measures to ensure the rotor system has enough stability in its operating region.

6.8 Defects Summary Sheet

Table 6-8 provides a summary of the experimental defects implemented on MBRotor-II. This summary sheet provides high level information on the defects observed in these specific experiments. This table should not be generalised on other rotating equipment in

industry or if the configuration of the MBRotor-II is modified either mechanically or in relation to its controller settings.

Table 6-8: Summary of experimental defects implemented on MBRotor-II

Defects/ Symptoms	1X	1X Phase	2X	Super Harmonics	Subharmonics	Gap Voltage	Average Current	Overall Vibration
Partial Hard Rub	Minimal changes (No hot spot)	Minimal changes (No hot spot)	NA	Excitation of higher resonance (377 Hz Backward mode)	0.5X (Hard Rub) 1/3X, 1/4X, etc. Soft Rub	Changes	Current changes to adjust to shaft position	Evident while rubbing
Misalignment	Might changes as support stiffness changes		Evident 2X peak in Spectrum	2X in MBRotor-II with flexible coupling; Might excite higher superharmonics or rotor resonances	Not Observed	No changes observed in average gap voltage at stand still as coupling is very flexible	Changes in average current values at stand still because of controller effort to keep the shaft in bearing centre	Changes as a result of higher 2X
Unbalance	Evident changes	Evident Changes	Not Observed	NA if no other secondary effect	NA if not other secondary effect	Not Observed	Higher instant current to keep the rotor in bearing centre	Changes based on unbalance magnitude and phase
Controller Issues	Controller issues might excite mechanical symptoms; therefore, each case should be studied carefully.							

6.9 Critique

In this chapter, several defects were simulated on MBRotor-II. However, the rotorkit has some limitation on creating other type of defects. One of the main application of AMBs in industry is in turbo-expanders. Turbo expanders can face fluid ingestion in form of liquid (process fluid e.g. LNG). This might cause fluid instability issues on the rotor system. This phenomena could not be simulated on rotorkit because of its limitation. Moreover, additional improper controller settings could be studied further.

6.10 Summary

In this chapter, different failure modes that could affect AMB supported rotors were simulated on the rotorkit MBRotor-II. The patterns of the failures were studied by measuring the data captured through position and current sensors. Different parameters such as vibration and current were captured in high resolution through an external DAQ (Confidential vendor-supplied data removed from this publically accessible electronic copy.). Most of the mechanical failures excite the resonance of the rotor, the details of which were extracted through the FEA model for that specific speed. Of course there were minor differences which are related to modelling and simulation inaccuracies or simplification of the model such as neglecting the stiffness of the support.

One of the best methods of diagnosing a problem is to compare the difference between the normal (healthy) run with a run with a defect present. For this purpose, and for future reference, a base line should be captured while the rotor is in its healthy condition.

During the rubbing simulation of the rotor, the impact that was caused by the stationary component excited both forward and reverse (backward) second resonances of the rotor. This was observed by investigating full spectrum plots.

The misalignment of the rotor through the flexible coupling indicated twice running speed (2X) frequency excitation which is a well-known pattern for misaligned rotors. In AMB supported bearings, the misalignment could be identified by comparing the currents in the AMB for the coupled and uncoupled rotor. Misalignment put additional forces on the bearing even during stand still conditions. It should be noted in industrial equipment that thermal gradients and growth might cause misalignment between cold and hot conditions of the machine. These factors need to be considered while aligning the rotors.

Unbalance by its nature shows itself at the frequency of shaft rotation. While low level unbalance is acceptable on rotating machinery, high levels of unbalance should be tackled by adding or removing mass from the rotor. The MBRotor-II shaft was balanced through conventional methods. However, it was proved that in order to have a better balanced condition all the sensors should be considered in balancing. It is possible to reduce the unbalance effect on one side of the rotor while worsening the condition of the unbalance on the other side of the rotor. All these factors should be considered while balancing. One advantage of AMB supported rotors is that the rotor can be controlled to rotate around its centre of mass rather than centre of geometry. This will lead to minimal levels of unbalance of the rotor while running.

Finally, the controller parameters play an important role in the vibration of the rotor. If there are frequencies not related to the rotor running speed or rotor resonances, it is probably related to controller faults. Some of the controller deficiencies show themselves to have symptoms similar to those of mechanical defects. A good example is the deficiencies in damping the rotor resonances above operating speeds. If the filters do not damp these resonances, the defect might show itself as an excitation of the resonance. Therefore, care should be taken while dealing with controller issues. One suitable method of dealing with controller issues is to inject sweep signals across all frequencies based on the ISO standard and excite all resonances of the rotor, especially during stand still condition. If the controller does not damp the resonances, the injected signal will cause high level vibration at that specific frequency.

Chapter 7

Summary, Conclusion and Future Work

7.1 Summary

This thesis presented modelling, simulation and diagnostics of rotating equipment supported by AMBs.

Chapter 3 provided a summary of the capabilities of the test rig. The test rig under study and experiment was an SKF MBRotor-II supported with an MB340g4-ERX controller. The MB340g4-ERX controller is an industrial controller that is used for industrial turbo-molecular AMB supported pumps. The MB340g4-ERX has MBScope software which provides the means of changing the configuration, implementing calibration and capturing basic data. The MB340g4-ERX controller has four SISO PID (one per radial axis) compensators complemented with Lead-Lag, low pass and 2nd order generic filters or notch filters to levitate the rotor and dampen the resonances below and above operating speed. The MB340g4-ERX controller also provides buffered output for connection to an external data acquisition systems.

In this Chapter 4, the MBRotor-II rotordynamics was modelled with FEA methods. The industrial guidelines, such as API, were considered in the FEA modelling of the rotor. The model was converted to a state space model with the AMB bearing forces and unbalance forces (optional) as inputs, and the displacement sensor locations as output. The state space model had 4x6x616 states. The eigenvalues of the model were compared with vendor-provided data sheets and it showed coincidence with lower than 2% deviation. Since displacement sensors are non-collocated with AMB actuators, the mode shape of the rotor was studied to ensure there was no node between the sensors and the AMB actuators. As the FEA model had a high number of DOFs, the state space model was reduced to 4x6X36 DOFs, ensuring the reduced model has a good coincidence up to 10 kHz frequency.

In Chapter 5, all of the electrical and controller transfer functions (including magnetic bearing, power amplifier, displacement sensors, controller time delay, zero order hold for digital signal processing, PID compensators and all the filters –lead lag, 2nd order generic filters and low pass filter) were extracted. All of the electrical and controller transfer functions were integrated with the MBRotor-II state space model derived in Chapter 4. The open loop and sensitivity transfer functions (defined based on industry standards) were extracted. The results were verified by experimental results which were extracted by

injecting a Sweep Sine waveform and measuring the transfer function (System Identification methods). The theoretical open loop transfer functions provided good coincidence with the experimental results.

Diagnostics and troubleshooting of MBRotor-II were investigated in detail in Chapter 6. An external data acquisition system was connected to the MBResearch buffered outputs for capturing synchronous high resolution data (AMB currents and displacement sensors). For a comprehensive diagnostics and troubleshooting approach, modelling and simulation data from the previous chapters, combined with measured data, was applied. The best method of finding anomalies in rotating equipment is to compare the faulty condition with the machine running normally. Therefore, baseline data was captured as an indication of the normal condition. Different defects which were possible to create on the rotorkit were studied experimentally and the patterns were analysed.

In the case of the hard rubbing simulation, the rotor impact on the stator and its bouncing back excited both forward and reverse critical frequencies. This was validated by considering the Campbell plot of theoretical model which indicated the critical frequency of the rotor at specific rotating speeds. Other subharmonic frequency components were also excited which was observed in the full spectrum and waterfall plots. The orbit plot shows the deviation of rotor excursions as a result of impact with the stator. The instantaneous shaft centre line plot shows deviation of the rotor from the bearing centre. In this experiment the rub did not have influence on the state of balance; however, in industrial applications the rubbing can cause a hot spot on the rotor causing local bend which shows itself in changes in the 1X and 1X phase.

In the misalignment experiment, the rotor was intentionally misaligned with the motor. The best method of detecting misalignment between two casings is to compare the AMB current values under the coupled and uncoupled conditions. If the rotor is misaligned the controller makes more effort to keep the rotor in the centre of the bearing. In the case of flexible couplings, comparing the coupled and uncoupled conditions at stand still shows the rotor position changes to be minimal (the rotorkit has a flexible coupling). However average current values would be different. In the case of rigid couplings, comparing coupled and uncoupled conditions, the average rotor position will differ along with the AMB current. During the running condition, misalignment causes the excitation of 2X components.

The rotorkit balance condition was improved by applying conventional balancing methods. The phase components (on position sensors) showed the mode that is excited is the first bending mode of the rotor. Therefore, the rotor balance condition was improved by installing mass on the balance plane which is on the disk mounted in the mid span of the rotor. Finally, it was demonstrated that by activating AVC, which acts like a notch filter makes the rotor rotates around its mass centre rather than geometric centre, reducing the amount of vibration on the rotor.

The controller issues could be identified by measurement of the vibration signal, current signal and by injecting sweep sine waveforms to identify the open loop transfer functions. The configuration of the 2nd order generic filters was modified intentionally for this study. The modified configuration passed the requirements of ISO14839-3 (2006) and the stability criteria of API617 (2014). However, the current signal measurement reached the minimum possible values when the shaft vibration reached the point that the rotor came into contact with the auxiliary bearing at the non-drive end. The model and the measured data showed the phase to be below 180°, showing insufficient damping of the rotor, making the system experiencing high level of vibration.

7.2 Conclusion

This research extracted the normal characteristics of the rotorkit to validate the model with vendor provided datasheet and also to compare the equipment performance against industrial standards. In addition, other rotorkit characteristics that is not possible to extract in the operating field through sensors measurement and help in diagnostics of the machine were extracted. These are properties such as reverse and forward frequencies at different speed in form of Campbell plot.

This research took a comprehensive approach in diagnostics of rotating equipment supported by AMBs through integration of model data and sensor data where minimal research was implemented in this field.

This research demonstrated advanced pattern recognition methods combined with theoretical model for solving most common AMB supported rotating equipment failure modes including mechanical and controller faults. In order to implement effective inclusive diagnostics, design data with all sensor measured data such as AMB current measurements

which are as important as vibration displacement data were considered. These sensor data was processed further to extract meaningful plots such as Bode, Polar, Shaft Centre Line and full spectrum waterfalls for the defective shaft.

This research provided the fundamental knowledge on how AMB supported rotating equipment work, and provided essential knowledge on diagnosing this type of equipment in the field through pattern recognition methods with the aim of covering the gap and lack of knowledge that exists in the operating field to solve AMB supported rotating equipment failure modes.

In order to implement effective inclusive diagnostics, all design, modelling and simulation data was integrated with the sensor measured data. AMB current measurements which are as important as vibration displacement data has been considered. These sensor data was processed further to extract meaningful plots such as Bode, Polar, Shaft Centre Line and full spectrum waterfalls for the defective shaft. This thesis undertook a comprehensive integrated approach to diagnose the issues in rotating equipment supported by AMBs where little research in this field was done previously.

7.3 Future Work

The following research could be carried out as a continuation of this thesis:

- The work could be extended by diagnostics of fluid instability phenomena which is frequently happens in the field as a result of liquid carry over to the machine. This is a common failure mode especially in turbo-expanders which using AMBs is a normal practice. These defects could be simulated theoretically and the results could be compared with the experimental setup. By installing additional modules on the test rig this phenomenon could be validated. In addition, the controller setting could be optimised to tackle this issue if it occurs.
- Section 6.4 addressed rubbing the rotor against a hard stator material (hard Teflon plastic). This research could be extended for rubbing against soft materials by manufacturing a rubbing stand made of softer material and study the behaviour of rotor against soft stator material.

- The MBRotor-II has the capability of being connected to an external independent controller. In addition, the MBScope-Analyzer provides misleading results above 300 Hz when injecting signals. A new more flexible controller could be designed and manufactured where it can implement new controlling algorithms such as non-linear control, H_∞ or MIMO where has the capability to inject signals and measure the output.
- The experiments in this thesis were implemented on a laboratory test rig. This research could be extended to industrial plant application.
- Newkirk phenomena (thermal unbalance caused by rub) could be simulated using the theoretical models and compared with experimental data by setting up additional components on the test rig.
- Different failure modes could be simulated theoretically and the result could be compared with the patterns found in the measured sensor data.

References

Abuzaid, M. A., Eleshaky, M. E., & Zedan, M. G. (2009). Effect of partial rotor-to-stator rub on shaft vibration. *Journal of Mechanical Science and Technology, 23*(1), 170-182.

Aenis, M., Knopf, E., & Nordmann, R. (2002). Active magnetic bearings for the identification and fault diagnosis in turbomachinery. *Mechatronics, 12*(8), 1011-1021.

Alves, P. (1998). *Magnetic Bearings-A Primer.* Paper presented at the Proceedings of the 27th Turbomachinery Symposium.

API610. (2010). Centrifugal Pumps for Petroleum, Heavy Duty Chemical and Gas Industry Services. *American Petroleum Institute*.

API611. (2014). GENERAL-PURPOSE STEAM TURBINES FOR PETROLEUM, CHEMICAL, AND GAS INDUSTRY SERVICES. *American Petroleum Institute*.

API616. (2011). GAS TURBINES FOR THE PETROLEUM, CHEMICAL, AND GAS INDUSTRY SERVICES. *American Petroleum Institute*.

API617. (2014). Axial and Centrifugal Compressors and Expander-compressors. In *EIGHTH EDITION, SEPTEMBER 2014*.

API684. (2005). API Standard Paragraphs Rotordynamic Tutorial: Lateral Critical Speeds, Unbalance Response, Stability, Train Tortionals, and Rotor Balancing.

Beams, & Holmes. (1941). Suspension of rotatable bodies. In: Google Patents.

Bently, D., & Muszynska, A. (1989). Fluid-generated instabilities of rotors. *Orbit, 10*(1).

Bently, D., Muszynska, A., & Bosmans, R. (1989). Vibration monitoring and shaft crack detection. *Transactions of the American Nuclear Society, 60*.

Bently, D. E., & Hatch, C. T. (2003). Fundamentals of rotating machinery diagnostics. *Mechanical Engineering-CIME, 125*(12), 53-54.

Bleuler, H., Cole, M., Keogh, P., Larsonneur, R., Maslen, E., Okada, Y., . . . Traxler, A. (2009). *Magnetic bearings: theory, design, and application to rotating machinery*: Springer Science & Business Media.

Bouaziz, S., Messaoud, N. B., Mataar, M., Fakhfakh, T., & Haddar, M. (2011). A theoretical model for analyzing the dynamic behavior of a misaligned rotor with active magnetic bearings. *Mechatronics, 21*(6), 899-907.

Campbell, A. J. (1993). Static and Dynamic Alignment of Turbomachinery. *ORBIT. June*.

Childs, D., & Childs, D. W. (1993). *Turbomachinery rotordynamics: phenomena, modeling, and analysis*: John Wiley & Sons.

Clark, D. J., Jansen, M. J., & Montague, G. T. (2004). An overview of magnetic bearing technology for gas turbine engines.

Dimarogonas, A. (1973). *Newkirk effect: thermally induced dynamic instability of high-speed rotors.* Paper presented at the ASME 1973 International Gas Turbine Conference and Products Show.

Dimarogonas, A. (1992). A brief history of rotor dynamics. In *Rotordynamics' 92* (pp. 1-10): Springer.

Downie, H., Hodkiewicz, M., Keating, A., & Steere, A. L. (2015). Active Magnetic Bearings. *CEED Seminar Proceedings 2015*.

Ehtemam, V. (2012). Technical Report - Backup Air Compressor.

Ehtemam, V. (2016). Anomaly Report for Instrument Air Compressor.

Fluke. (2013). Most common causes of machine vibration.

Friswell, M. I. (2010). *Dynamics of rotating machines*: Cambridge University Press.

General-Electric. (2017). Turboexpander-compressors. Retrieved from https://www.geoilandgas.com/subsea-offshore/offshore-turbomachinery/turboexpander-compressors

Genta, G. (2007). *Dynamics of rotating systems*: Springer Science & Business Media.

Goldman, M. (1995). Rotor-to-stator, rub-related, thermal/mechanical effects in rotating machinery. *Chaos, Solutions & Fractals, 5*(9), 1579-1601.

Gouws, R. (2013). Active magnetic bearing condition monitoring. *World Journal of Engineering, 10*(2), 179-188. doi:10.1260/1708-5284.10.2.179

Halminen, O., Kärkkäinen, A., Sopanen, J., & Mikkola, A. (2015). Active magnetic bearing-supported rotor with misaligned cageless backup bearings: A dropdown event simulation model. *Mechanical Systems and Signal Processing, 50-51*, 692-705. doi:10.1016/j.ymssp.2014.06.001

Hatch, M. R. (2000). *Vibration simulation using MATLAB and ANSYS*: CRC Press.

Huang, T., Chen, Z., Zhang, H.-T., & Ding, H. (2015). Active control of an active magnetic bearings supported spindle for chatter suppression in milling process. *Journal of Dynamic Systems, Measurement, and Control, 137*(11), 111003.

Huang, Y. (2007). Model predictive control of magnetic bearing system.

Inman, D. J. (2017). *Vibration with control*: John Wiley & Sons.

ISO7919. (2009). Mechanical vibration of non-reciprocating machines - Measurement on rotating shafts and evaluation criteria.

ISO13373-2. (2016). Condition monitoring and diagnostics of machines - Vibration condition monitoring. Part 2: Processing, analysis and presentation of vibration data.

ISO14839-1. (2002). Mechanical Vibration -- Vibration of rotating machinery equipped with active magnetic bearings -- Part 1: Vocabulary In.

ISO14839-2. (2004). Mechanical Vibration -- Vibration of rotating machinery equipped with active magnetic bearings -- Part 2: Evaluation of vibration In.

ISO14839-3. (2006). Mechanical Vibration -- Vibration of rotating machinery equipped with active magnetic bearings -- Part 3: Evaluation of stability margin In.

ISO14839-4. (2012). Mechanical Vibration -- Vibration of rotating machinery equipped with active magnetic bearings -- Part 4: Technical guidelines. In.

Jeffcott, H. H. (1919). XXVII. The lateral vibration of loaded shafts in the neighbourhood of a whirling speed.—The effect of want of balance. *The London, Edinburgh, and Dublin Philosophical Magazine and Journal of Science, 37*(219), 304-314.

Ji, J.-C., Hansen, C. H., & Zander, A. C. (2008). Nonlinear dynamics of magnetic bearing systems. *Journal of Intelligent Material Systems and Structures, 19*(12), 1471-1491.

Jiancheng, F., Shiqiang, Z., & Bangcheng, H. (2013). AMB Vibration Control for Structural Resonance of Double-Gimbal Control Moment Gyro With High-Speed Magnetically Suspended Rotor. *Mechatronics, IEEE/ASME Transactions on, 18*(1), 32-43. doi:10.1109/TMECH.2011.2161877

Keogh, & Patrick, S. (2012). Contact dynamic phenomena in rotating machines: Active/passive considerations. *Mechanical Systems and Signal Processing, 29*(C), 19-33. doi:10.1016/j.ymssp.2011.06.024

Keogh, P., & Cole, M. (2017). Dynamic conditions to destabilize persistent Rotor/touchdown bearing contact in AMB systems. *Mechanical Engineering Journal, 4*(5), 17-00005-00017-00005.

Keogh, P. S. (2012). Contact dynamic phenomena in rotating machines: Active/passive considerations. *Mechanical Systems and Signal Processing, 29*(C), 19-33. doi:10.1016/j.ymssp.2011.06.024

Liu, T., Lyu, M., Wang, Z., & Yan, S. (2018). An identification method of orbit responses rooting in vibration analysis of rotor during touchdowns of active magnetic bearings. *Journal of Sound and Vibration, 414*, 174-191. doi:10.1016/j.jsv.2017.11.001

Lyu, M. D., Liu, T., Wang, Z., Yan, S., Jia, X., & Wang, Y. (2018). Orbit Response Recognition During Touchdowns by Instantaneous Frequency in Active Magnetic Bearings. *J. Vib. Acoust.-Trans. ASME, 140*(2). doi:10.1115/1.4037850

Maslen, E. H., & Schweitzer, G. (2009). doi:10.1007/978-3-642-00497-1

Muszynska, A. (2005). *Rotordynamics*: CRC press.

Muszynska, A., Bently, D. E., Franklin, W. D., Hayashida, R. D., Kingsley, L. M., & Curry, A. E. (1989). Influence of rubbing on rotor dynamics, Part 1.

Muszynska , G. (1995). Chaotic responses of unbalanced rotor/bearing/stator systems with looseness or rubs. *Chaos, Solitons & Fractals, 5*(9), 1683-1704.

Newkirk, B. L. (1927). Shaft rubbing. *Naval Engineers Journal, 39*(1), 114-120.

Padovan, J., & Choy, F. (1987). Nonlinear dynamics of rotor/blade/casing rub interactions. *Journal of turbomachinery, 109*(4), 527-534.

Ren, S., Bian, C., & Liu, J. (2008). *Finite element analysis on the electromagnetic fields of active magnetic bearing.* Paper presented at the Journal of Physics: Conference Series.

Roy, H. K., Das, A. S., & Dutt, J. K. (2016). An efficient rotor suspension with active magnetic bearings having viscoelastic control law. *Mechanism and Machine Theory, 98*(C), 48-63. doi:10.1016/j.mechmachtheory.2015.11.012

Schweitzer, G. (2009). Introduction and survey. In *Magnetic bearings* (pp. 1-26): Springer.

SKF. (2014a). MBRotor-II Manual - Rotordynamic Excerpt.

SKF. (2014b). *User's Guide MBRotor-II Test Stand Hardware Manual 892-0103 Rev B*. SKF Magnetic Bearings.

Somad, F. (2007). *System identification and control of magnetic bearing systems.* Victoria University,

Spangler, D., Prins, R., & Kasarda, M. (2017). *A System Identification Technique Using Bias Current Perturbation for the Determination of the Magnetic Axes of an Active Magnetic Bearing.* Paper presented at the Actuators.

Srinivas, R. S., Tiwari, R., & Kannababu, C. (2018). Application of active magnetic bearings in flexible rotordynamic systems – A state-of-the-art review. *Mechanical Systems and Signal Processing, 106*, 537-572. doi:10.1016/j.ymssp.2018.01.010

Štimac, G., Braut, S., Buli, N., & Iguli, R. (2013). Modeling and experimental verification of a flexible rotor AMB system. *COMPEL - The international journal for computation and mathematics in electrical and electronic engineering, 32*(4), 1244-1254. doi:10.1108/03321641311317068

Subramanian, S., Sekhar, A. S., & Prasad, B. V. S. S. S. (2017). Rotordynamic characterization of rotating labyrinth gas turbine seals with radial growth: Combined centrifugal and thermal effects. *International Journal of Mechanical Sciences, 123*, 1-19. doi:10.1016/j.ijmecsci.2017.01.033

Sun, Z., Yan, X., Zhao, J., Kang, X., Yang, G., & Shi, Z. (2017). Dynamic Behavior Analysis of Touchdown Process in Active Magnetic Bearing System Based on a Machine Learning Method. *Science and Technology of Nuclear Installations, 2017*. doi:10.1155/2017/1839871

Swanson, E., Masala, A., & Hawkins, L. (2014). *A new Active Magnetic Bearing Requirements for Compressors in API 617 Eighth Edition.* Paper presented at the Proceedings of the 43rd Turbomachinery Symposium, Tutorial.

Tan, H. N., & Zhang, J. S. (2012). Method of Variable Parameter PID Control Applied for AMB System. *Applied Mechanics and Materials, 150-150*, 75-79. doi:10.4028/www.scientific.net/AMM.150.75

Traxler, A., & Maslen, E. (2009). Hardware Components. In *Magnetic bearings* (pp. 69-109): Springer.

Voigt, A. J., Mandrup-Poulsen, C., Nielsen, K. K., & Santos, I. F. (2017). Design and Calibration of a Full Scale Active Magnetic Bearing Based Test Facility for Investigating Rotordynamic Properties of Turbomachinery Seals in Multiphase Flow. *Journal of Engineering for Gas Turbines and Power, 139*(5), 052505-052505-052510. doi:10.1115/1.4035176

von Groll, G. (1995). *Dynamic Properties of Rotating Structures: Modelling and Visualisation of Simulation and Experimental Results.* Imperial College,

Weiler, B. (2017). Finite Element Method Based Analysis and Modeling in Rotordynamics. In R. Allemang, J. Kim, & D. Thompson (Eds.): ProQuest Dissertations Publishing.

Xiaowen, D., Mingfu, L., & Robert, L. (2002). Coupled Bending and Torsional Vibrations Due to Rotor-to-Stator Contacts [J]. *Journal of Aerospace Power, 17*(1), 97-104.

Yung, C. (2001). Laser alignments not as simple as they seem: unusual machinery operating characteristics, such as thermal growth, mean that operator knowledge and experience are essential for good results. *Machinery & Equipment, 17*(3), 25.

Zhao, Y., Yang, G., Keogh, P., & Zhao, L. (2017). Dynamic Analysis for the Rotor Drop Process and Its Application to a Vertically Levitated Rotor/Active Magnetic Bearing System. *J. Tribol.-Trans. ASME, 139*(4). doi:10.1115/1.4035343

Zheng, S., Han, B., Feng, R., & Jiang, Y. (2015). Vibration Suppression Control for AMB-Supported Motor Driveline System Using Synchronous Rotating Frame Transformation. *Industrial Electronics, IEEE Transactions on, 62*(9), 5700-5708. doi:10.1109/TIE.2015.2407857

Zheng, S., Li, H., Peng, C., & Wang, Y. (2017). Experimental Investigations of Resonance Vibration Control for Noncollocated AMB Flexible Rotor Systems. *Industrial Electronics, IEEE Transactions on, 64*(3), 2226-2235. doi:10.1109/TIE.2016.2623580

Appendices

Appendix 1

Components of test stands (SKF, 2014b).

Confidential vendor-supplied data removed from this publically accessible electronic copy.

A reader seeking that data should contact SKF directly.

Appendix 2

Confidential vendor-supplied data removed from this publically accessible electronic copy.

A reader seeking that data should contact SKF directly.